

PROCEEDINGS

ISSN Print: 2518-4245

ISSN Online: 2518-4253

Vol. 60(2), June 2023

OF THE PAKISTAN ACADEMY OF SCIENCES: A. Physical and Computational Sciences



PAKISTAN ACADEMY OF SCIENCES
ISLAMABAD, PAKISTAN

Proceedings of the Pakistan Academy of Sciences: Part A Physical and Computational Sciences

President: Khalid Mahmood Khan
Secretary General: Tasawar Hayat
Treasurer: Amin Badshah

Proceedings of the Pakistan Academy of Sciences A. Physical and Computational Sciences is the official flagship, the peer-reviewed quarterly journal of the Pakistan Academy of Sciences. This open-access journal publishes original research articles and reviews on current advances in the field of Computer Science (all), Materials Science (all), Physics and Astronomy (all), Engineering Sciences (all), Chemistry, Statistics, Mathematics, Geography, Geology in English. Authors are not required to be Fellows or Members of the Pakistan Academy of Sciences or citizens of Pakistan. The journal is covered by Print and Online ISSN, indexed in Scopus, and distributed to scientific organizations, institutes and universities throughout the country, by subscription and on an exchange basis.

Editor:

Riffat Mahmood Qureshi, Pakistan Academy of Sciences, Islamabad, Pakistan; editor@paspk.org

Managing Editor:

Ali Ahsan, Pakistan Academy of Sciences, Islamabad, Pakistan; editor@paspk.org

Discipline Editors:

Chemical Sciences: Guo-Xin Jin, Inorganic Chemistry Institute, Fudan University, Shanghai, China

Chemical Sciences: Haq Nawaz Bhatti, Department of Chemistry University of Agriculture, Faisalabad, Pakistan

Geology: Peng Cui, Key Laboratory for Mountain Hazards and Earth Surface Process, CAS, Institute of Mountain Hazards & Environment, CAS Chengdu, Sichuan, People's Republic of China

Computer Sciences: Sharifullah Khan, Faculty of Electrical, Computer, IT & Design(FECID), Pak-Austria Fachhochschule: Institute of Applied Sciences and Technology (PAF-IAST), Mange, Haripur, Pakistan

Engineering Sciences: Akhlesh Lakhtakia, Evan Pugh University Professor and The Charles G. Binder (Endowed), Engineering Science and Mechanics, Pennsylvania State University, University Park, USA

Mathematical Sciences: Ismat Beg, Department of Mathematics and Statistical Sciences, Lahore School of Economics, Lahore, Pakistan

Mathematical Sciences: Jinde Cao, Department of Mathematics, Southeast University Nanjing, P. R. China

Physical Sciences: Asghari Maqsood, Department of Physics, E-9, PAF Complex Air University, Islamabad

Physical Sciences: Niemela J. Joseph, The Abdus Salam International Center for Theoretical Physics (ICTP-UNESCO), Trieste- Italy

Editorial Advisory Board:

Saeid Abbasbandy, Department of Mathematics, Imam Khomeini International University Ghazvin, 34149-16818, Iran

Muazzam Ali Khan Khattak, Department of Computer Science, Quaid-i-Azam University, Islamabad, Pakistan

Muhammad Sharif, Department of Mathematics, University of the Punjab, Lahore, Pakistan

Faiz Ullah Shah, Department of Civil, Environmental and Natural Resources Engineering, Lulea University of Technology, Luleå, Sweden

Kashif Nisar, Faculty of Computing and Informatics University Malaysia Sabah Jalan UMS, Kota Kinabalu Sabah, Malaysia

Guoqian Chen, Laboratory of Systems Ecology and Sustainability Science, College of Engineering, Peking University, Beijing, China

Bhagwan Das, Department of Electronic Engineering, Quaid-e-Awam University of Engineering, Science and Technology Nawabshah, Sindh, Pakistan

Muhammad Sadiq Ali Khan, Department of Computer Science, University of Karachi, Pakistan

Annual Subscription: **Pakistan:** Institutions, Rupees 4000/-; Individuals, Rupees 2000/- (Delivery Charges: Rupees 150/-)

Other Countries: US\$ 200.00 (includes air-lifted overseas delivery)

© *Pakistan Academy of Sciences*. Reproduction of paper abstracts is permitted provided the source is acknowledged. Permission to reproduce any other material may be obtained in writing from the Editor.

The data and opinions published in the *Proceedings* are of the author(s) only. The *Pakistan Academy of Sciences* and the *Editors* accept no responsibility whatsoever in this regard.

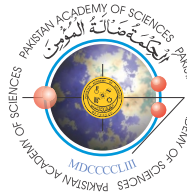
HEC Recognized, Category Y; Scopus Indexed

Published by **Pakistan Academy of Sciences**, 3 Constitution Avenue, G-5/2, Islamabad, Pakistan

Email: editor@paspk.org; **Tel:** 92-51-920 7140 & 921 5478; **Websites:** www.paspk.org/proceedings/; www.paspk.org

Printed at **Graphics Point.**, Office 3-A, Wasal Plaza, Fazal-e-Haq Road Blue Area Islamabad.

Ph: 051-2806257, **E-mail:** graphicspoint16@gmail.com



PROCEEDINGS OF THE PAKISTAN ACADEMY OF SCIENCES: PART A Physical and Computational Sciences

CONTENTS

Volume 60, No. 2, June 2023

Page

Research Articles

- Stability of Graphene on the Si (111) Surface: Insights from Reactive Molecular Dynamics Simulations 1
— *Didik Riyanto, Edy Kurniawan, Husein Muhammad Fras, Hanifha Nur Azizah, and Rizal Arifin*
- Analysis of a City's Heat Island Effect on the Micro-Climature Parameters within Cities 7
— *Rishabh Sharma, Khan Amadur Rahman, Vasyl Tyshchenko, Oksana Illiash, and Iryna Mezentseva*
- Flow Control in a Rectangular Open Channel using Two Impermeable Spur Dikes: A Numerical Study 17
— *Hafiz Syed Moazzum Gillani, Zain-ul-Hassan, Hafiz Rana Azeem Sarwar, Muhammad Sohail Jameel, Waqar Hasan, Ehsaan Manzoor, and Imran Khan*
- Catalogues of Some Useful Classes of Circular Designs in Blocks of Three Different Sizes to Control Neighbor Effects 27
— *Akbar Fardos, Abdul Salam, Jamshaid Ul Hassan, Hurria Ali, Khadija Noreen, and Rashid Ahmed*
- A Stable Version of the Modified Algorithm for Error Minimization in Combined Numerical Integration 37
— *Aijaz Bhatti, Owais Ali Rajput, and Zubair Ahmed Kalhoro*
- Quantum Computer Architecture: A Quantum Circuit-Based Approach Towards Quantum Neural Network 45
— *Tariq Mahmood, Talab Hussain, and Maqsood Ahmed*
- Design and Development of Neutronics and Thermal Hydraulics Modeling Code for ACP1000 Nuclear Reactor Dynamics in LabVIEW 55
— *Arshad Habib Malik, Feroza Arshad, and Aftab Ahmad Memon*

Instructions for Authors

Submission of Manuscripts: Manuscripts may be submitted as an e-mail attachment at editor@paspk.org or submit online at <http://ppaspk.org/index.php/PPASA/about/submissions>. Authors must consult the **Instructions for Authors** at the end of this issue or at the Website: www.paspk.org/proceedings/ or www.ppaspk.org.



Stability of Graphene on the Si (111) Surface: Insights from Reactive Molecular Dynamics Simulations

Didik Riyanto¹, Edy Kurniawan¹, Husein Muhammad Fras¹, Hanifha Nur Azizah²,
and Rizal Arifin^{2*}

¹Department of Electrical Engineering, Universitas Muhammadiyah Ponorogo, Jl. Budi Utomo No. 10 Ponorogo, Indonesia

²Department of Mechanical Engineering, Universitas Muhammadiyah Ponorogo, Jl. Budi Utomo No. 10 Ponorogo, Indonesia

Abstract: The remarkable characteristics of graphene render it well-suited for a diverse range of applications, particularly in the realm of electronic devices. After the synthesis process, the two-dimensional material known as graphene is then transferred onto a substrate. Silicon (Si) is considered a suitable choice for this purpose. Therefore, it has become essential to investigate the stability of graphene on silicon surfaces. This study utilized reactive molecular dynamics simulations to investigate the thermal stability of graphene on a Si (111) substrate across a temperature range of 300 to 1500 K. The results demonstrate the exceptional stability of graphene on this particular surface. This phenomenon can be explained by the restricted intermolecular interactions between the carbon atoms in graphene and the silicon atoms on the substrate surface. The study findings indicate that graphene exhibits a dome-shaped configuration on the Si (111) surface. In this configuration, only the carbon atoms located at the periphery of the graphene structure interact with the silicon atoms present on the underlying substrate.

Keywords: Graphene, Thermal Stability, Si (111) Surface, Dome-shaped Configuration, Reactive Molecular Dynamics Simulations.

1. INTRODUCTION

The research community has shown significant interest in the two-dimensional material known as graphene [1–5]. Graphene is widely recognized for its exceptional properties, including high electronic conductivity [6], excellent optical transmission [7], and notable mechanical flexibility [8]. These characteristics position graphene as a promising material for potential applications in electronic devices, such as capacitors [9], transistors [10], and photodetectors [11], in the future. The catalytic ability of graphene in the combustion reaction of 1,3,5-trinitroperhydro-1,3,5-triazine has been investigated by Song *et al.* [12]. According to their findings, it has been reported that wrinkled graphene exhibits a higher level of reactivity compared to its flat counterpart [12]. Furthermore, graphene has been employed as a nano-scale composite material in the field of water filtration [13]. The researchers have successfully demonstrated a notable

distinction between the water samples before and after filtration, suggesting that the filtration process is functioning effectively [13].

Graphene can be synthesized through various methods, one of which is chemical vapor deposition (CVD), a widely recognized technique known for its high efficiency and effectiveness. In the process of CVD, graphene is synthesized on metal substrates, including nickel (Ni), copper (Cu), and platinum (Pt). Following this, the graphene is then transferred onto alternative substrates, such as silicon (Si) and silicon dioxide (SiO₂) surfaces [13, 14]. In 2009, a substrate made of polycrystalline Cu foil was utilized for the initial production of a large-area single-layered graphene film. This achievement has served as a catalyst for further investigation into the synthesis of graphene using metal foils and thin films [15]. In addition, the production of graphene can be achieved through deposition of metal films, offering potential advantages. The utilization of

various metallic substrates for growth purposes can result in unique growth patterns, including rare metals beyond Cu and Ni, as well as binary or ternary alloys that are not easily available in foil form. The regulation of carbon content and the ratio of different metals in an alloy can be efficiently achieved through the control of metal film thickness. The aforementioned control mechanism has a direct impact on the deposition process of graphene and subsequently influences the quantity of layers that are formed. Multiple studies have documented that the process of deposition and annealing on particular single-crystal substrates can result in the formation of single-crystal metal films that display a preferred orientation. The carbon atoms located on or within the thin metal film have the ability to diffuse through it and ultimately reach the interface between the film and substrate. This phenomenon enables the direct growth of graphene on the substrate, thereby eliminating the requirement for growth through transfer methods [16]. Furthermore, Tai *et al.* [17] have achieved successful synthesis of graphene directly on a silicon substrate using metal-free ambient-pressure CVD. This method has resulted in the production of atomically flat monolayer or bilayer graphene, as well as concave bilayer and bulging few-layer graphene domains [18].

While Si is commonly used as a substrate for graphene in electronic applications, there is a limited amount of research available on the stability of graphene on Si surfaces. The stability of graphene on a Si (001) surface was examined by Javvaji *et al.* through molecular dynamics (MD) simulations at temperatures of 100, 300, and 900 K [19]. In a separate study, Zhang *et al.* [20] examined the bonding mechanism between graphene and the surface of a silicon substrate by applying a consistent vertical upward exfoliation velocity.

The objective of the current study was to evaluate the stability of graphene on a Si (111) surface using reactive MD simulations. These computations facilitate the examination of the processes involved in the formation and dissociation of C–C and C–Si bonds on the substrate, which have not been thoroughly investigated in previous studies. The changes in the structural composition of graphene were determined through MD simulations conducted at various temperatures ranging from 300 to 1500 K.

2. METHODOLOGY

The calculations were performed using the ReaxFF module of the Amsterdam Modeling Suite 2022 [21–23]. Additionally, we utilized the ReaxFF force field parameters proposed by Soria *et al.* [24] to accurately represent the atomic interactions involving Si–Si, Si–C, and C–C. Figure 1 illustrates the Si (111) substrate comprising of four layers having a total of 600 Si atoms. The lowermost two layers were held in a fixed position to accurately replicate the substrate’s thickness. Furthermore, the structural optimization was enhanced by the introduction of a carbon atom or carbon ring into the substrate. MD simulations were utilized to examine the thermal stability of graphene on the Si (111) surface. The temperature was incrementally increased from 300 to 1500 K in a systematic manner with increments of 100 K. A time step of 0.25×10^{-3} picoseconds was selected along with a temperature increase rate of 8 Kelvin per picosecond. Equilibration was performed at each temperature for a duration of 25 picoseconds. The temperature control in the simulation was achieved by utilizing the Nosé-Hoover thermostat [25–27]. The adsorption energies (E_{ads}) of the C atoms and C rings at different sites on the Si (111) surface were calculated using the following equation:

$$E_{ads} = E_{sc} - (E_s + E_c) \quad (1)$$

where, E_{sc} represents the energy of the system, which includes the Si substrate and the C atom or ring, E_s represents the energy of the substrate, while E_c represents the energy of the isolated C atom or ring. The analysis of the simulation results

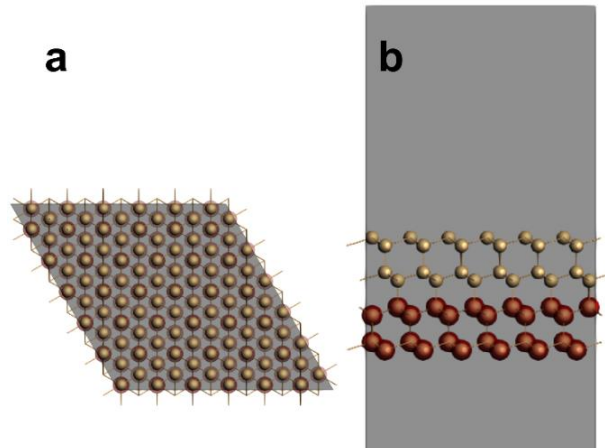


Fig. 1. (a) Top and (b) side views of the initial configuration of the Si (111) substrate. The Si atoms are represented by yellow spheres.

trajectory was conducted using the Ovito software [28]. Furthermore, a coordination analysis was conducted on the C atoms in graphene on the Si (111) surface at various simulation temperatures.

3. RESULTS AND DISCUSSION

The stability of graphene was evaluated through the calculation of adsorption energies for C atoms and hexagonal carbon rings on the Si (111) substrate. Following that, it underwent evaluation via MD simulations, spanning a temperature range from 300 to 1500 K.

3.1 Adsorption Energies of C Atoms and C Rings on the Si (111) Surface

In Table 1, the adsorption energies and heights of the C atoms at different sites on the Si (111) surface are presented. The results indicate that the C atoms located above the Si atoms in the second and third layers occupy the hollow 2 and hollow 3 sites, respectively. According to the data presented in Table 1, it can be observed that the hollow 2 site exhibits the highest adsorption energy (-3.87 eV), while the bridge site demonstrates the lowest adsorption energy (-5.74 eV). The h (Å) data pertains to the vertical distance between the C atoms and the Si (111) surface. The C atoms situated at the bridge site exhibit a vertical displacement of 0.12 Å from the Si (111) surface. Conversely, the C atoms positioned at the hollow 2 site show a greater vertical displacement of 1.66 Å from the substrate.

Table 1. Adsorption energies (E_{ads}) and heights (h) of C atoms at various sites on the Si (111) surface.

Site	E_{ads} (eV)	h (Å)
Top	-4.14	1.38
Bridge	-5.74	0.12
Hollow 2	-3.87	1.66
Hollow 3	-4.75	1.08

Figure 2 illustrates the adsorption sites on the Si (111) surface in relation to the C atoms, as outlined in Table 1. In Figure 2a, it can be observed that the C atoms are positioned directly above the Si atoms in the uppermost layer. The distance between the C atoms and the Si atoms is precisely 1.38 Å. In Figure 2b, it can be observed that the C atoms are positioned between the Si atoms in both the first and second layers. Notably, both sets of Si atoms exhibit a slight displacement from their initial positions, facilitating contact between the C atoms

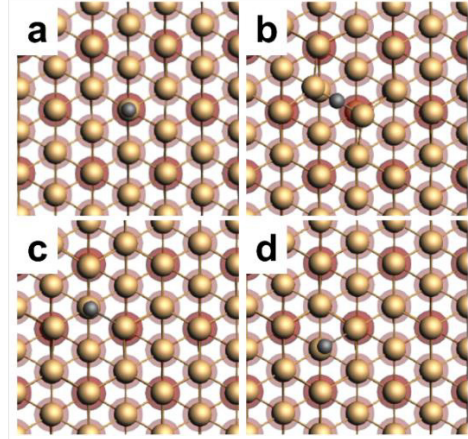


Fig. 2. Optimized arrangement of C atoms on the Si (111) surface at four distinct locations: (a) top site, (b) bridge site, (c) hollow site situated above the second layer of Si atoms, and (d) hollow site situated above the third layer of Si atoms. The Si and C atoms are represented by the yellow and gray spheres, respectively.

and the surface. In comparison to the adsorption energies documented for alternative adsorption sites, this phenomenon yields the most minimal adsorption energy value. The findings of this study align with prior research, which suggests that C atoms adsorbed onto the Si (111) surface exhibit a preference for bridge sites [29]. Figures 2c–d demonstrate that the C atoms adsorbed onto the hollow 2 and hollow 3 sites undergo a subtle displacement towards a Si atom positioned in the top layer. This displacement leads to the establishment of chemical bonds between them.

Table 2 presents the adsorption energies of hexagonal C rings on the Si (111) surface, considering different locations. Sites 1, 2, and 3 correspond to the positions located above the Si atoms in the first, second, and third layers of the substrate, respectively. The adsorption energy of the C ring at site 1 exhibits a positive value, suggesting the presence of a repulsive interaction between the C ring and Si atoms on the substrate surface. This is supported by the observation of a Si atom displacement in the uppermost region of the substrate, resulting in the penetration of the C ring into the substrate (refer to atom 1 in Figure 3a). The adsorption energies of the C rings situated at sites 2 and 3 exhibit negative values, suggesting the presence of attractive interactions between the C and Si atoms on the surface of the Si (111) substrate. The site with the lowest adsorption energy is designated as site 3. At this location, each C atom in the C ring establishes a binding interaction with the

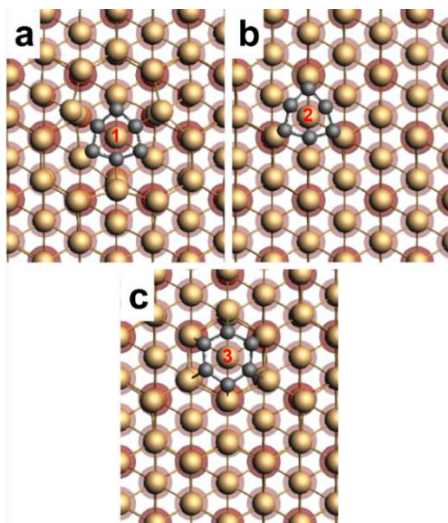


Fig. 3. Optimized arrangement of C rings on the Si (111) surface at three distinct locations: the sites situated above the (a) first, (b) second, and (c) third layers of Si atoms. The Si and C atoms are represented as yellow and gray spheres, respectively. The spheres denoted by indices 1, 2, and 3 correspond to the Si atoms located in the first, second, and third layers, respectively.

Si atoms found in both the first and second layers (refer to Figure 3c). The hexagonal shape of the C ring is preserved in this scenario. At location 3, it is evident that specific C atoms are unable to form bonds with Si atoms in the third layer due to the considerable distance separating them. Only the C atoms that are in close proximity to the Si atoms in the first layer have the capability to establish chemical bonds. This phenomenon is accountable for the distortion of the C ring. Based on the results obtained, it can be concluded that the adsorption of the C ring is more favorable at site 3 on the Si (111) surface.

Table 2. Adsorption energies (E_{ads}) of C rings at various sites on the Si (111) surface. The positions above the Si atoms in the first, second, and third layers of the substrate are represented by sites 1, 2, and 3, respectively.

Adsorption Site	E_{ads} (eV)
Site 1	1.94
Site 2	-3.88
Site 3	-4.00

3.2 Effect of Temperature on Graphene Stability on Si (111) Surface

The graph in Figure 4 illustrates the variation in the maximum height of a C atom in graphene in relation to the Si (111) surface at different temperatures.

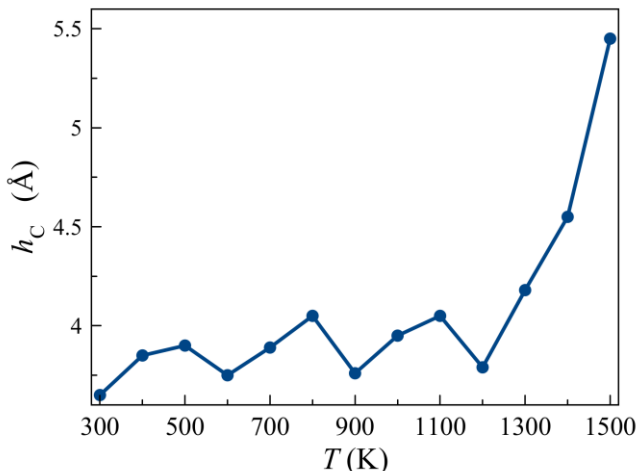


Fig. 4. The maximum vertical distance (h_c) between a C atom in graphene and the Si (111) surface at temperatures of 300 to 1500 K.

The maximum height exhibits slight variations within the temperature range of 300 to 1200 K, but undergoes a notable increase between 1300 and 1500 K. Figure 5 illustrates the dome-shaped morphology of graphene observed on the Si (111) surface. It is worth mentioning that the C atoms located at the periphery of the graphene structure establish chemical bonds with the Si atoms present on the surface of the substrate. Conversely, the C atoms situated in the central region of the graphene structure exhibit a tendency to distance themselves from the Si (111) surface. Figures 5a–b depict the similarity observed in the graphene domes on the Si (111) surface at temperatures of 300 and 900 K, respectively. Additionally, Figure 5c illustrates the alterations in the shape of the graphene dome when subjected to a temperature of 1500 K.

Furthermore, the determination of the graphene structure can be achieved through the analysis of the radial distribution function $g(r)$, as depicted in Figure 6. The $g_{C-C}(r)$ plots, which illustrate the interatomic distances between C atoms in graphene, demonstrate a significant resemblance across the temperature range from 300 to 1500 K. The primary peak of $g_{C-C}(r)$ is observed within the range of 1.42 to 1.47 Å between carbon-carbon (C-C) atoms. The discrepancy in the observed value can be attributed to the vibrational freedom of C atoms at higher temperatures. The obtained value aligns with the results of prior research, which suggest that the distance between C-C atoms in graphene falls within the range of 1.42 Å to 1.49 Å [30-31]. The obtained results demonstrate the remarkable stability of graphene on the Si (111) surface, where

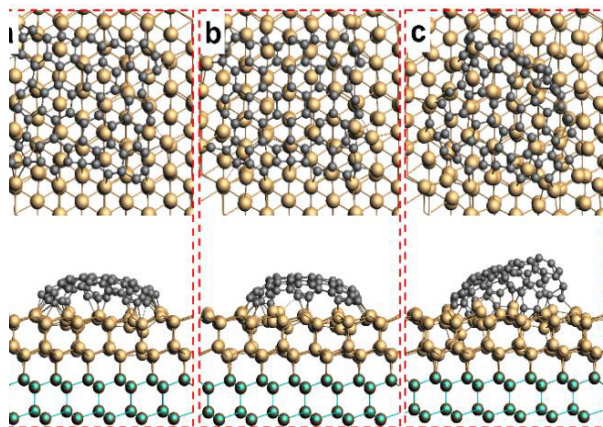


Fig. 5. Graphene on the Si (111) surface at temperatures of (a) 300 K, (b) 900 K, and (c) 1500 K. The upper and lower images depict perspectives from the top and side, respectively.

the interactions between the C atoms in graphene and the Si atoms on the substrate surface are found to be minimal, thus playing a significant role in this aspect. The results obtained are consistent with the findings of previous studies conducted by Zhang *et al.* [20] and suggest that a vertical upward velocity of 4.3 Å/ps is necessary for the exfoliation of monolayer graphene from the Si surface.

4. CONCLUSION

The stability of graphene on a Si (111) surface was investigated through the utilization of reactive MD simulations. The Si (111) bridge site demonstrated a higher affinity for the adsorption of C atoms compared to other potential sites, such as the top and hollow sites. Additionally, it was observed that the C ring predominantly occupies the surface site positioned directly above the Si atoms in the third layer. Furthermore, the findings of this investigation suggest that graphene demonstrates remarkable stability on the Si (111) surface at temperatures up to 1500 K. This stability can be attributed to the limited interactions between the C atoms in graphene and the Si atoms in the substrate.

5. ACKNOWLEDGMENTS

The research conducted in this study received financial support from Universitas Muhammadiyah Ponorogo through a grant for fundamental research in 2023. The grant was awarded under contract #066/VI.4/PN/2023.

6. CONFLICT OF INTEREST

The authors declare no conflict of interest.

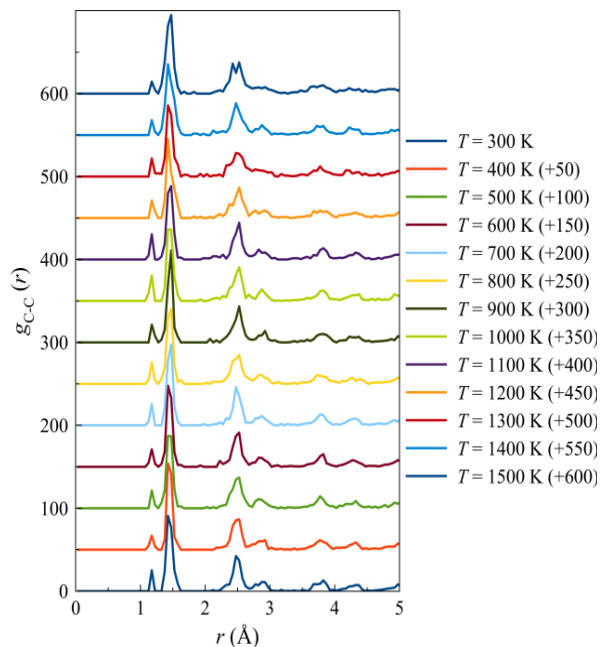


Fig. 6. Radial distribution functions of C–C interatomic distances, $g_{C-C}(r)$, in graphene on the Si (111) surface over the temperature range of 300 to 1500 K.

7. REFERENCES

1. Y. Liu, M. Xu, X. Zhu, M. Xie, Y. Su, N. Hu, Z. Yang, and Y. Zhang. Synthesis of carbon nanotubes on graphene quantum dot surface by catalyst free chemical vapor deposition. *Carbon* 68: 399–405 (2014).
2. R. Arifin, Y. Shibuta, K. Shimamura, and F. Shimojo. First principles molecular dynamics simulation of graphene growth on Nickel (111) surface. *IOP Conference Series: Materials Science and Engineering* 128: 012032 (2016).
3. R. Arifin, Y. Shibuta, K. Shimamura, F. Shimojo, and S. Yamaguchi. Ab Initio Molecular Dynamics Simulation of Ethylene Reaction on Nickel (111) Surface. *Journal of Physical Chemistry C* 119: 3210–3216 (2015).
4. R. Arifin, Y. Shibuta, K. Shimamura, and F. Shimojo. First principles calculation of CH₄ decomposition on nickel (111) surface. *The European Physical Journal B* 88: 303 (2015).
5. Y. Shibuta, R. Arifin, K. Shimamura, T. Oguri, F. Shimojo, and S. Yamaguchi. Ab initio molecular dynamics simulation of dissociation of methane on nickel(111) surface: Unravelling initial stage of graphene growth via a CVD technique. *Chemical Physics Letters* 565: 92–97 (2013).
6. K.S. Novoselov, A.K. Geim, S.V. Morozov, D. Jiang, Y.Zhang, S.V. Dubonos, I.V. Grigorieva and A.A. Firsov. Electric Field Effect in Atomically Thin Carbon Film. *Science* 306: 666–669 (2004).

7. R.R. Nair, P. Blake, A.N. Grigorenko, K.S. Novoselov, T. J. Booth, T. Stauber, N.M.R. Peres and A.K. Geim. Fine Structure Constant Defines Visual Transparency of Graphene. *Science* 320: 1308–1308 (2008).
8. A. K. Geim, K. S. Novoselov. The rise of graphene. *Nature Materials* 6: 183–191 (2007).
9. S.H. Abro, F.Hussain, M.Sohail, D.Tariq, K. Jawed, R. Sanwal, and M.N. Alghamdi. Development and Synthesis of Composite Electrode (rGO/G/PANI) for Capacitor from Burnout Battery Powder: Composite Electrode (rGO/G/PANI) for Capacitor. *Proceedings of the Pakistan Academy of Sciences: A* 57: 41–50 (2021).
10. A.Béraud, M.Sauvage, C.M. Bazan, M. Tie, A. Bencherif, and D. Bouilly. Graphene field-effect transistors as bioanalytical sensors: design, operation and performance. *Analyst* 146: 403–428 (2021).
11. K. Murali, N. Abraham, S. Das, S. Kallatt, and K. Majumdar. Highly Sensitive, Fast Graphene Photodetector with Responsivity >106 A/W Using a Floating Quantum Well Gate. *ACS Applied Materials & Interfaces* 11: 30010–30018 (2019).
12. L. Song, F.Q. Zhao, S.Y. Xu, X.H. Ju, and C.C. Ye. Onset of catalytic activity of graphene nanosheets in reaction with energetic materials evaluated by ReaxFF molecular dynamics simulation. *Surfaces and Interfaces* 31: 102024 (2022).
13. S.H. Abro, A. Chandio, I.A. Channa, and A.S. Alaboodi. Design, Development and Characterization of Graphene Sand Nano-Composite for Water Filtration. *Pakistan Journal of Scientific and Industrial Research Series A: Physical Sciences* 63A: 118–122 (2020).
14. D.V. Smovzh, I.A. Kostogrud, E.V. Boyko, and M.A. Morozova. Graphene transfer from a copper surface to a silicon substrate. *Journal of Physics: Conference Series* 1675: 012098 (2020).
15. Z. Khanam, I. Riaz, A. Rasheed, and R. Jalil. Fabrication and Identification of Graphene Layers on Silicon Dioxide and Flexible PMMA Substrates: Graphene fabrication. *Proceedings of the Pakistan Academy of Sciences: A* 53: 431–445 (2021).
16. X. Li, W. Cai, J. An, S. Kim, J. Nah, D. Yang, R. Piner, A. Velamakanni, I. Jung, E. Tutuc, S.K. Banerjee, L. Colombo, and R.S. Ruoff. Large-Area Synthesis of High-Quality and Uniform Graphene Films on Copper Foils. *Science* 324: 1312–1314 (2009).
17. S. Xu, L. Zhang, B. Wang, and R.S. Ruoff. Chemical vapor deposition of graphene on thin-metal films. *Cell Reports Physical Science* 2: 100372 (2021).
18. L. Tai, D. Zhu, X. Liu, T. Yang, L. Wang, R. Wang, S. Jiang, Z. Chen, Z. Xu, and X. Li. Direct Growth of Graphene on Silicon by Metal-Free Chemical Vapor Deposition. *Nano-Micro Letters* 10: 20 (2017).
19. B. Javvaji, B.M. Shenoy, D.R. Mahapatra, A. Ravikumar, G.M. Hegde, and M.R. Rizwan. Stable configurations of graphene on silicon. *Applied Surface Science* 414: 25–33 (2017).
20. Q. Zhang, Y. Zhao, X. Ma, Y. Zhao, X. Pang. Study on bonding mechanism of graphene on silicon substrate. *Modern Physics Letters B* 32: 1850265 (2018).
21. A.C.T. van Duin, W.A. Goddard, M.M. Islam, H. van Schoot, T. Trnka, and A.L. Yakovlev. ReaxFF 2022.1 (2022) <http://www.scm.com> (accessed 22 January 2023)
22. A.C.T. van Duin, S. Dasgupta, F. Lorant, and W.A. Goddard. ReaxFF: A reactive force field for hydrocarbons. *Journal of Physical Chemistry A* 105: 9396–9409 (2001).
23. K. Chenoweth, A.C.T. van Duin, and W.A. Goddard. ReaxFF reactive force field for molecular dynamics simulations of hydrocarbon oxidation. *Journal of Physical Chemistry A* 112: 1040–1053 (2008).
24. F.A. Soria, W. Zhang, P.A. Paredes-Olivera, A.C.T. van Duin, and E.M. Patrito. Si/C/H ReaxFF Reactive Potential for Silicon Surfaces Grafted with Organic Molecules. *Journal of Physical Chemistry C* 122: 23515–23527 (2018).
25. S. Nosé. A molecular dynamics method for simulations in the canonical ensemble. *Molecular Physics* 52: 255–268 (1984).
26. S. Nosé. A unified formulation of the constant temperature molecular dynamics methods. *The Journal of Chemical Physics* 81: 511–519 (1984).
27. W.G. Hoover. Canonical dynamics: Equilibrium phase-space distributions. *Physical Review A* 31: 1695 (1985).
28. A. Stukowski. Visualization and analysis of atomistic simulation data with OVITO—the Open Visualization Tool. *Modelling and Simulation in Materials Science and Engineering* 18: 015012 (2010).
29. T. Takai, T. Halicioğlu, and W.A. Tiller. Adsorption, potential maps and diffusion of Si, C, and SiC on A Si(111) surface. *Surface Science* 164: 327–340 (1985).
30. A.Z. Alzahrani. Structural and Electronic Properties of Graphene upon Molecular Adsorption: DFT Comparative Analysis. In: Graphene Simulation. J.R. Gong (ed.). *IntechOpen, Rijeka, Croatia*, pp. 21–38 (2011).
31. M. Igami, S. Okada, and K. Nakada. Electronic and geometric structures of fluorine adsorbed graphene. *Synthetic Metals* 121: 1233–1234 (2001)



Analysis of a City's Heat Island Effect on the Micro-Climature Parameters within Cities

Rishabh Sharma¹, Khan Amadur Rahman^{1*}, Vasyl Tyshchenko^{2*},
Oksana Illiash³, and Iryna Mezentseva⁴

¹Department of Architecture, Faculty of Engineering and Technology, Aligarh Muslim University, Aligarh, India

²Department of Fire Prevention and Life Safety of the Civilian Population, Institute of Public Administration and Research in Civil Protection, Kyiv, Ukraine

³Department of Applied Ecology and Nature Management, National University «Yuri Kondratyuk Poltava Polytechnic», Poltava, Ukraine

⁴Department of Occupational and Environmental Safety, National Technical University Kharkiv Polytechnic Institute, Kharkiv, Ukraine

Abstract: The Urban Heat Island (UHI) is a micro-climatic phenomenon that influences the urban areas by elevating its temperature. UHI not only causes the thermal discomfort but also exert serious health issues along with aggravation of urban microclimate. Although a lot of research has been done on this phenomenon but UHI effect on micro scale is still less explored. This paper attempts to make a contribution in UHI studies of micro-climate. It consists of examination of UHI impact on microclimate of Aligarh city areas using mobile traverse method. This study determined the presence and extent of UHI's microclimate variation within urban communities of different environmental layout and functional uses. The UHI effect started to appear from early afternoon and continue to rise with maximum UHI intensity recorded at early night. The highest recorded UHI intensity was 3.1 °C (at 21:00 hrs.), and the lowest was 0.6 °C (at 09:00 hrs.). A comparison of two districts of the same city located at a distance of 3 km and differing in population density, the number of buildings and landscaping showed that in the L1 area with more dense population and low landscaping, the temperature was consistently higher during the daily period; also the L1 region had less humidity, which combined with the already high temperature, makes it difficult to breathe and control the microclimate. These findings can be used for consideration for the future sustainable development of the affected area in regard of thermal comfort, environmental health and urban planning.

Keywords: Urban Heat Island, Urbanization, Temperature Increase, Mobile Traverse Method, Thermal Comfort, Environmental Layout, Urban Planning.

1. INTRODUCTION

Rapid urban grain change has an impact on a city's local energy balance and, consequently, its thermal and climatic characteristics [1, 2]. It is predicted that with the growth of cities, the negative impacts on the environment will increase [3]. Urban Heat Island effect is one of the environmental issues that are being caused by such scenarios [4]. The first account of the urban heat phenomenon dates back to 1818 [5] therefore numerous additional research were carried out in numerous places worldwide to

better understand the phenomenon [6, 7]. Each city is found to have a unique microclimate that differs from the regional climate pattern and is impacted by the urban form, weather, topography, water features, and greenery [8, 9]. Urban heat island impact is defined by the difference between the temperature of an urban region and that of its surroundings. This difference is often referred to as urban heat island intensity (UHII) or strength [10]. The well-known Intergovernmental Panel on Climate Change [11] report acknowledges the occurrence of UHI brought on by urbanization, loss of plant cover, and

an increase in anthropogenic heat and discusses the essential mitigation measures. The sixth assessment report [12] acknowledged the significant changes in the climate caused by humans' excessive interventions in their environment.

UHI phenomena generally comes in two flavors. The severity of surface urban heat island (SUHI) varies with the strength of the sun, the weather, and the amount of ground cover. It is often highest during the daytime and can reach temperatures of 10 to 15 °C [13]. Usually, there is a close relationship between the temperatures of near surface air and the ground surface [14]. Warmer air in urban areas than in their surroundings characterizes atmospheric municipal heat island (AUHI), which is divided into two categories based on height as stated: (i) Urban heat island canopy. The air expanse that is below the buildings and trees tops, but above the ground is called the canopy layer. Due to the fact that the majority of activities only take place in the canopy layer, the UHI in this layer immediately influences person functionality [9, 15, 16]. (ii) Heat island in the urban boundary layer. This UHI spreads from rooftops and treetops all the way down to the point where urban environments have no more influence to the atmospheric air. Typically, this vertical spacing from the zone's surface is less than 1.5 km (or one mile) [7] (Figure 1).

Cities have been known to have the UHI effect, preferably in areas that are more populated or densely built up than the surrounding countryside [17]. Solar radiation exposure is influenced by the buildings location orientation and the occupied volume of these buildings, and the aspect ratio of

the space between them [18]. The heat produced by human activity and solar radiation congregates as long-wave radiation, which diminishes as a result of the intricate heat transfer betwixt buildings and is trapped betwixt them [19], raising the temperature of the region. Buildings that are close together not only trap heat but also hinder airflow and ventilation, which furthers the phenomenon's intensification [20]. Many studies have demonstrated that air temperature in cities is influenced by surface temperature of municipal superficies materials [14, 21, 22]. The sun frequently heats urban surfaces like pavements and roofs between 27 and 50°C, making them hotter than the air [10, 23]. This heat is progressively released into the environment after being absorbed during the day, which contributes to the UHI effect [24]. All of this occurs because materials' thermal and radiative qualities affect how heat is exchanged in urban environments [9, 18]. Dark-colored materials have a low albedo while white, bright, and reflecting materials have a high albedo [25]. 80 % of the sunlight is absorbed by the pavement and roofs that cover 60 % of urban areas [9]. By evapotranspiration, CO₂ absorption, and giving shade to surfaces exposed to the sun, trees and plants are known to keep the environment cool [10]. Greenery's high albedo contributes to its ability to reflect heat back onto itself. The efficiency of this natural cooling drastically decreases with the loss of green space, causing municipal warming [13, 18, 26]. The UHI impact is more pronounced in clear, calm conditions than in cloudy, windy conditions [27]. When the temperature rises, the relative humidity decreases, resulting in drier air, but when the temperature drops, the air gets wet, resulting in a rise in relative humidity [28].

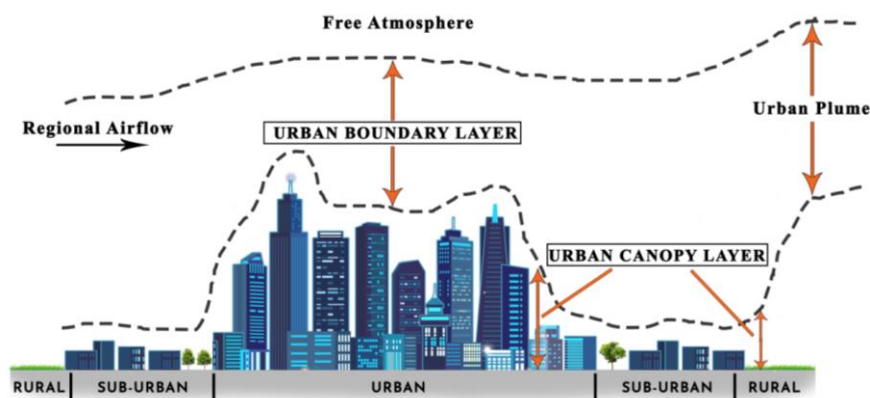


Fig. 1. Two-layer representation of atmospheric air thermal alteration in an municipal setting

Source: Redrawn from (Oke, 1976)

In addition to deteriorating the environment, UHI also affects air quality, human comfort, and the demand for cooling energy, which exacerbates problems like global warming. If the air temperature rises even by 1 °C, then in cities electricity consumption increases on average by 2 to 4 %, according to Akbari *et al.* [29], which creates the need to search for alternative energy sources [30, 31, 32]. The study also showed that, in order to make up for the increase between 0.5 and 3.0 °C in municipal temperature, 5–10 % of the power used in cities is used to cool buildings. When the temperature rises, so do the needs for water for cooling, watering plants, and human consumption [33, 34], as well as for power. Those with low thermal tolerance are susceptible to significant illnesses such as cardiovascular stress, cardio respiratory diseases, heat cramps, blood clots, and, in some circumstances, death due to the extreme heat [35, 36]. With each degree of temperature increase, those who live in such unfavourable conditions have less sleep, which can amount to up to two weeks of insufficient sleep annually and directly contribute to an increase in health morbidities [37, 38]. Thus, the urban heat island effect has been explored to varying degrees in many scientific papers demonstrating the impact of land use/land cover (LU/LC) and green cover on the air quality index [39]; it is shown that the lack of green spaces is the main problem, and this problem will only be exacerbated due to overpopulation associated with the rapid growth of cities [40]; analyzed the law of spatio-temporal evolution and determined the differences between urban heat islands in winter and summer [41]; impact of urban heat islands on heat-related cardiovascular morbidity [42]; explored nighttime urban heat island intensities during Covid-19 lockdown and ecological habitat [43, 44]; investigated the difference between urban and rural heat [45]. However, the authors did not reveal studies of the comparative nature of two districts of the same city located close to each other, but having different characteristics, such as social activity, population density in the area, the degree of development and landscaping of the territory, etc.

The present study is conducted to investigate and assess the effects of UHI on carefully chosen places, namely: Center Point Chauraha and Staff

Club Chauraha, based on local climates for two districts of the city of Aligarh, located close to each other, but have different characteristics. The city of Aligarh is part of the northern Indian state of Uttar Pradesh, around 132 km southeast of New Delhi, and located between the Ganga and Yamuna rivers, in the middle of the doab. Furthermore, to investigate the impact of UHI, this study solely evaluates the relative humidity (%) and ambient dry bulb air temperature in the canopy layer at two specifically chosen locations in Aligarh.

2. MATERIALS AND METHODS

For the purpose of gathering data, two places in Aligarh city were carefully chosen. The microclimatic environmental conditions at these two areas are in contrast to one another. Center Point Chauraha is the first location, designated as L1, while Staff Club Chauraha, on the campus of Aligarh Muslim University, is the second location, designated as L2. The two areas are roughly 3 kilometers apart. Since L1 is a Central Business District (CBD), it receives the majority of the city's foot traffic. The area, which is characterized by both commercial and residential land use, is located in the heart of Aligarh City's high density sector. Due to the paucity of urban vegetation relative to the built-up region, the urban grain of the area is poorly preserved. On the spine route of the A.M.U. campus, L2 sees a fair volume of traffic flow. Compared to other locations, the area around has a high level of vegetation and greenery. In close proximity to the place is a public park.

The information is gathered five times a day, from 9:00 to 12:00, 15:00 to 18:00, and 21:00 to 21:00, for a period of 23 days, from April 22 to May 15, 2022. Due to the unfavorable weather, one day from the survey period – May 4, 2022 – was excluded. To capture and comprehend the urban configuration of the research regions, radial buffer zones of 500m were taken into consideration at both locations. To prevent changes in the microclimate, each survey was finished within 30 minutes. Based on the past research procedures, all the precautions and techniques were used [10, 16, 18, 46]. The UHI intensity across the study period, which varied from morning to night and affected micro-climatic factors depending on distinct urban settings, was then depicted in tables and graphs and compared

using the temperature and humidity measurements from the two locations.

In order to gain information about the causes of thermal discomfort and evidence of microclimatic variation, data are collected utilizing mobile traverse method-portable equipment. During measurements, the apparatus was fixed to a tripod stand that was 1.3 meters above the ground. The sensor was effectively protected from direct sunlight while still ensuring airflow by having a hard cardboard covering it. Before taking readings, the equipment was left in place for a sufficient amount of time to come into balance with its environment.

3. RESULTS AND DISCUSSION

According to analysis of field measurement data, L1 experienced a greater temperature than L2, as indicated in Table 1. The mean temperature difference ranged from 0.87 °C in the morning to 2.23 °C at night (Table 1). As a result, the L1 region exhibits urban warmth, where heat stored during the day is later released into the atmosphere, delaying the cooling of urban space. Given that most past studies have used the same pattern, this UHI pattern justifies the term «urban heat island» [10, 18, 47]. By daybreak, the considerable UHI effect began

to show evident, and urban buildings continued to warm up until late in the day. After that, the temperature lowers significantly while the UHI rises, peaking at night. The highest recorded UHI intensity was 3.1 °C when it was seen at 21:00 hours, and the lowest was 0.6 °C when it was seen at 09:00 hrs (Table 2). This is taking place as a result of Location 1's UHI phenomenon, which causes heat to be absorbed during the day and then slowly released after nightfall. The occurrence at L1 may have existed due to human heat, exposed pavement areas, increased traffic volume, decreased vegetation, and strong traffic influx. Several causes of UHI production have been verified in earlier research [10].

This study indicates that microclimatic variables can have a big impact on temperature and humidity over short distances, as the 3 km used in this study. L1's temperature was consistently higher than L2's (Table 1, Table 2). This is taking place as a result of L1, which is a high-density area with artificial surfaces and little vegetation (Figure 2). Due to large asphalt roadways, exposed dense mass, and few pockets of shade, the sun-exposed surfaces are more prevalent in the L1 area. As a result, L1 urban settings absorb more heat throughout the day and have less long wave cooling afterwards,

Table 1. The difference between the L1 and L2 mean temperatures (°C) at specific three hours' time intervals between 09:00 to 21:00 hrs. during the survey period of 23 days

Mean Temperature Difference (°C)			
Time	Mean Humidity Center Point Chauraha (L1)	Mean Humidity Staffclub Chauraha (L2)	Mean Difference
09:00	36.63	35.76	0.87
12:00	41.80	40.43	1.37
15:00	42.78	41.13	1.65
18:00	37.64	35.80	1.83
21:00	34.00	31.77	2.23
			Average = 1.59

Table 2. Maximum and minimum UHI Intensity (UHII) at selected three hours' time interval between 09:00 to 21:00 hrs. during the survey period of 23 days at L1 and L2

Analysis of UHI Intensity (UHII)		
Time	Maximum UHI	Minimum UHI
09:00	1.4	0.6
12:00	1.8	1.1
15:00	2	1.2
18:00	2.4	1.4
21:00	3.1	1.6

Radial buffer size : 500m , Area: 785398 sq.m.

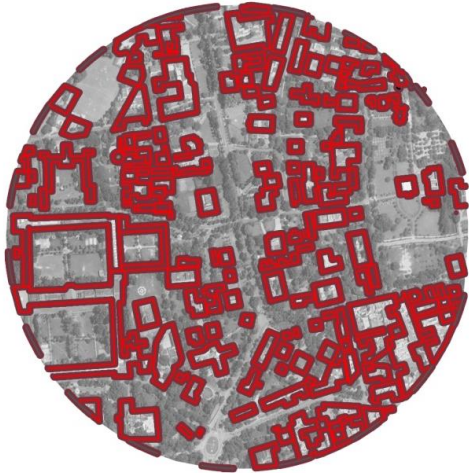
Vegetation Built up Study loca



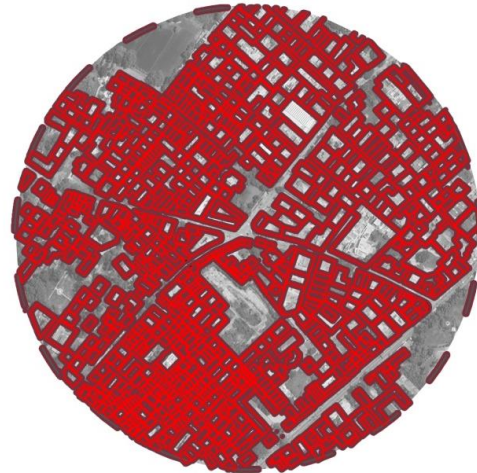
STAFF CLUB CHAURAHA



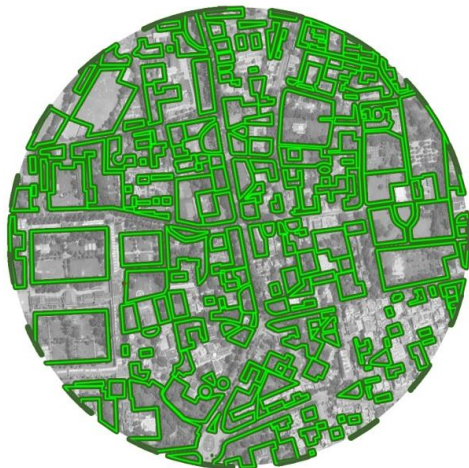
CENTRE POINT CHAURAHA



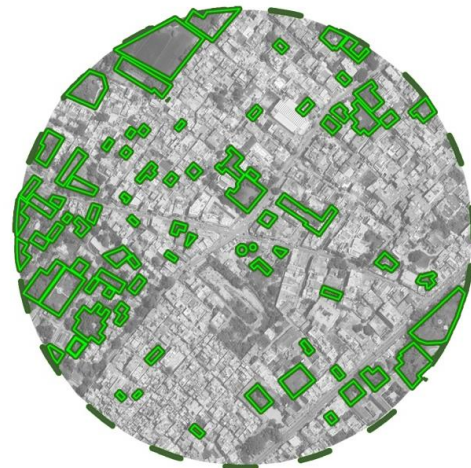
Built up area: 29.25%



Built up area: 58%



Green Coverage: 46.36%



Green Coverage: 15.78%

Fig 2. Picture depicting the built-up and greenery within the considered 500 meters of the research area

which increases the intensity of UHI. Because it has been proven that asphalt absorbs heat during the day and surface temperatures can reach 67 °C [48] and releases heat at night. However, by adding various color pigments, the temperature of the asphalt pavement can be reduced by 5.4 °C per day [49]. As a result of reduced density and high green cover, L2 temperature increased less than L1 temperature throughout the diurnal period and decreased significantly after sunset (Figure 2). The building density of buildings and the used facing materials significantly increase the air temperature of the urban environment [50, 51]. In other words, depending on the spatial composition and urban features, the urban heat island effect and its amplitude might change at lower scales [15, 52].

As shown in Table 3, the mean relative humidity was seen to be rising starting in the evening and was thought to be the case until early in the morning. It was recorded at its lowest point in the late afternoon, typically about 15:30 when the temperature was at its highest. This explains why temperature and relative humidity have an inversely proportional relationship, meaning that as temperature rises, relative humidity decreases, making the air drier [28]. Because L1 had less humidity than L2 (Table 3), paired with an already high temperature, L1's micro-climate is difficult for urban residents to control. This may be taking place because there are more urban materials at L1 than L2, which are less permeable to water.

4. CONCLUSION

The empirical evidence from this study supports the assertion that UHI impact is common in densely populated metropolitan regions. In contrast to L1,

which has a high concentration of greenery and is less densely populated, L2 has a lower temperature rise and higher cooling than L1. Furthermore, this study proves that diurnal temperature variations in built environments occur over relatively small distances and are influenced by urban spatial design. The findings of this study indicate that UHI was found to be more severe after sunset. Understanding the relationship between the specified microclimatic measures, such as ambient dry bulb temperature and relative humidity fluctuations, and microclimatic conditions was made easier by the spatial study of urban fabric at selected places. L1 had lower humidity and a higher temperature pattern than L2 because of the location's weak green cover and water-impermeable surfaces (Table 1, Table 3). Similar findings have been drawn by other researchers who have shown how many environmental factors in urban environments can cause 2 °C microclimatic changes that may indicate serious problems with UHI; who substantiated that temperature fluctuations even by 0.69 °C can be considered significant. According to this study, urban dwellers at L1 can experience significant unfavourable microclimatic conditions due to measured mean temperature differences of 1.37 °C at noon and 1.65 °C at 15:00 hours.

A deeper understanding of microclimatic UHI can be produced by such study endeavors. The important component of healthy and energetic public spaces is a microclimate that is thermally comfortable. Good understanding of daily fluctuations in urban temperature can aid authorities and planners in understanding for better existing and future development. This can be done by transforming existing metropolitan areas in a clever and small-scale manner.

Table 3. Mean relative humidity (%) at L1 and L2, as well as the difference between them at a certain moment throughout the survey period of 23 days

Time	Mean Humidity Data (%)		
	Mean Humidity Center Point Chauraha (L1)	Mean Humidity Staffclub Chauraha (L2)	Mean Difference
09:00	33.01	34.96	1.95
12:00	25.73	27.21	1.49
15:00	23.58	26.43	2.85
18:00	29.80	32.61	2.82
21:00	36.08	40.70	4.63

5. RECOMMENDATIONS

5.1 Altering Roofing Materials – Cool Roofs

Create the idea of cool roofing by replacing heated roof materials with cool materials (high albedo value). According to a National Centre for Atmospheric Research (NCAR) study from 2010, white painted roofs can minimize the UHI effect by 33 %, and if cool roofs can be achieved by changing colour, the cost of the roof is not increased. Engineers at Prude University created a “ultra white” paint in 2021 that can reflect 98.1 % of sunlight, aid in energy conservation, and counteract climate change. This paint can save 10 K.W. of cooling power when applied to a 93 sq.m. roof area.

5.2 Bringing Down Anthropogenic Heat

Human activity produces anthropogenic heat, with sources including illumination, building cooling and heating systems, and moving automobiles [53], which creates the need to search for alternative energy sources [30, 31] in the conditions of the energy crisis. The temperature in metropolitan areas may rise by 2 to 3 °C as a result of this heat [54]. Thus, we can observe a vicious circle, since the earlier manuscript emphasized that the consequences of a one degree increase in air temperature is an increase in energy consumption [29], in addition, building-integrated photovoltaic system panels can potentially increase UHI intensity [30]. Encouraging public transit, limiting the use of private motor vehicles, and switching to cleaner fuels can all help reduce the impact of UHI. It may be more energy efficient to switch to an efficient cooling/heating system like VRF (Variant Refrigerant Flow). They operate quietly, consistently give comfort, take up less room, and offer superior control [55].

5.3 Increasing the Amount of Greenery

Increasing vegetation cover is one of the most effective ways to reduce the effects of heat on the urban environment [56, 57]. Shade, thermal insulation, and noise and air pollution control are all provided by vegetation [58]. Vegetation is observed to reduce the near-surface air temperature by 1-4.7 %, especially when UHI is significant [59, 60].

Another crucial factor to take into account is the selective planting of trees. For cooling, shade, and evapotranspiration, their healthy growth and type of tree must be taken into consideration. Plantations might benefit from shade trees. They have a large canopy and can shade homes and pedestrians while reducing the amount of direct sunlight that hits urban surfaces, keeping the microclimate cool [61]. A mature tree may evapotranspire up to 450 liters of water per day, which is equal to 20 hours of use of a five-star air conditioner [62]. In their simulation study conducted in Canadian cities, Akbari and Taha [61] found that planting 30 % more trees might result in 10 % energy savings from heating and air conditioning. According to Theeuwes et al. [63], temperature typically drops by 0.6 K for every 10 % increase in vegetation.

5.4 More Porous and Permeable Surfaces

Water can percolate through pavement or plant and reach a substrate layer through permeable surfaces, which encourages deep infiltration [64]. These characteristics should reduce temperature to a respectable degree [17]. Turf pavers can be used in place of the typical tiles found on sidewalks, outdoor areas, and parking lots. Further to the water permeability quality, they contribute to the “feel good” quality of green space. Porous concrete paving stones, which not only allow water to get absorbed but also aid trees in consuming nearby water, can be utilized in places where turf tiles are impractical. For pedestrian walkways, porous concrete is advised since it requires less washing for cleaning and maintenance [62].

6. CONFLICT OF INTEREST

The authors declare no conflict of interest.

7. REFERENCES

1. I. Kousis, I. Pigliatile, and A.L. Pisello. Intra-urban microclimate investigation in urban heat island through a novel mobile monitoring system. *Scientific Reports* 11(1): 1–17 (2021).
2. H. Jin, P. Cui, N.H. Wong, and M. Ignatius. Assessing the effects of urban morphology parameters on microclimate in Singapore to control the urban heat island effect. *Sustainability* 10(1): (2018).
3. W.L. Filho, L.E. Icaza, V.O. Emanche, and A.Q. Al-Amin. An evidence-based review of impacts, strategies and tools to mitigate urban heat islands. *International Journal of Environmental Research and Public Health* 14(12): 1–29 (2017).

4. W. Filho, F. Wolf, R. Castro-Díaz, C. Li, V.N. Ojeh, N. Gutiérrez, G.J. Nagy, S. Savić, C.E. Natenzon, A.Q. Al-Amin, M. Maruna, and J. Bönecke. Addressing the urban heat islands effect: A cross-country assessment of the role of green infrastructure. *Sustainability* 13(2): 1–20 (2021).
5. L. Howard. The Climate of London. *International Association for Urban Climate* 1 (1833). https://urban-climate.org/documents/LukeHoward_Climate-of-London-V1.pdf.
6. W.P. Lowry. Empirical Estimation of Urban Effects on Climate: a Problem Analysis. *Journal of Applied Meteorology* 16(2): 129–135 (1977).
7. T.R. Oke. The energetic basic of the urban heat island. *Royal Meteorological Society* 108: 1–24 (1982).
8. P.P. Wong, P.-C. Lai, and M. Hart. Microclimate Variation of Urban Heat in a Small Community. *Procedia Environmental Sciences* 36: 180–183 (2016).
9. U.S Environmental Protection Agency. Urban Heat Island Basics. Reducing Urban Heat Islands: *Compendium of Strategies* 1–22 (2008).
10. L. Gartland. Heat Islands: Understanding and mitigating heat in urban areas. *Earthscan: Taylor & Francis Group, an informa business, Uk and USA* (2008).
11. IPCC. Climate Change 2014: Impacts, Adaptation, and Vulnerability. Part A: Global and Sectoral Aspects. Contribution of Working Group II to the Fifth Assessment Report of the Intergovernmental Panel on Climate Change (AR5 ed.). *Cambridge University Press* (2014).
12. IPCC. Climate Change 2022 : Impacts , Adaptation and Vulnerability. Contribution of Working Group II to the Sixth Assessment Report of the Intergovernmental Panel on Climate Change. *Cambridge University Press* (2022).
13. G. Jain, and S. Sarkar. Urban Heat Island: Causes, Effects & Mitigating Strategies. *Imperial Journal of Interdisciplinary Research (IJIR)* 3(5): 2098–2103 (2017).
14. S. Kawashima, T. Ishida, M. Minomura, and T. Miwa. Relations between surface temperature and air temperature on a local scale during winter nights. *Journal of Applied Meteorology* 39(9): 1570–1579 (2000).
15. E. Erell, D. Pearlmutter, and T. Williamson. Urban Microclimate: Designing the Spaces Between Buildings (1st ed.). *Earthscan Routledge* (2011).
16. S. Sahu, A.S. Pawar, and M. Mukherjee. Urban Heat Island Investigation: Techniques and Methods so Far. *Architecture Time Space and People* 14(3): 16–22 (2014).
17. M. Nuruzzaman. Urban Heat Island: Causes, Effects and Mitigation Measures - A Review. *International Journal of Environmental Monitoring and Analysis* 3(2): 67 (2015).
18. A. Soltani, and E. Sharifi. Daily variation of urban heat island effect and its correlations to urban greenery: A case study of Adelaide. *Frontiers of Architectural Research* 6(4): 529–538 (2017).
19. A. Coutts, J. Beringer, and N. Tapper. Changing Urban climate and CO2 emissions: Implications for the development of policies for sustainable cities. *Urban Policy and Research* 28(1): 27–47 (2010).
20. R. Priyadarsini, W.N. Hien, and C.K.W. David. Microclimatic modeling of the urban thermal environment of Singapore to mitigate urban heat island. *Solar Energy* 82(8): 727–745 (2008).
21. I.R. Imamura. Air Surface Temperature Correlations. In Controlling summer heat islands. *Lawrence Berkeley Laboratory* (1989).
22. R. Watkins, M. Kolokotroni, J. Palmer, and P. Littlefair. The London Heat Island — Surface and Air Temperature Measurements in a Park and Street Gorges. *ASHRAE Transactions* 108: 419–427 (2002).
23. P. Berdahl, and S.E. Bretz. Preliminary survey of the solar reflectance of cool roofing materials. *Energy and Buildings* 25(2): 149–158 (1997).
24. T. Asaeda, and V.T. Ca. Heat storage of pavement and its effect on the lower atmosphere. *Atmospheric Environment* 30(3): 413–427 (1996).
25. M.E. Hulley. The urban heat island effect: Causes and potential solutions. *Metropolitan Sustainability* 79–98 (2012).
26. N.H. Wong, and S.K. Jusuf. Study on the microclimate condition along a green pedestrian canyon in Singapore. *Architectural Science Review* 53(2): 196–212 (2010).
27. S. Tumanov, A. Stan-Sion, A. Lupu, C. Soci, and C. Oprea. Influences of the city of Bucharest on weather and climate parameters. *Atmospheric Environment* 33: 4173–4183 (1999).
28. S. Valsson, and A. Bharat. Impact of Air Temperature on Relative Humidity - A study. *Architecture - Time Space & People* February: 38–41 (2011).
29. H. Akbari, M. Pomerantz, and H. Taha. Cool surfaces and shade trees to reduce energy use and improve air quality in urban areas. *Solar Energy* 70(3): 295–310 (2001).
30. T.S. Elhabodi, S. Yang, J. Parker, S. Khattak, B.J. He, and S. Attia. A review on BIPV-induced temperature effects on urban heat islands. *Urban Climate* 50: (2023).
31. V. Vambol, A. Kowalczyk-Juško, K. Józwiakowski, A. Mazur, S. Vambol, and N.A. Khan. Investigation in Techniques for Using Sewage Sludge as an Energy Feedstock: Poland's Experience. *Ecological Questions* 34(1): 91–98 (2023).
32. S. Vambol, Y. Shakhov, V. Vambol, and I. Petukhov.

- A mathematical description of the separation of gas mixtures generated by the thermal utilization of waste. *Eastern-European Journal of Enterprise Technologies* 1(2/79): 35–41 (2016).
33. R.C. Balling, P. Gober, and N. Jones. Sensitivity of residential water consumption to variations in climate: An intraurban analysis of Phoenix, Arizona. *Water Resources Research* 44(10): 1–11 (2008).
 34. R.A. Khan, R. El Morabet, J. Mallick, M. Azam, V. Vambol, S. Vambol, and V. Sydorenko. Rainfall Prediction using Artificial Neural Network in Semi-Arid mountainous region, Saudi Arabia. *Ecological Questions* 32(4): 127–133 (2021).
 35. R. Basu. High ambient temperature and mortality: A review of epidemiologic studies from 2001 to 2008. *Environmental Health* 8(1): (2009).
 36. J.A. Patz, D. Campbell-Lendrum, T. Holloway, and J.A. Foley. Impact of regional climate change on human health. *Nature* 438(7066): 310–317 (2005).
 37. K. Minor, A. Bjerre-Nielsen, S.S. Jonasdottir, S. Lehmann, and N. Obradovich. Rising temperatures erode human sleep globally. *One Earth* 5(5): 534–549 (2022).
 38. A.M. Hrynzovskyi, I.A. Holovanova, S.T. Omelchuk, O.V. Kuzminska, A.A. Hrynzovska, O.O. Karlova, and V.Y. Kondratiuk. Public health and social supervision issues within public administration of ukrainian territories in the late 8th-early 9th centuries. *Wiadomosci Lekarskie (Warsaw, Poland: 1960)* 71(1 pt 2): 246–251 (2018).
 39. A. Kausar, A. Afzal, G. Saeed, A. Maqsoom, O.I. Khan, S. Afsar, V. Vambol, and S. Vambol. Land-Use/Land Cover Analysis Through Object Based Technique: A Case Study of Shahrah-e-Faisal. *Ecological Questions* 34(2): 1–15 (2023).
 40. H. Arif, A. Kausar, A. Afzal, S.R. Ahmed, S. Afsar, A.H. Lahori, S. Vambol, and V. Vambol. Geospatial techniques for comparative case study of spatiotemporal changes in New Karachi and North Karachi parks. *Ecological Questions* 34(4): 1–9 (2023).
 41. S. Yuan, Z. Ren, X. Shan, Q. Deng, and Z. Zhou. Seasonal different effects of land cover on urban heat island in Wuhan's metropolitan area. *Urban Climate* 49: 101547 (2023).
 42. S.E. Cleland, W. Steinhardt, L.M. Neas, J.J. West, and A.G. Rappold. Urban Heat Island Impacts on Heat-Related Cardiovascular Morbidity: A Time Series Analysis of Older Adults in US Metropolitan Areas. *Environment International* 178: 108005 (2023).
 43. Z. Feng, X. Wang, J. Yuan, Y. Zhang, and M. Yu. Changes in air pollution, land surface temperature, and urban heat islands during the COVID-19 lockdown in three Chinese urban agglomerations. *Science of The Total Environment* 892: 164496 (2023).
 44. S. Khan, R. Srivastava, A.R. Khan, and A.M. Hrynzovskyi. Study of Covid-19-Related Ecological Habitat of College Students: A Survey. *Ecological Questions* 34(2): 1–15 (2023).
 45. G. Calis, S.A. Yildizel, and U.S. Keskin. Investigation of color pigment incorporated roller compacted high performance concrete as a mitigation tool against urban heat island. *Case Studies in Construction Materials* 17: e01479 (2022).
 46. J. Voogt. How Researchers Measure Urban Heat Islands. *Department of Geography, University of Western Ontario, London* (2000).
 47. P.P.Y. Wong, P.C. Lai, C.T. Low, S. Chen, and M. Hart. The impact of environmental and human factors on urban heat and microclimate variability. *Building and Environment* 95: 199–208 (2016).
 48. N. Anting, M.F.M. Din, K. Iwao, M. Ponraj, K. Jungan, L.Y. Yong, and A.J.L.M. Siang. Experimental evaluation of thermal performance of cool pavement material using waste tiles in tropical climate. *Energy and Buildings* 142: 211–219 (2017).
 49. T. Karlessi, M. Santamouris, K. Apostolakis, A. Synnefa, and I.J.S.E. Livada. Development and testing of thermochromic coatings for buildings and urban structures. *Solar Energy* 83(4): 538–551 (2009).
 50. J. Feng, K. Gao, S. Garshasbi, T. Karlessi, A. Pyrgou, G. Ranzi, M. Santamouris, A. Synnefa, and G. Ulpiani. Urban Heat Island and Advanced Mitigation Technologies. *Comprehensive Renewable Energy (Second Edition)* 3: 742–767 (2022).
 51. M. Taleghani, M. Tenpierik, A. van den Dobbelsteen, and D.J. Sailor. Heat in courtyards: A validated and calibrated parametric study of heat mitigation strategies for urban courtyards in the Netherlands. *Solar Energy* 103: 108–124 (2014).
 52. T.R. Oke. Towards better scientific communication in urban climate. *Theoretical and Applied Climatology* 190: 179–190 (2006).
 53. P. Shahmohamadi, A.I. Che-Ani, K.N.A. Maulud, N.M. Tawil, and N.A.G. Abdullah. The Impact of Anthropogenic Heat on Formation of Urban Heat Island and Energy Consumption Balance. *Urban Studies Research* 2011: 1–9 (2011).
 54. H. Taha. Urban climates and heat islands: Albedo, evapotranspiration, and anthropogenic heat. *Energy and Buildings* 25(2): 99–103 (1997).
 55. A. Teke, and O. Timur. Assessing the energy efficiency improvement potentials of HVAC systems considering economic and environmental aspects at the hospitals. *Renewable and Sustainable Energy Reviews* 33: 224–235 (2014).
 56. A. Dimoudi, and M. Nikolopoulou. Vegetation in the urban environment: Microclimatic analysis and benefits. *Energy and Buildings* 35(1): 69–76 (2003).

57. F. Wilmers. Green for melioration of urban climate. *Energy and Buildings* 11(1–3): 289–299 (1988).
58. M. Roth. Urban heat islands. *Handbook of Environmental Fluid Dynamics* 2: 67–75 (2013).
59. L. Kleerekoper, M. Van Esch, and T.B. Salcedo. How to make a city climate-proof, addressing the urban heat island effect. *Resources, Conservation and Recycling* 64: 30–38 (2012).
60. X.X. Li, and L.K. Norford. Evaluation of cool roof and vegetations in mitigating urban heat island in a tropical city, Singapore. *Urban Climate* 16: 59–74 (2016).
61. H. Akbari, and H. Taha. The impact of trees and white surfaces residential heating and cooling energy use in four canadian cities. *Heat Island Project* 17(2): 141–149 (1992).
62. M. Giguère. Urban Heat Island Mitigation Strategies. *Institut national de santé publique du Québec* (2009).
63. N.E. Theeuwes, G.-J. Steeneveld, R.J. Ronda, and B. Holtslag. A diagnostic equation for the daily maximum urban heat island effect for cities in northwestern Europe. *International Journal of Climatology* 37(1): 443–454 (2016).
64. B. Albanese, and G. Matlack. Utilization of parking lots in Hattiesburg, Mississippi, USA, and impacts on local streams. *Environmental Management* 24(2): 265–271 (1999).



Flow Control in a Rectangular Open Channel using Two Impermeable Spur Dikes: A Numerical Study

Hafiz Syed Moazzum Gillani¹, Zain-ul-Hassan¹, Hafiz Rana Azeem Sarwar², Muhammad Sohail Jameel^{1*}, Waqar Hasan¹, Ehsaan Manzoor¹, and Imran Khan¹

¹Department of Transportation Engineering and Management, University of Engineering and Technology, Lahore, Pakistan

²Department of Civil Engineering, Islamic International University, Islamabad, Pakistan

Abstract: The present study examines how adjusting vegetation patches in a rectangular open channel with two impermeable spur dikes alters the displacement of the recirculation region. The Reynolds stress turbulence model is implemented via the 3D numerical code FLUENT (ANSYS). Mean stream-wise velocity profiles were drawn at selected positions and at mid of flow depth i.e., 3.5 cm, a horizontal plane is cut through the open channel for analyzing velocity contours and streamline flow. The findings indicate that the stream-wise velocity profiles showed fluctuations in the presence of different shapes and arrangement of cylindrical patch discussed and the maximum velocity within the field of spur dike is of the order of 0.018 m/s due to the prism shape. By changing the position of the cylindrical patch, the location of the recirculation region displaces within the field of impermeable spur dike.

Keywords: Recirculation Region, Vegetation Patches, Impermeable Spur Dikes, Rectangular Open Channel, Flow Control in Open Channels.

1. INTRODUCTION

The essential sources of water are rivers as well as channels for a long period. To make water accessible, the human beings used to live near rivers and channels which served the purpose of transferring water to far areas. The previous reason makes it essential to protect the channels and rivers from erosion as well as their deterioration due to flowing water. Researchers from diverse scientific disciplines such as Hydraulics, Hydrology, Geology, and Sedimentology have collectively worked to demonstrate that comprehensively analyzing river channels and their historical behaviors, along with foundational scientific and technical investigations, is distinctly separate when aiming to optimize the utilization of these crucial water resources. Spur dikes are the hydraulic structures used for river training and bank protection works. The use of spur dikes from long ago shows that this kind of structure has wide benefits. By constructing the spur dike, the flow path contracts, and resultantly

the flow velocity near the structure increases which leads to increased average velocity in the contracted section. This is why using spur dikes is a good solution for managing how rivers flow, controlling the movement of water and passage of water under bridges, and preventing the erosion of river banks and edges [1].

Spur dikes are commonly used in channels to prevent the erosion of channel beds and banks by fixing them at the right angle to the direction of flow in order to reduce the velocity of flow. These are considered among the best structures of hydro engineering for prevention and diversion of water. The Spur Dikes are of two types: Pervious Spur Dikes and Impervious Spur Dikes, based on the fact that the structure is pervious or not. Generally, construction material used for spur dikes are bamboo, steel, timber, RCC piles etc. Permeable Spur dikes are considered economical and found their application in temporary works. Construction materials for impervious spur dikes are stones, soils

(local), gravels, rocks, and local materials (easily available). An approaching flow is prevented or diverted through impervious spur dikes. Although water can pass through pervious spur dike, but it reduces the water speed. Either the spur dikes are covered by water or not, these are classified as submerged and non-submerged type. If the spur dike is covered by water, then this is referred as submerged spur dike. If the spur dike is not fully covered by water, it is known as non-submerged spur dikes. Based on the shape, spur dikes may have shape like hocky shape, T-shape, mole-head as well as L-shape. Again based on function of spur dikes against water, the dikes are classified as diverting type, repelling type and attracting type. A downstream-facing (Attractive) spur dike exerts an attractive force, causing the flow to be diverted from its original path. In this way, it makes the flow of water towards the center of channel. A deflection spur dike is strategically positioned with its upstream end facing the flow of the river. Its purpose is to redirect the water away from the riverbank in order to mitigate erosion by redirecting the water flow. Consequently, the repelling spur dike is anchored perpendicular to the flow's direction [2].

Variations in the water bodies (i.e., river) beds and banks results due to different features such as shape of channel (width, depth), the material from which river bed is made-up, amount of sediment carried by water bodies. In the past, researchers simulated actual flow conditions in open channels with different flow conditions so that properties of flow under different conditions can be determined. In this regard, Koken *et al.* [3] employed an impermeable spur dike within a horizontal plane, utilizing two-dimensional velocity vectors, to examine flow mechanisms downstream. Exploring flow patterns around both individual and arrays of water-resistant spur dikes, Kafle *et al.* [4] employed different turbulent closure models. Teraguchi *et al.* [5] analyzed the impact on flow velocity distribution around pervious and impervious spur dikes, as well as bandal-like structures, under two conditions: one where these were non-submerged, and the other where the submerged state prevailed. At downstream, the vortex zone formed around one impervious spur dike was investigated using RNG (Re-Normalization Group model) turbulence method by Giglou *et. al* [1]. When water passed

through impervious spur dike, it resulted into vortex zone formed around impervious spur dike of four times the length of spur dike. This caused decrease in flow velocity of silt which caused deposition of silt. With passage of time, due to silt deposition the spur dike field would be filled with silt. This becomes the reason of reduction in flood carrying capacity of rivers. RSM (Reynold's Stress Model) was used by many researchers in the past to study the velocity flow characteristics in open channels [6-8]. Around two impervious spur dikes, the distribution of momentum as well as mass horizontally and vertically was done by using LES model (Large Eddy Simulation) [9]. Vaghefi *et al.* [10] used computational fluid dynamic (CFD) model to simulate that how water flows around a T-shaped barrier in a river bend, while considering nearby structures that either attract or repel the water. The simulation accurately predicted the average water velocities near the barrier, indicating its reliability for studying flow patterns around river bends with similar barriers. The results showed that the maximum shear stress on the barriers increased by 23.5 % for attractive structures and 17.6 % for repelling structures compared to vertical ones [10]. Karami *et al.* [11] worked on reduction of the erosion depth around a series of existing barriers in a river. They conducted experiments with an additional barrier placed upstream of the first one. They tested different designs by varying the size, length, angle, and spacing of the protective barriers under different water conditions. The results showed that a well-designed protective barrier can effectively reduce the maximum erosion depth around the main barriers, and specific design recommendations were provided based on the experiment's findings. [11]. Ning *et al.* [12] examined how the spacing between spur dikes affects the depth of erosion and flow characteristics. They found that the greatest erosion occurs near the first spur dike, and increasing spacing reduces its protective effect. The bed shear stress significantly influences the erosion process, as evidenced by correlation analysis. This factor also helps establish the optimal spacing for spur dikes, given that within the primary flow area, the maximum flow velocity is twice that of the incoming velocity. [12]. Esmaeli *et al.* [13] conducted a study to explore how modifying flow patterns through the use of spur dikes can help control erosion and protect river banks. The

study encompassed the creation of a laboratory meandering channel with the incorporation of five spur dikes, aiming to explore how erosion control is influenced by variations in both permeability and length [13]. Bora and Kalita [14] formulated a simulation-optimization framework aimed at identifying the most effective arrangement of groynes concerning their quantity, dimensions, and placements. This approach was designed to manage riverbank erosion successfully. The model minimizes construction costs while ensuring low flow speed in a specific zone to prevent erosion. The model utilizes the shallow water equations and a genetic algorithm for optimization, producing logical results and demonstrating its potential for real-world applications [14] lengths and positions for controlling bank erosion. The vulnerable bank is considered to be protected if a very small value of water flow speed is achieved on the near bank area. A linked simulation-optimization model is developed in this regard which minimizes the total construction cost of the groyne project. At the same time, a constraint in terms of low flow speed in a predefined zone is incorporated, which helps in bank erosion prevention. In the simulation model, the depth-averaged shallow water equations are solved using a finite difference scheme. The optimization problem is formulated in three different approaches to tackle different types of in situ field problems. Genetic algorithm (GA. Nayyer *et al.* [15] examined the flow characteristics around spur dikes of different shapes (I, L, T) arranged in series, both through experimental and numerical methods. It was determined that when employing a mix of (LTT) spur dikes, the most notable outcome was the reduction in velocity, shear stress, and turbulence intensity. This implies that the incorporation of different geometries in combination can effectively mitigate erosion and increase sedimentation amidst spur dikes [15]. Shamloo and Pirzadeh [16] investigated the behavior of subcritical flow around an indirect groyne by altering its installation angles. The objective was to analyze how these adjustments influence the extent of the separation zone that forms behind the groyne. By employing 3D simulations within the Fluent software, researchers observed a substantial influence of the angle of groyne installation on separation length. These findings exhibited a strong agreement with experimental data. The observed separation length was roughly 12 times that of a 0.3 m long impermeable

groyne. The angle that yielded optimal results was approximately 5 degrees, as indicated by Shamloo and Pirzadeh [16]. Zhang *et al.* [17] performed a series of experiments to explore the effects of single spur dikes, both permeable and impermeable, on beds prone to erosion. Their results indicated that the impermeable spur dike caused a maximum scour depth around it that was 50 % greater in comparison to the permeable spur dike [17]. Yang *et al.* [18] explored how the arrangement of permeable spur dikes within a river bend influences the highest water depth upstream. Their research indicated that placing the spur dikes at the midpoint of the bend, oriented at a 75° angle, specifically where the dike met the outer bank of the bend, caused formation of the greatest maximum depth of water [18].

The previous studies have dealt only with changes in river's morphology, pattern of mean velocity and resistance of flow [19-20]. With bridge pier and single impervious spur dike, the characteristics of flow as well as changes in morphology can be examined [21 In mountainous regions, the impervious spur dike has the advantage of non-formation of recirculation region around it but a slow flow field on the downstream side. Other models i.e., $k-\epsilon$ (epsilon model) and LES model were utilized to determine the maximum turbulent kinetic energy and scour hole at and around an impervious spur dike [9,17]. The reason of failure of impervious spur dike in alluvial rivers is scour hole of larger depth. It can be seen in Sangha Bridge Taunsa, Pakistan. All these models provide flow characteristics under specific conditions and do not provide information about recirculation zones behavior. In order to cope up with this, the present studies examine a model through we get complete information about the behavior of flow i.e., flow characteristics and recirculation zones behavior, by using different patches of dissimilar shapes at different positions within two impervious spur dikes.

2. METHODOLOGY

2.1 Equations for Numerical Simulation

The flow of water for the numerical simulation is assumed to be steady and incompressible. The Reynolds governing equations for numerical simulation are given below:

The flow of water for the numerical simulation is assumed to be steady and incompressible. The Reynolds governing equations for numerical simulation are given below:

The Continuity equation is:

$$\frac{\partial U_i}{\partial x_i} = 0$$

The Momentum equation is:

$$U_j \frac{\partial}{\partial x_j} (U_i) = \frac{\nu}{\rho} \frac{\partial}{\partial x_j} \left(\frac{\partial U_i}{\partial x_j} + \frac{\partial U_j}{\partial x_i} \right) - \frac{1}{\rho} \frac{\partial P}{\partial x_i} + (-\rho u_i u_j)$$

where $\frac{\partial R_{ij}}{\partial t}$ is the rate of change of Reynolds stresses, C_{ij} represents the convective transport, P_{ij} signifies the generation rate of Reynolds stresses, D_{ij} accounts for stress transport due to diffusion, ε_{ij} reflects the rate at which stresses dissipate, Π_{ij} characterizes the distribution of stresses resulting from interactions between turbulent pressure and strain and Ω_{ij} denotes the distribution of stresses due to rotational effects. where U_i and U_j stands for the time-averaged velocity component along the x_i and x_j direction, ν and ρ are the kinematic viscosity and density of the water respectively, P corresponds to pressure, and $-\rho u_i u_j$ corresponds to the Reynolds stresses. The convective term is as follows:

$$C_{ij} = \frac{\partial (\rho U_k \overline{u_i u_j})}{\partial x_k}$$

The production term is:

$$P_{ij} = -(R_{im} \frac{\partial U_j}{\partial x_m} + R_{jm} \frac{\partial U_i}{\partial x_m})$$

The representation of the diffusion term is structured as follows:

$$D_{ij} = \frac{\partial}{\partial x_m} \left(\frac{\nu_t}{\sigma_k} \frac{\partial R_{ij}}{\partial x_m} \right)$$

where, $\nu_t = C_\mu \frac{k_2}{\varepsilon}$, $C_\mu = 0.09$ and $\sigma_k = 1.0$.

The representation of the dissipation rate is structured as follows:

$$\varepsilon_{ij} = \frac{2}{3} \varepsilon \delta_{ij}$$

where ε symbolizes the rate of dissipation of turbulent kinetic energy and δ_{ij} corresponds to the Kronecker

delta. This delta δ_{ij} is equal to 1 when i equals j , and it is 0 when i is not equal to j .

$$\prod_{ij} = -C_1 \frac{\varepsilon}{k} \left(R_{ij} - \frac{2}{3} k S_{ij} \right) - C_2 \left(P_{ij} - \frac{2}{3} P \delta_{ij} \right)$$

where C_1 and C_2 are 1.8 and 0.6, respectively. The turbulent kinetic energy k can be represented through the summation of three normal stresses:

$$k = \frac{1}{2} (\overline{u_i'^2} + \overline{u_j'^2} + \overline{u_k'^2})$$

The term of the rotation is given by:

$$\Omega_{ij} = -2\omega_k (\overline{u_j u_m} e_{ikm} + \overline{u_i u_m} e_{jkm})$$

The symbol ω_k represents the rotational vector, while e_{ijk} is known as the alternating symbol. This symbol e_{ijk} takes on a value of +1 when the indices i , j , and k follow a cyclic order and are distinct from each other. Conversely, when the indices i , j , and k are distinct but follow an anti-cyclic order, the alternating symbol e_{ijk} equals to -1. When any two indices among i , j , and k are identical, the alternating symbol takes on a value of 0.

2.2 Open Channel Specifications

To simulate the water flow for the analysis, the geometry of rectangular open channel is shown in Figure 1. The length of the open channel is 56 cm and the width is 96 cm. The maximum flow height is 7 cm. The spur dikes of specifications (4 x 24 x 7) cm were placed perpendicular to the mainstream as shown in Figure 1. The rectangular spur dikes are of impermeable nature which means that flow cannot pass through them. Within the field of impermeable spur dikes, vegetation patches (24 x 12 x 7) cm were placed at three positions bottom, middle and top. At each position, the arrangement and shapes were changed to investigate the displacement of recirculation region. The specifications for different shapes i.e., circular, prism, rectangular and different arrangements are shown in Figures 2-4.

The model was investigated such that each shape was placed at every position with both arrangements. So, for a total of 18 cases, the displacement of recirculation region was investigated through Reynold's stress turbulence model developed by

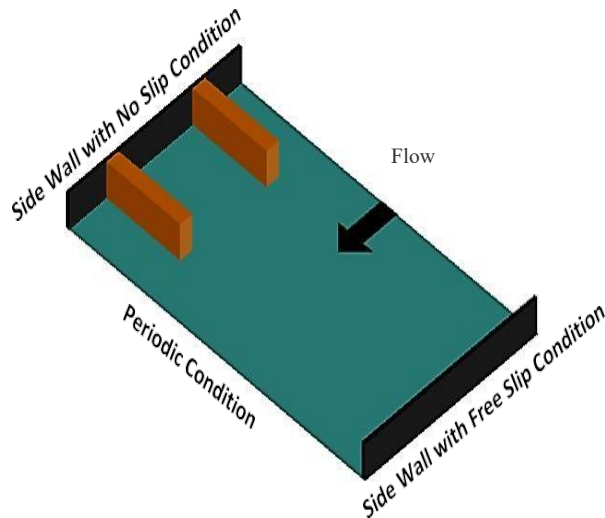


Fig. 1. Arrangement for numerical simulation

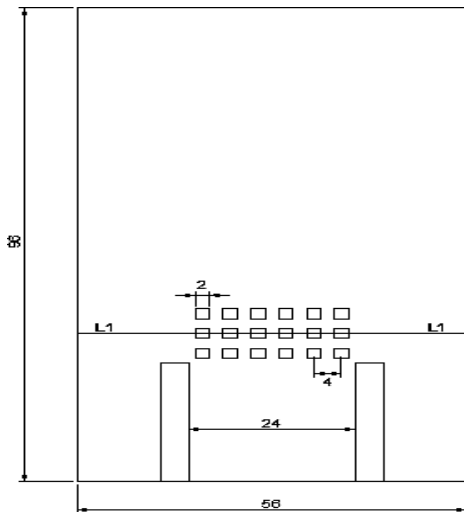


Fig. 2. Rectangular top patch with linear arrangement

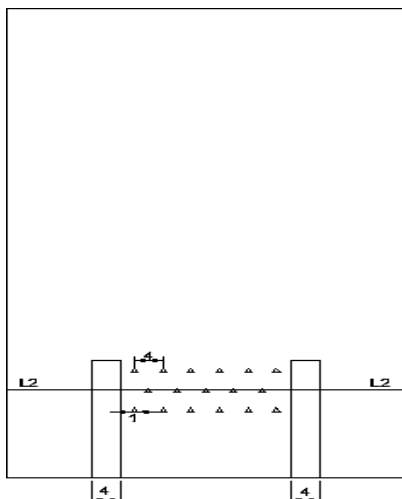


Fig. 3. Prism middle patch with staggered arrangement

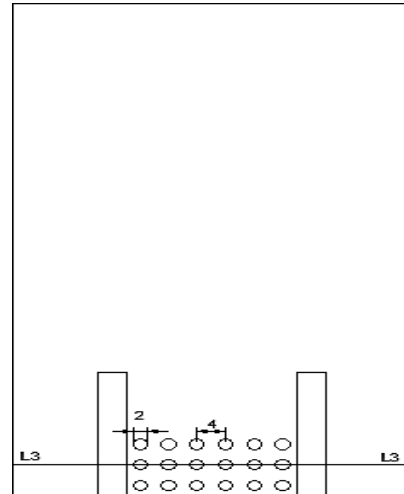


Fig. 4. Circular bottom patch with linear arrangement

three dimensional (3-D) numerical code FLUENT (ANSYS). At positions L1 (top), L2 (middle) and L3 (bottom) shown in Figures 2-4, the mean stream wise velocity profiles were drawn and at mid of flow depth i.e., 3.5 cm, a horizontal plane is made cut through the open channel for analyzing velocity contours and streamline flow.

3. RESULTS AND DISCUSSION

3.1 Mean Flow Characteristics

The mean stream wise velocity profiles for the total of 18 cases at the selected positions L1 (top), L2 (middle) and L3 (bottom) shown in Figures 2-4 are presented in Figure 5. From Figure 5, it can be clearly seen that at a certain position irrespective of the shape and arrangement of vegetation patch, the velocity profiles are somewhat similar. In other words, the shape and arrangement of the vegetation patch does not have significant influence on the velocity profile at a certain position. However, by changing the position of the vegetation patch, all three shapes and their respective arrangements show a change in the velocity profile. In Figure 5 (a-i) i.e., at the bottom position of the patch, all three shapes follow a similar velocity profile. The velocity at the upstream side is quite high than the downstream side, also within the field of impermeable spur dikes, the velocities are quite low. In Figure 5 (a-ii) for the staggered arrangement there is little variation in all three velocity profiles against each other with the prism shape showing the highest velocity profile. Also, within the field of

impermeable spur dikes, the fluctuations are more than with the linear arrangement with the prism shape showing more fluctuations than circular and rectangular shapes. In Figure 5 (b-i) i.e., at the middle position of the patch, the velocity profiles start at quite low values, then rapidly achieve peak velocities in comparison to the bottom position with the circular shape having the most peak velocity

profile at both upstream and downstream side. In Figure 5 (b-ii), in case of staggered arrangement, all shapes follow the same trend for velocity profile similar to figure 5 (a-ii) but with the difference of having more peakedness added to the velocity profiles. In Figure 5 (c-i) i.e., at the top position, all three shapes show significant variation in velocity profiles at both upstream, downstream and within

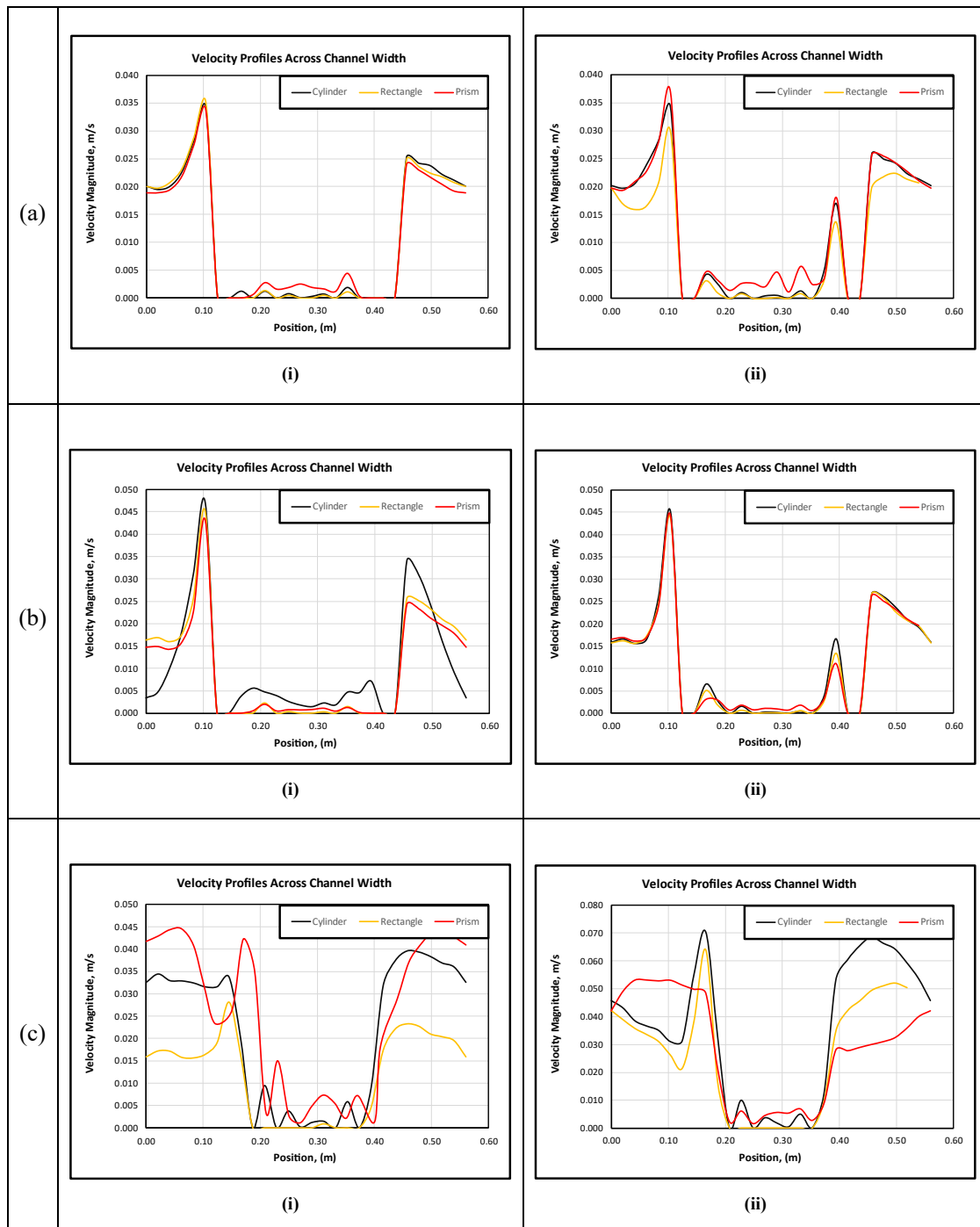


Fig. 5. Mean stream-wise velocity profiles i.e., across channel width 56 cm, (a) Patch position bottom (b) Patch position middle (c) Patch position top, (i) Linear arrangement (ii) Staggered arrangement

the field of impermeable spur dikes with the prism shape showing the most fluctuations throughout the stream flow and higher velocity than circular and rectangular shapes. In Figure 5 (c-ii), there is similar variation in the velocity profiles to that shown in 5 (c-i) but here, it can be concluded that out of all the 18 cases, this case where there is maximum velocity at both upstream and downstream side of the spur dikes and this highest velocity profile is shown by circular shape. Throughout all the cases the maximum velocity within the field of spur dike is of the order of 0.018 m/s which is quite low and can be the cause of recirculation regions formed within the field of impermeable spur dike.

3.2 Velocity Streamlines Characteristics

Next the recirculation regions are shown with the help of streamlines drawn on a horizontal plane

at 3.5 cm of the maximum flow depth of 7 cm. At 3.5 cm that is the mid of flow depth (7 cm) a horizontal plane is cut through the entire open channel to visualize and observe the velocity streamlines around the spur dikes and vegetation patches as shown in Figure 6. The streamlines are shown for each shape at every position but only for linear arrangement as it is evident from the above discussion that the arrangement does not play significant role in altering the flow properties. The same streamlines can be assumed for the staggered arrangement. In Figure 6a, for the top patch position the recirculation region displaces as the shape of the vegetation patch is changed. In case of circular position, the recirculation region is somewhat in the middle of the field of impermeable spur dikes. As for rectangular shape, the recirculation is exactly at center and slightly above the middle of the field. While in the third case that is for prism

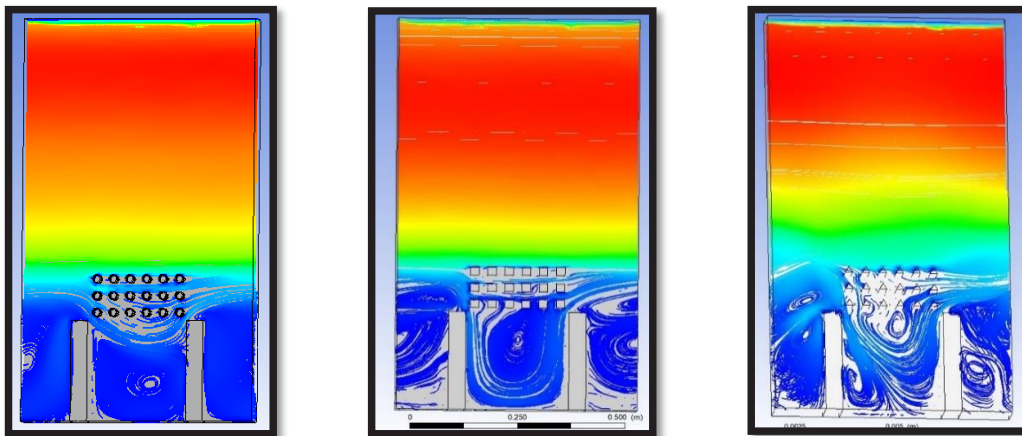


Fig. 6a. Patch position top with linear arrangement, Left (Circular), Middle (Rectangular), Right (Prism)

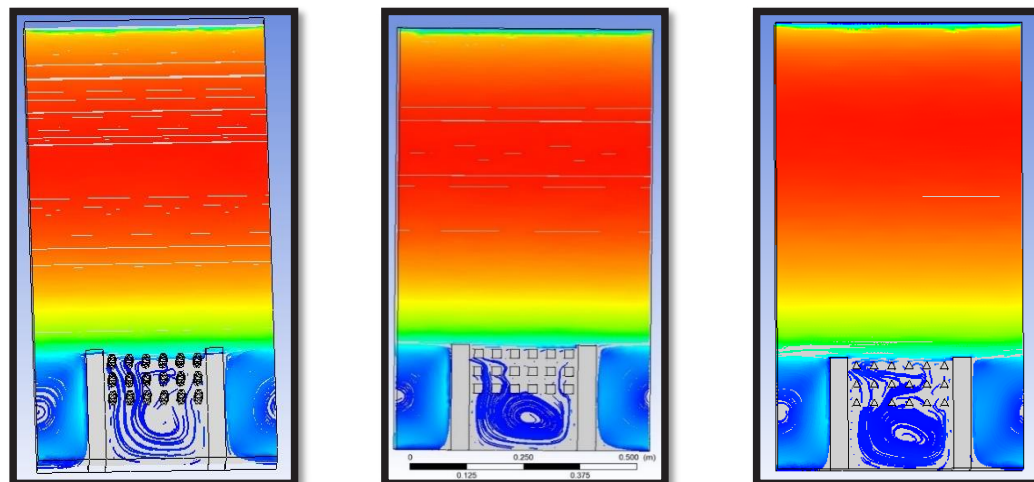


Fig. 6b. Patch position middle with linear arrangement, Left (Circular), Middle (Rectangular), Right (Prism)

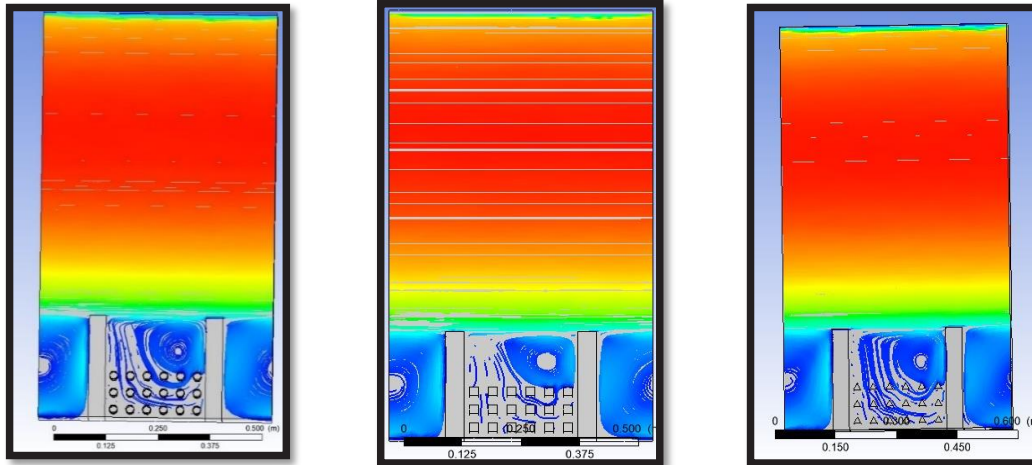


Fig. 6c. Patch position bottom with linear arrangement, Left (Circular), Middle (Rectangular), Right (Prism)

shape, there is a lot of turbulence, and more than one recirculation regions can be observed within the field of spur dikes. In Figure 6b, the position of recirculation region is same irrespective of the shape of vegetation patch for all three shapes the recirculation region is located in the middle of the field of impermeable spur dikes. However, the shape of recirculation region is not so prominent in case of the circular shape. In Figure 6c, for the bottom patch position, the location of recirculation region is identical for all three shapes i.e., top right corner of the field of two spur dikes. However, it can be noticed that for rectangular shape the shape of recirculation is bigger than for prism shape and that is in turn bigger than that for the circular shape.

4. CONCLUSION

The present investigation relates to study of the flow behavior in an open channel within impermeable spur dikes with vegetation patches of different shapes (circular, rectangular, prism) and arrangements (Linear and Staggered) laid in the field of the spur dikes at three different positions top, middle, and bottom. The main conclusions drawn out of this study are as following:

- i. At a certain position irrespective of the shape and arrangement of vegetation patch, the velocity profiles are somewhat similar. In other words, the shape and arrangement of the vegetation patch does not have significant influence on the velocity profile at a certain position. By altering the vegetation patch position, the circular, rectangular, and prism shapes, along with

their respective arrangements, exhibit changes in velocity profiles.

- ii. Throughout all the 18 cases discussed, the maximum velocity within the field of spur dike is of the order of 0.018 m/s due to the prism shape. This is quite low and can be the cause of recirculation zones within the region of spur dikes causing siltation.
- iii. By changing the position of the vegetation patch, the location of recirculation region displaces within the field of impermeable spur dike. However, at a certain position, by changing the shapes and arrangement of vegetation patch, the location and shape of recirculation region is almost identical.

5. CONFLICT OF INTEREST

The authors declare no conflict of interest

6. REFERENCES

- 1 A.N. Giglou, J.A. Mccorquodale, and L. Solari. Numerical study on the effect of the spur dikes on sedimentation pattern. *Ain Shams Engineering Journal* 9(4): (2018).
- 2 M. Pandey, Z. Ahmad, and P.K. Sharma. Scour around impermeable spur dikes: a review. *ISH Journal of Hydraulic Engineering* 24(1): 1-20 (2018).
- 3 M. Koken. Coherent structures around isolated spur dikes at various approach flow angles. *Journal of Hydraulic Research* 49(6): 736-743 (2011).
- 4 M.R. Kaffle. Numerical Simulation of Flow around a Spur Dike with Free Surface Flow in Fixed Flat Bed. *Journal of the Institute of Engineering* 9(1):

- 107-114 (2014).
- 5 H. Teraguchi, H. Nakagawa, K. Kawaike, Y. Baba, and H. Zhang. Effects of hydraulic structures on river morphological processes. *International Journal of Sediment Research* 26(3): 283-303 (2011).
 - 6 N. Anjum, and N. Tanaka. Hydrodynamics of longitudinally discontinuous, vertically double layered and partially covered rigid vegetation patches in open channel flow. *Journal of River Research Applications* 36(1): 1-13 (2019).
 - 7 S.-U. Choi, and H. Kang. Reynolds stress modeling of vegetated open-channel flows. *Journal of Hydraulic Research* 42(1): 3-11 (2004).
 - 8 U. Ghani, N. Anjum, G.A. Pasha, and M. Ahmad. Numerical investigation of the flow characteristics through discontinuous and layered vegetation patches of finite width in an open channel. *Journal of Environmental Fluid Mechanics* 19(6): 1469-1495 (2019).
 - 9 A. McCoy, G. Constantinescu, and L. Weber. Numerical Investigation of Flow Hydrodynamics in a Channel with a Series of Groynes. *Journal of Hydraulic Engineering* 134(2): 157-172 (2008).
 - 10 M. Vaghefi, B. Faraji, M. Akbari, and A. Eghbalzadeh. Numerical investigation of flow pattern around a T-shaped spur dike in the vicinity of attractive and repelling protective structures. *Journal of the Brazilian Society of Mechanical Sciences and Engineering* 40(2): (2018).
 - 11 H. Karami, A. Ardeshir, K. Behzadian, and M. Ghodsian. Protective spur dike for scour mitigation of existing spur dikes. *Journal of Hydraulic Research* 49(6): 809–813 (2011).
 - 12 J. Ning, G. Li, and S. Li. Numerical simulation of the influence of spur dikes spacing on local scour and flow. *Journal of Applied Sciences* 9(11): 2306 (2019).
 - 13 P. Esmaeli, S. Boudaghpour, M. Rostami, and M. Mirzaee. Experimental investigation of permeability and length of a series of spur dikes effects on the control of bank erosion in the meandering channel. *Ain Shams Engineering Journal* 13(4): 101701 (2022).
 - 14 K. Bora, and H.M. Kalita. Determination of best groyne combination for mitigating bank erosion. *Journal of Hydroinformatics* 21(5): 875–892 (2019).
 - 15 S. Nayyer, S. Farzin, H. Karami, and M. Rostami. A numerical and experimental investigation of the effects of combination of spur dikes in series on a flow field. *Journal of the Brazilian Society of Mechanical Sciences and Engineering* 41(6): 1-11 (2019).
 - 16 H. Shamloo, and B. Pirzadeh. Numerical Simulation of the Angle of Groyne Installation on the Separation Zone Length Behind it. *Journal of River Engineering* 2(5): 2014.
 - 17 H. Zhang, H. Nakagawa, K. Kawaike, and Y. baba. Experiment and simulation of turbulent flow in local scour around a spur dyke. *International Journal of Sediment Research* 24(1): 33-45 (2009).
 - 18 J. Yang, J. Zhang, Q. Zhang, X. Teng, W. Chen, and X. Li. Experimental research on the maximum backwater height in front of a permeable spur dike in the bend of a spillway chute. *Journal of Water Supply* 19(6): 1841-1850 (2019).
 - 19 M. Koken, and G. Constantinescu. An investigation of the dynamics of coherent structures in a turbulent channel flow with a vertical sidewall obstruction. *Journal of Physics of Fluids* 21: 085104 (2009).
 - 20 S. Maeno, S. Ogawa, and Y. Uema. Local scour analysis around a spur dike during a surge pass. *Journal of Hydraulic Engineering* 48(2): 817-822 (2004).
 - 21 N. Nagata, T. Hosoda, T. Nakato, and Y. Muramoto. Three-dimensional numerical model for flow and bed deformation around river hydraulic structures. *Journal of Hydraulic Engineering* 131(12): 1074-1087 (2005).



Catalogues of Some Useful Classes of Circular Designs in Blocks of Three Different Sizes to Control Neighbor Effects

Akbar Fardos, Abdul Salam, Jamshaid Ul Hassan, Hurria Ali,
Khadija Noreen, and Rashid Ahmed*

Department of Statistics, The Islamia University of Bahawalpur, Pakistan

Abstract: Minimal neighbor designs minimize the bias raised due to the neighbor effects using the minimum number of experimental units. Minimal circular balanced and strongly balanced neighbour designs can be constructed only for odd v (number of treatments to be compared). For v even, minimal Quasi Rees and nearly strongly balanced neighbor designs are constructed. In this article, the construction procedures of these four classes are described. Catalogues of these designs in blocks of three different sizes are also presented which provide the readymade solution to the experimenters and researchers.

Keywords: Neighbor Effects, CBNDs, CSBNDs, CQRNDs, CNSBNDs

1. INTRODUCTION

Minimal balanced neighbor designs (BNDs) and minimal strongly BNDs (SBNDs) are considered to be economical designs to control the neighbor effects. The bias raised due to neighbor effects can be minimized with the use of BNDs [1-4]. Following are some important definitions.

- If each treatment appears once as neighbor with all other treatments exactly once but does not appear as neighbor with itself, then the design is called minimal BND.
- If each treatment appears once as neighbor with all other treatments including itself exactly once, then the design is called minimal SBND. Method of cyclic shifts (Rule I) produces minimal circular BNDs (MCBNDs) and minimal circular SBNDs (MCSBNDs) for v odd.
- Design is called Quasi Rees neighbor design (QRND) if each treatment appears once as neighbor with other $(v-2)$ treatments exactly once and (i) appear twice with only one treatment, (ii) does not appear as neighbor with itself.
- Design is called minimal nearly SBND if each

treatment appears once as neighbor with other $(v-2)$ treatments exactly once and (i) appear twice with only one treatment, (ii) appear once as neighbor with itself except the treatment labeled as $(v-1)$ which does not appear as its own neighbor. Method of cyclic shifts (Rule II) produces circular QRNDs (CQRNDs) and minimal circular nearly SBNDs (MCNSBNDs) for v even.

Rees [5] introduced MCBNDs in serology for v odd. Misra *et al.* [6] introduced generalized neighbor designs (GNDs). Azais *et al.* [2] constructed some circular BNDs (CBNDs) using border plots. Preece [7] constructed CQRNDs for some cases. Chaure and Misra [8] constructed some classes of GNDs. Jaggi *et al.* [9] constructed some partially BNDs. Nutan [10] constructed some families of GNDs. Kedia and Misra [11] constructed some series of circular GNDs (CGNDs). Ahmed *et al.* [12] constructed economical CGNDs. Iqbal *et al.* [13] constructed some classes of CBNDs using cyclic shifts. Akhtar *et al.* [14] constructed CBNDs for block of size five. Meitei [15] constructed new series of (i) CNBDs and (ii) one-sided CBNDs. Ahmed and Akhtar [16] constructed CBNDs for block of size six. Shehzad *et al.* [17] constructed CBNDs for some cases.

Iqbal *et al.* [18] generated CGNDs for blocks of sizes three. Hamad and Hanif [19] developed two new procedures to construct non-directional two-dimensional BNDs and partially BNDs. Jaggi *et al.* [20] described some methods to construct CBNDs and circular partially BNDs to estimate direct and neighbor effects of the treatments in blocks of equal and unequal block sizes. Singh [21] developed new series of universally optimal one-sided CBNDs. Meitei [22] presented a new series of universally optimal one-sided CBND with block size 5. Salam et al. [23] introduced MCNSBNDs in equal and two different block sizes.

MCNSBNDs are important classes of neighbor designs to estimate the treatment effects and neighbor effects independently. Construction of these four important classes of neighbor designs will be an innovational work. In the present study, the construction procedures of these useful classes of neighbor designs are described. Catalogues of these designs in blocks of three different sizes are also presented for $v \leq 100$.

2. METHOD OF CYCLIC SHIFTS

Iqbal [24] introduced a method of cyclic shifts which is simplified here for the construction of minimal CBNDs, minimal CSBNDs, minimal CQRNDs and minimal CNSBNDs.

2.1. Construction of MCBNDs and MCSBNDs

In this section, method of cyclic shifts (Rule I) is explained for the construction of MCBNDs and MCSBNDs.

In this section, method of cyclic shifts (Rule I) is explained for the construction of MCBNDs and MCSBNDs.

Rule I: Let $S_j = [, \dots,]$ be i sets of shifts, $j = 1, 2, \dots, i, w = 1, 2, \dots, k_w - 1$.

- If $1 \leq v-1$ and S^* contains each of $1, 2, \dots, v-1$ exactly once, designs is MCBND.
- If $0 \leq v-1$ and S^* contains each of $0, 1, 2, \dots, v-1$ exactly once, designs is MCSBND.

Where S^* contains:

- i. Each element of sets S_j .
- Sum (mod v) of all elements in each set S_j .
- Complements of all elements in (i) & (ii), here complement of 'a' is ' $v-a$ '.

Example 2.1.1. $S_1 = [5,6,13,23], S_2 = [7,8,9], S_3 = [10,11]$ produce MCBND for $v = 25, k_1 = 5, k_2 = 4, k_3 = 3$.

Use $v (= 25)$ blocks for S_1 . Write $0, 1, \dots, v-1$ in first row. Complete 2nd row by adding 5 (mod 25) to the 1st row elements respectively. Similarly add 6, 13, 23 (mod 25). Use 25 more blocks for S_2

Table 1. MCBND generated from $S_1 = [5,6,13,23], S_2 = [7,8,9], S_3 = [10,11]$ for $v = 25$

Blocks																								
1	2	3	4	5	6	7	8	9	10	11	12	13	14	15	16	17	18	19	20	21	22	23	24	25
0	1	2	3	4	5	6	7	8	9	10	11	12	13	14	15	16	17	18	19	20	21	22	23	24
5	6	7	8	9	10	11	12	13	14	15	16	17	18	19	20	21	22	23	24	0	1	2	3	4
11	12	13	14	15	16	17	18	19	20	21	22	23	24	0	1	2	3	4	5	6	7	8	9	10
24	0	1	2	3	4	5	6	7	8	9	10	11	12	13	14	15	16	17	18	19	20	21	22	23
22	23	24	0	1	2	3	4	5	6	7	8	9	10	11	12	13	14	15	16	17	18	19	20	21
26	27	28	29	30	31	32	33	34	35	36	37	38	39	40	41	42	43	44	45	46	47	48	49	50
0	1	2	3	4	5	6	7	8	9	10	11	12	13	14	15	16	17	18	19	20	21	22	23	24
7	8	9	10	11	12	13	14	15	16	17	18	19	20	21	22	23	24	0	1	2	3	4	5	6
15	16	17	18	19	20	21	22	23	24	0	1	2	3	4	5	6	7	8	9	10	11	12	13	14
24	0	1	2	3	4	5	6	7	8	9	10	11	12	13	14	15	16	17	18	19	20	21	22	23
51	52	53	54	55	56	57	58	59	60	61	62	63	64	65	66	67	68	69	70	71	72	73	74	75
0	1	2	3	4	5	6	7	8	9	10	11	12	13	14	15	16	17	18	19	20	21	22	23	24
10	11	12	13	14	15	16	17	18	19	20	21	22	23	24	0	1	2	3	4	5	6	7	8	9
21	22	23	24	0	1	2	3	4	5	6	7	8	9	10	11	12	13	14	15	16	17	18	19	20

of every group is divisible by v . Then delete one (any) element from every group, the resultant will be $(i+2)$ sets to generate required designs.

Catalogue of MCBNDs in blocks of three different sizes for $v = 2ik_1 + 2k_2 + 2k_3 + 1$, $v \leq 60$, $5 \leq k_1 \leq 10$, $4 \leq k_2 \leq 7$, $3 \leq k_3 \leq 6$, where $k_3 < k_2 < k_1$.

v	k_1	k_2	k_3	Sets of Shifts
25	5	4	3	[5,6,13,23]+[7,8,9]+[10,11]
35	5	4	3	[2,6,8,18]+[12,13,14,28]+[9,10,11]+[15,16]
45	5	4	3	[5,9,10,18]+[6,7,8,22]+[13,15,19,31]+[11,16,17]+[20,21]
55	5	4	3	[3,14,16,20]+[7,9,10,23]+[8,12,13,17]+[18,19,27,31]+[11,21,22]+[25,26]
27	6	4	3	[3,6,8,13,22]+[7,9,10]+[11,12]
39	6	4	3	[4,5,7,8,12]+[9,10,15,16,22]+[11,13,14]+[18,19]
51	6	4	3	[3,5,7,12,22]+[8,9,17,21,41]+[14,15,16,18,26]+[11,19,20]+[23,24]
29	7	4	3	[3,5,6,8,14,20]+[7,10,11]+[12,13]
43	7	4	3	[6,7,14,17,18,21]+[5,9,10,12,13,35]+[11,15,16]+[19,20]
57	7	4	3	[5,6,7,13,27,53]+[10,12,14,20,24,25]+[15,16,17,18,19,21]+[11,22,23]+[26,29]
31	8	4	3	[4,5,6,7,9,12,16]+[8,10,11]+[13,17]
47	8	4	3	[5,6,8,9,16,20,26]+[7,11,12,13,14,15,19]+[10,17,18]+[22,24]
33	9	4	3	[5,6,7,8,10,13,16,31]+[9,11,12]+[14,15]
51	9	4	3	[5,6,7,8,9,16,22,26]+[12,13,14,15,17,18,21,41]+[11,19,20]+[23,24]
35	10	4	3	[3,5,6,8,9,12,14,18,28]+[10,11,13]+[15,16]
55	10	4	3	[3,5,6,7,8,9,12,27,31]+[13,14,15,16,17,18,19,20,23]+[11,21,22]+[25,26]
29	6	5	3	[5,6,11,14,20]+[3,7,8,10]+[12,13]
41	6	5	3	[11,12,16,17,21]+[7,8,10,13,38]+[2,9,14,15]+[18,19]
53	6	5	3	[5,6,7,9,23]+[12,16,21,22,27]+[13,14,15,18,36]+[2,11,19,20]+[24,25]
31	7	5	3	[5,6,7,11,12,17]+[3,8,9,10]+[13,16]
45	7	5	3	[6,7,13,18,19,22]+[8,9,10,12,17,31]+[2,11,15,16]+[20,21]
59	7	5	3	[2,3,5,6,13,29]+[8,9,10,14,22,48]+[15,16,17,18,19,21]+[23,24,25,26]+[27,28]
33	8	5	3	[6,7,9,12,13,16,31]+[3,8,10,11]+[14,15]
49	8	5	3	[2,5,6,7,10,21,46]+[9,11,12,13,14,15,16]+[18,19,20,24]+[22,23]
35	9	5	3	[5,6,8,10,13,14,18,28]+[2,9,11,12]+[15,16]
53	9	5	3	[5,6,7,8,9,18,23,27]+[12,13,14,15,16,21,22,36]+[2,11,19,20]+[24,25]
37	10	5	3	[2,3,5,6,7,8,9,14,19]+[11,13,15,25]+[16,17]
57	10	5	3	[3,5,6,7,8,9,10,12,53]+[13,14,15,16,17,18,19,21,27]+[22,23,24,25]+[26,29]
33	7	6	3	[3,5,6,7,13,31]+[9,10,11,12,16]+[14,15]
47	7	6	3	[3,4,5,6,7,20]+[10,11,12,13,14,26]+[15,16,17,18,19]+[22,24]
35	8	6	3	[6,9,12,13,14,18,28]+[2,3,8,10,11]+[15,16]
51	8	6	3	[3,5,6,8,15,22,41]+[9,11,12,13,14,16,26]+[17,18,19,20,21]+[23,24]
37	9	6	3	[3,5,6,7,8,9,15,19]+[10,11,13,14,25]+[16,17]
55	9	6	3	[3,6,7,8,9,17,27,31]+[10,11,12,13,14,15,16,18]+[19,20,21,22,23]+[25,26]
39	10	6	3	[3,4,5,6,7,8,9,13,22]+[11,12,14,15,16]+[18,19]
59	10	6	3	[5,6,7,8,9,10,16,26,29]+[12,13,14,15,17,18,19,20,48]+[21,22,23,24,25]+[27,28]
37	8	7	3	[3,5,6,7,8,19,25]+[9,10,11,13,14,15]+[16,17]
53	8	7	3	[2,3,5,6,7,8,21]+[10,11,12,13,14,15,22]+[18,19,20,23,27,36]+[24,25]
39	9	7	3	[4,5,6,7,8,9,14,22]+[10,11,12,13,15,16]+[18,19]

57	9	7	3	[6,7,9,10,11,15,24,27]+ [12,13,14,16,17,18,25,53]+[8,19,20,21,22,23]+[26,29]	41	9	7	4	[6,7,8,9,11,19,21,38]+[10,12,13,14,15,16]+ [5,17,18]
41	10	7	3	[5,6,7,8,9,10,17,21,38]+[11,12,13,14,15,16]+ [18,19]	59	9	7	4	[4,6,7,8,9,24,28,29]+[13,14,15,16,17,19,25,48]+[12,18,20,21,22,23]+[5,26,27]
31	6	5	4	[6,9,11,16,17]+[4,7,8,10]+[5,12,13]	43	10	7	4	[4,6,7,9,10,14,20,21,35]+[11,12,13,15,16,17]+ [5,18,19]
43	6	5	4	[9,14,16,20,21]+[7,11,12,17,35]+[3,10,13,15]+ [5,18,19]	37	7	6	5	[4,6,9,16,17,19]+[8,10,11,13,25]+[2,5,14,15]
55	6	5	4	[5,8,9,12,17]+[13,14,22,23,27]+ [15,16,18,20,31]+[6,7,19,21]+[3,25,26]	51	7	6	5	[6,7,12,23,24,26]+[8,9,11,13,17,41]+ [15,16,18,19,20]+[2,5,21,22]
33	7	5	4	[4,6,10,12,15,16]+[8,9,11,31]+[5,13,14]	39	8	6	5	[11,12,13,14,18,19,22]+[4,6,7,9,10]+[2,5,15,16]
47	7	5	4	[3,5,6,7,10,14]+[9,11,12,13,17,24]+ [16,18,19,26]+[4,20,22]	55	8	6	5	[5 , 6 , 7 , 9 , 2 2 , 2 7 , 3 1] + [1 0 , 1 1 , 1 2 , 1 3 , 1 4 , 1 6 , 2 6] + [17,18,19,20,21]+[2,4,23,25]
35	8	5	4	[3,4,6,8,13,16,18]+[10,11,12,28]+[5,14,15]	41	9	6	5	[6,7,8,9,14,18,19,38]+[11,12,13,15,21]+ [2,5,16,17]
51	8	5	4	[6,7,11,15,16,17,26]+[3,8,9,12,13,14,41]+ [19,20,21,24]+[5,22,23]	59	9	6	5	[4,6,7,8,9,24,28,29]+[12,14,15,16,17,18,27,48]+[19,20,21,22,23]+[2,5,25,26]
37	9	5	4	[3,4,6,7,8,9,10,25]+[13,14,17,19]+[5,15,16]	43	10	6	5	[4,6,7,9,10,16,19,20,35]+[12,13,14,15,21]+ [2,5,17,18]
55	9	5	4	[5,6,7,8,9,18,22,31]+[10,11,12,13,14,15,16,17]+[20,21,23,27]+[3,25,26]	41	8	7	5	[6,7,10,18,19,21,38]+[9,11,12,13,14,15]+ [2,5,16,17]
39	10	5	4	[3,5,6,7,8,9,10,13,15]+[12,14,19,22]+[4,16,18]	57	8	7	5	[6 , 7 , 9 , 1 1 , 2 2 , 2 7 , 2 9] + [1 0 , 1 2 , 1 3 , 1 4 , 1 5 , 1 6 , 2 6] + [18,19,20,21,23,53]+[2,5,24,25]
59	10	5	4	[4,6,7,8,9,10,17,25,29]+ [12,13,14,15,16,18,19,20,48]+[22,23,24,28]+[5,26,27]	43	9	7	5	[4,6,7,14,19,20,21,35]+[10,11,12,13,15,16]+ [2,5,17,18]
35	7	6	4	[3,4,6,9,18,28]+[10,11,12,13,16]+[5,14,15]	45	10	7	5	[4,7,8,9,10,20,21,22,31]+[11,12,13,15,16,17]+ [2,5,18,19]
49	7	6	4	[4,6,7,10,23,46]+[9,11,12,14,20,24]+ [15,16,17,18,19]+[5,21,22]	43	8	7	6	[3,4,5,6,10,21,35]+[9,11,12,13,14,20]+ [15,16,17,18,19]
37	8	6	4	[3,4,7,8,14,17,19]+[9,10,11,13,25]+[5,15,16]	59	8	7	6	[6,7,8,12,23,28,29]+[4,9,10,13,14,17,48]+ [16,18,19,20,21,22]+[15,24,25,26,27]
53	8	6	4	[4,6,7,12,22,25,27]+[9,10,13,14,15,16,21]+ [11,18,19,20,36]+[5,23,24]	45	9	7	6	[3,4,5,6,8,9,22,31]+[10,11,12,13,16,21]+ [15,17,18,19,20]
39	9	6	4	[3,5,6,7,8,10,15,22]+[11,12,13,14,19]+[4,16,18]	47	10	7	6	[3,4,5,6,7,8,13,22,24]+[11,12,14,15,16,17]+ [10,18,19,20,26]
57	9	6	4	[6,7,8,14,24,27,29,53]+ [10,11,12,13,15,16,17,18]+[19,20,21,22,23]+[5,25,26]					
41	10	6	4	[4,6,7,8,9,12,16,21,38]+[11,13,14,15,19]+ [5,17,18]					
39	8	7	4	[3,5,6,7,14,19,22]+[9,10,11,12,13,15]+[4,16,18]					
55	8	7	4	[4 , 5 , 7 , 1 2 , 2 2 , 2 7 , 3 1] + [1 0 , 1 1 , 1 2 , 1 3 , 1 4 , 1 5 , 1 6 , 2 3] + [9,17,18,19,20,21]+[3,25,26]					

4. CATALOGUE OF CQRNDS

CQRNDS can be constructed for $v = 2ik_1 + 2k_2 + 2k_3 - 2$; i integer, through method of cyclic shifts (Rule II) using i sets of shifts for k_1 , one each for k_2 and k_3 . These $(i+2)$ sets of shifts will be generated as:

- Consider $S = [1, 2, \dots, m-1, m]$, where $m = \frac{v-2}{2}$.
- Divide S into i groups of k_1 values and one

group of k_2 values such that the sum of every group is divisible by $v-1$. Then delete one (any) element from every group, the resultant will be $(i+1)$ sets.

Catalogue of CQRNDs in blocks of sizes three for $v = 2ik_1 + 2k_2 + 2k_3 - 2$, $v \leq 60$, $6 \leq k_1 \leq 10$, $5 \leq k_2 \leq 7$, $4 \leq k_3 \leq 6$, where $k_3 < k_2 < k_1$.

v	k_1	k_2	k_3	Sets of Shifts
28	6	5	4	[3,4,5,6,7]+[8,10,11,13]+[1,9]t
40	6	5	4	[4,5,6,9,12]+[2,7,8,10,11]+[14,16,17,18]+[15,19]t
52	6	5	4	[4,5,6,9,24]+[7,8,10,11,13]+[14,15,17,19,25]+ [20,21,22,23]+[1,18]t
30	7	5	4	[5,6,8,11,12,13]+[2,7,9,10]+[4,14]t
44	7	5	4	[3,4,5,6,10,13]+[8,9,11,12,19,20]+[16,17,18,21]+[1,15]t
58	7	5	4	[3,4,5,7,9,27]+[11,12,13,19,21,28]+ [14,15,16,17,18,26]+[22,23,24,25]+[1,6]t
32	8	5	4	[4,5,6,7,10,13,14]+[2,8,9,11]+[12,15]t
48	8	5	4	[2,3,5,6,7,8,15]+[9,10,11,12,13,14,21]+ [17,19,20,22]+[18,23]t
34	9	5	4	[4,5,6,7,8,9,10,15]+[12,13,14,16]+[1,3]t
52	9	5	4	[5,6,7,8,9,14,24,25]+[3,10,11,12,13,15,17,19]+ [20,21,22,23]+[1,18]t
36	10	5	4	[3,4,5,6,7,8,9,10,16]+[13,14,15,17]+[1,12]t
56	10	5	4	[2,3,4,5,6,7,8,9,10]+ [12,13,14,15,17,18,19,20,26]+ [22,23,24,25]+[21,27]t
32	7	6	4	[1,2,3,5,6,10]+[7,9,11,13,14]+[12,15]t
46	7	6	4	[1,2,4,7,8,20]+[9,11,12,13,14,21]+[5,16,17,18,19]+[6,22]t
60	7	6	4	[4,5,6,8,10,14]+[3,11,13,27,28,29]+ [9,16,17,19,20,22]+[2,23,24,25,26]+[1,21]t
34	8	6	4	[2,5,6,7,11,15,16]+[8,10,12,13,14]+[1,3]t
50	8	6	4	[2,4,6,10,22,23,24]+[9,11,12,13,14,15,16]+ [3,18,19,20,21]+[1,5]t
36	9	6	4	[2,4,5,7,8,9,13,16]+[3,11,14,15,17]+[1,12]t

54	9	6	4	[3,4,6,8,13,18,24,25]+[2,10,11,12,14,15,16,17]+[1,20,21,22,23]+[7,26]t
38	10	6	4	[1,2,4,6,7,8,10,16,17]+[9,12,13,14,15]+[5,18]t
58	10	6	4	[3,4,5,7,8,9,13,27,28]+ [11,14,15,16,17,18,19,23,26]+[2,21,22,24,25]+[1,6]t
36	8	7	4	[3,4,5,8,11,16,17]+[2,7,10,13,14,15]+[1,12]t
52	8	7	4	[4,5,6,7,22,23,24]+[8,9,13,14,15,16,17]+ [2,3,19,20,21,25]+[1,18]t
38	9	7	4	[2,3,4,7,8,11,16,17]+[1,10,12,13,14,15]+[5,18]t
56	9	7	4	[4,5,6,7,10,19,25,26]+[3,11,12,13,14,15,16,17]+[1,2,20,22,23,24]+[21,27]t
40	10	7	4	[2,3,4,6,7,8,9,16,18]+[1,10,12,13,14,17]+ [15,19]t
60	10	7	4	[4,5,6,7,8,9,12,28,29]+ [11,13,15,16,17,18,20,26,27]+ [2,3,22,23,24,25]+[1,21]t
48	7	6	5	[2,3,5,6,10,14]+[8,9,11,13,20,21]+[4,15,18,19,22]+[1,17,23]t
36	8	6	5	[4,5,6,8,9,15,16]+[3,11,13,14,17]+[1,2,10]t
52	8	6	5	[3,4,5,6,15,22,24]+[8,10,11,12,13,14,25]+ [7,17,19,20,21]+[1,2,16]t
38	9	6	5	[2,3,5,6,7,8,16,17]+[9,11,13,14,15]+[1,4,18]t
56	9	6	5	[4,5,6,7,8,10,25,26]+ [3,9,12,13,14,15,16,17]+ [2,21,22,23,24]+[1,20,27]t
40	10	6	5	[2,3,4,5,6,7,8,16,17]+[9,11,13,15,18]+[1,14,19]t
60	10	6	5	[4,5,6,7,8,9,10,27,28]+ [11,12,13,16,17,18,20,26,29]+[3,21,23,24,25]+[1,2,19]t
38	8	7	5	[3,5,6,7,8,16,17]+[2,9,10,13,14,15]+[1,4,18]t
54	8	7	5	[4,5,7,8,10,24,25]+[3,11,12,14,15,16,22]+ [2,9,17,19,20,21]+[1,6,26]t
40	9	7	5	[3,4,5,6,7,8,17,18]+[2,11,12,13,15,16]+ [1,14,19]t

58	9	7	5	[7,8,9,17,24,25,27,28]+ [5,10,12,13,14,15,16,18]+[3,6,19,21,22,23]+ [1,2,4]t
40	8	7	6	[4,5,6,7,8,16,17]+[3,9,10,13,14,18]+[1,2,12,19]t
56	8	7	6	[5 , 6 , 7 , 8 , 1 2 , 2 4 , 2 5] + [9 , 1 0 , 1 1 , 1 3 , 1 5 , 1 6 , 2 2] + [3,4,17,19,21,26]+[1,2,18,27]t
60	9	7	6	[5,6,8,9,10,18,25,26]+ [12,13,14,15,17,22,28,29]+[4,7,19,21,23,24]+ [1,2,3,16]t
44	10	7	6	[5,6,7,8,9,18,19,20,21]+[4,11,12,14,15,17]+ [1,2,3,10]t

27	7	4	3	[1,2,6,10,13,22]+[7,8,9]+[11,12]
41	7	4	3	[2,5,6,10,21,38]+[8,9,12,13,16,17]+ [11,14,15,]+[18,19]
55	7	4	3	[2,3,5,6,8,31]+[7,9,12,13,19,23]+ [10,14,15,16,17,18]+[11,21,22]+[4,25]
29	8	4	3	[2,3,5,6,8,14,20]+[1,7,10]+[4,12]
45	8	4	3	[3,5,12,15,16,17,22]+[2,6,8,9,10,11,13]+ [1,7,18]+[4,20]
31	9	4	3	[3,4,5,6,7,8,12,17]+[9,10,11]+[13,16]
49	9	4	3	[5,6,7,8,13,17,21,24]+ [2,9,10,12,14,15,16,20]+[11,18,19]+[22,23]
33	10	4	3	[3,5,6,8,9,10,11,16,31]+[7,12,13]+[14,15]
53	10	4	3	[2,3,5,6,8,14,20,21,27]+ [9,10,11,12,13,15,16,18,19]+[7,22,23]+ [4,24]
27	6	5	3	[1,2,3,8,13]+[6,7,9,10]+[11,12]
39	6	5	3	[1,4,5,7,22]+[11,12,14,15,16]+[3,6,8,9]+ [18,19]
51	6	5	3	[1,2,14,15,19]+[7,8,11,13,22]+ [12,17,18,20,26]+[3,5,6,16]+[23,24]
29	7	5	3	[1,2,3,5,7,11]+[6,8,10,14]+[4,12]
43	7	5	3	[1,2,5,9,11,15]+[3,6,7,10,12,13]+ [14,16,17,18]+[4,19]
57	7	5	3	[1,3,6,7,13,27]+[5,9,10,11,12,14]+ [8,15,16,17,18,19]+[22,23,24,25]+[2,26]
31	8	5	3	[4,5,6,7,11,12,17]+[3,8,9,10]+[2,13]
47	8	5	3	[2,3,4,5,6,7,20]+[8,9,10,11,12,13,14]+ [15,16,18,19]+[1,22]
33	9	5	3	[1,5,6,7,8,10,13,16]+[3,9,11,12]+ [4,14]
51	9	5	3	[2,5,6,7,8,11,22,41]+[1,3,9,12,13,14,15,16]+ [17,18,20,21]+[4,23]
35	10	5	3	[1,2,3,5,6,8,13,14,18]+[9,10,11,12]+[4,15]
55	10	5	3	[1 , 2 , 3 , 5 , 6 , 7 , 8 , 9 , 1 4] + [10,11,12,13,15,17,18,19,23]+ [16,20,21,22]+[4,25]
31	7	6	3	[2,3,4,5,6,16]+[7,8,9,10,12]+[1,13]
45	7	6	3	[1,2,3,6,11,22]+[7,8,9,10,12,13]+ [15,16,17,18,19]+[4,20]
59	7	6	3	[1,2,5,6,19,26]+[7,8,10,12,13,20]+ [9,14,15,16,17,18]+[21,22,23,24,25]+ [27,28]

5. CATALOGUE OF MCSBNDS

MCSBNDS can be constructed for $v = 2ik_1+2k_2+2k_3-1$; i integer, through method of cyclic shifts (Rule 1) using i sets of shifts for k_1 , one each for k_2 and k_3 . These $(i+2)$ sets of shifts are generated as:

- Consider $S = [0, 1, 2, \dots, m-1, m]$, where $m = \frac{v-1}{2}$.
- Replace one or two values with their complements to make the sum of resultant S divisible by v , here complement of 'a' is 'v-a'.
- Divide resultant S in i groups of k_1 values and one group each of size k_2 and k_3 such that the sum of every group is divisible of v . Then delete one (any) value from each group, the resultant will be $(i+2)$ sets to generate MCSBNDS in blocks of three different sizes.

Catalogue of MCSBNDS in blocks of sizes three for $v = 2ik_1+2k_2+2k_3-1$, $v \leq 60$, $5 \leq k_1 \leq 10$, $4 \leq k_2 \leq 7$, $3 \leq k_3 \leq 6$, where $k_3 < k_2 < k_1$.

v	k_1	k_2	k_3	Sets of Shifts
23	5	4	3	[2,3,7,11]+[5,6,8]+[1,9]
33	5	4	3	[6, 13,16,31]+[5,7,8,10]+[9,11,12]+[4,14]
43	5	4	3	[2,3,17,21]+[7,12,14,18]+[5,6,9,10]+ [11,15,16,]+[4,19]
53	5	4	3	[2,9,15,27]+[3,6,8,13]+[5,7,10,12]+ [14,16,18,22]+[1,11,20]+[4,24]
25	6	4	3	[3,5,6,13,23]+[7,8,9]+[4,10]
37	6	4	3	[2,3,5,8,19]+[6,9,10,11,13]+[7,14,15]+[4,16]
49	6	4	3	[2,8,10,11,18]+[5,6,9,13,19]+ [12,14,15,16,17]+[7,20,21]+[4,22]

35	9	6	3	[1,3,5,6,8,9,10,28]+[11,12,13,14,18]+[4,15]	59	10	6	4	[2,3,4,6,9,12,25,28,29]+[7,10,13,14,15,16,17,18,19]+[20,21,22,23,24]+[5,26,27]
53	9	6	3	[1,2,3,5,7,9,10,16]+[8,11,12,13,14,15,23,27]+[6,18,19,20,21]+[4,24]	35	7	6	5	[2,3,4,5,9,12]+[6,8,11,16,28]+[10,13,14,15]
29	6	5	4	[2,3,4,7,13]+[6,8,10,14]+[5,11,12]	49	7	6	5	[1,4,5,6,9,24]+[2,7,8,10,11,14]+[13,15,16,17,18]+[20,21,22,23]
41	6	5	4	[2,4,7,12,16]+[6,8,9,10,11]+[13,14,15,19]+[5,17,18]	37	8	6	5	[1,2,3,5,6,7,13]+[4,8,9,11,17]+[10,14,15,16]
53	6	5	4	[2,3,4,19,25]+[6,7,8,9,10]+[11,12,14,15,18]+[16,20,21,22]+[1,5,23]	53	8	6	5	[1,3,4,5,6,16,18]+[7,9,10,11,13,14,15]+[2,8,19,20,21]+[12,22,23,24]
31	7	5	4	[2,3,4,6,7,9]+[8,10,11,16]+[5,12,13]	39	9	6	5	[4,5,6,7,8,10,16,22]+[9,11,12,13,14]+[1,2,3,15]
45	7	5	4	[2,3,4,6,8,22]+[7,9,10,12,13,18]+[11,15,16,17]+[5,19,20]	57	9	6	5	[1,2,3,5,6,7,8,29,53]+[[0,9,10,11,13,15,16,17,23]+[14,18,19,20,21,22]+[12,24,25,26,27]
59	7	5	4	[2,3,4,7,14,29]+[6,8,9,10,12,25]+[13,15,16,17,18,19]+[21,22,23,24]+[5,26,27]	41	10	6	5	[1,2,4,5,6,7,8,11,38]+[9,10,13,14,15]+[12,16,17,18]
33	8	5	4	[3,4,6,10,12,15,16]+[7,8,9,11]+[5,13,14]	41	8	7	6	[1,2,4,5,6,7,16]+[8,9,11,12,13,14]+[10,17,18,19,21]
49	8	5	4	[2,4,6,7,10,23,46]+[8,9,11,12,13,14,15]+[18,19,20,24]+[5,21,22]	57	8	7	6	[2,5,6,7,12,29,53]+[8,9,10,13,14,15,22]+[16,17,18,19,20,21]+[11,24,25,26,27]
35	9	5	4	[0,2,3,4,6,8,13,16,18]+[9,10,11,12,28]+[1,5,14,15]	43	9	7	6	[2,3,4,5,6,10,21,35]+[7,9,12,13,14,15]+[11,17,18,19,20]
53	9	5	4	[0,2,3,4,7,8,21,25,36]+[6,9,10,11,12,13,14,15,16]+[18,19,20,22,27]+[1,5,23,24]	45	10	7	6	[1,2,3,4,5,6,7,8,9]+[13,15,16,17,21,22]+[10,11,12,18,19]
37	10	5	4	[2,4,6,7,8,9,10,11,17]+[3,13,14,19]+[1,5,15]					
57	10	5	4	[2,3,6,7,8,9,10,16,53]+[11,12,13,14,15,17,18,19,23]+[20,21,22,24]+[5,25,26]					
33	7	6	4	[3,4,6,7,15,31]+[8,9,10,11,12]+[5,13,14]					
47	7	6	4	[1,4,5,6,7,24]+[8,10,11,12,13,14]+[15,16,17,18,19]+[2,3,20]					
35	8	6	4	[2,3,4,6,9,18,28]+[8,10,11,12,13]+[1,5,14]					
51	8	6	4	[4,6,7,14,21,24,26]+[2,3,8,9,11,13,15]+[16,17,18,19,20]+[1,5,22]					
37	9	6	4	[2,3,4,7,8,14,17,19]+[6,9,10,11,13]+[1,5,15]					
55	9	6	4	[2,4,5,6,7,8,11,12]+[9,13,14,15,16,17,23,27]+[18,19,20,21,22]+[1,3,25]					
39	10	6	4	[2,3,5,6,7,8,10,15,22]+[11,12,13,14,19]+[4,16,18]					

6. CATALOGUE OF MCNSBND S

MCNSBNDs can be constructed for $v = 2ik_1 + 2k_2 + 2k_3 - 4$; i integer, through method of cyclic shifts (Rule II) using i sets of shifts for k_1 , one each for k_2 and k_3 . These $(i+2)$ sets of shifts are generated as:

- Consider $S = [0, 1, 2, \dots, m-1, m]$, where $m = \frac{v-2}{2}$.
- Divide S in i groups of k_1 values and one group of k_2 values such that the sum of each group is divisible by $v-1$. Then delete one (any) value from each group, the resultant will be $(i+1)$ sets. Consider the last group as $(i+2)^{\text{th}}$ set of shifts which will consist of remaining k_3-2 elements, and sum of these remaining elements should not be necessarily divisible of $v-1$. Hence required MCNSBNDs will be constructed in blocks of three different sizes using these $(i+2)$ sets.

Catalogue of MCNSBNDs in blocks of sizes three for $v = 2ik_1 + 2k_2 + 2k_3 - 4$, $v \leq 60$, $6 \leq k_1 \leq 10$, $5 \leq k_2 \leq 7$, $4 \leq k_3 \leq 6$, where $k_3 < k_2 < k_1$.

v	k_1	k_2	k_3	Sets of Shifts
26	6	5	4	[8,9,10,11,12]+[4,5,6,7]+[1,2]t
38	6	5	4	[3,4,5,7,16]+[9,10,14,15,18]+[1,6,13,17]+ [11,12]t
50	6	5	4	[2,3,6,15,23]+[7,8,9,10,11]+[13,14,17,18,24]+[19,20,21,22]+[1,25]t
28	7	5	4	[4,6,8,11,12,13]+[3,5,7,10]+[1,9]t
42	7	5	4	[2,3,5,6,7,18]+[9,10,11,12,13,19]+[15,16,17,20]+[1,4]t
56	7	5	4	[3,4,5,6,10,27]+[2,7,9,11,12,13]+[14,15,16,18,19,20]+[21,22,24,26]+[23,25]t
30	8	5	4	[3,5,6,8,11,12,13]+[2,7,9,10]+[4,14]t
46	8	5	4	[1,2,3,4,5,9,21]+[8,10,11,12,13,14,15]+ [17,18,19,20]+[6,22]t
32	9	5	4	[3,4,5,6,7,10,12,15]+[2,8,9,11]+[13,14]t
50	9	5	4	[3,4,7,8,11,18,23,24]+[6,9,10,12,13,14,15,17]+[19,20,21,22]+[1,5]t
34	10	5	4	[2,4,5,6,7,8,9,10,15]+[12,13,14,16]+[1,3]t
54	10	5	4	[1,2,3,4,5,6,8,9,15]+ [10,11,12,13,14,18,23,25,26]+[20,21,22,24]+[16,17]t
32	7	6	5	[5,8,10,12,13,14]+[3,4,6,7,9]+[1,11,15]t
46	7	6	5	[2,3,4,6,9,21]+[8,11,12,13,19,20]+[14,15,16,17,18]+[1,5,22]t
60	7	6	5	[2,4,5,7,14,27]+[8,9,12,26,28,29]+[15,16,17,18,19,20]+[21,22,23,24,25]+[1,10,11]t
34	8	6	5	[4,5,6,7,13,14,15]+[9,10,11,12,16]+[0,1,3]t
50	8	6	5	[5,6,7,11,22,23,24]+[9,10,12,13,14,15,21]+[16,17,18,19,20]+[1,2,3]t
36	9	6	5	[3,4,5,6,7,14,15,16]+[9,11,12,13,17]+[1,2,10]t
54	9	6	5	[3,4,7,8,13,22,24,25]+[9,10,11,12,14,15,16,17]+[18,19,20,21,23]+[1,6,26]t
38	10	6	5	[2,3,5,6,7,8,10,16,17]+[11,12,13,14,15]+ [1,4,18]t

58	10	6	5	[5,6,7,8,9,10,19,24,26]+[12,13,14,15,16,17,18,27,28]+[20,21,22,23,25]+[1,2,4]t
38	8	7	6	[4,5,6,10,15,16,18]+[8,9,11,12,13,14]+ [1,2,3,17]t
54	8	7	6	[3,4,6,20,23,24,26]+[10,11,12,13,14,15,22]+[8,16,17,18,19,21]+[1,2,5,25]t
40	9	7	6	[4,5,6,7,8,15,16,17]+[9,10,11,13,14,18]+ [1,2,12,19]t
58	9	7	6	[7,9,20,24,25,26,27,28]+ [10,11,12,13,14,15,16,17]+[8,18,19,21,22,23]+[0,1,2,4]t

7. SUMMARY AND CONCLUSION

Easy methods to generate four important classes of neighbor designs namely; MCBNDs, MCSBNDs, CQRNDs and MCNSBNDs are developed in this article for almost every case of v . The developed methods produce these designs in equal as well as in unequal block sizes. The proposed designs are useful to (i) estimate the treatment effect and neighbor effect independently, and (ii) minimize the bias due to neighbor effects. The presented catalogues are useful for the experimenters because these provide them the design of their own choice.

8. ACKNOWLEDGEMENTS

Authors are thankful to the reviewers for their valuable corrections and suggestions.

9. CONFLICT OF INTEREST

The authors declare no conflict of interest.

10. REFERENCES

1. J.M. Azais. Design of experiments for studying intergenotypic competition. *Journal of the Royal Statistical Society: Series B* 49: 334-345 (1987).
2. J.M. Azais, R.A. Bailey, and H. Monod. A catalogue of efficient neighbor designs with border plots. *Biometrics* 49(4): 1252- 1261 (1993).
3. J. Kunert. Randomization of neighbour balanced designs. *Biometrical Journal* 42(1): 111-118 (2000).
4. J.S. Tomar, S. Jaggi, and C. Varghese. On totally balanced block designs for competition

- effects. *Journal of Applied Statistics* 32(1): 87-97 (2005).
5. D.H. Rees. Some designs of use in serology. *Biometrics* 23: 779-791 (1967).
 6. B.L. Misra, Bhagwandas, and S.M. Nutan. Families of neighbor designs and their analysis *Communications in Statistics - Simulation and Computation* 20: 427-436 (1991).
 7. D.A. Preece. Balanced Ouchterlony neighbor designs. *Journal of Combinatorial Mathematics and Combinatorial Computing* 15: 197-219 (1994).
 8. N.K. Chaurse, and B.L. Misra. On construction of generalized neighbor design. *Sankhya Series B* 58: 245-253 (1996).
 9. S. Jaggi, V.K. Gupta, and J. Ashraf. On block designs partially balanced for neighbouring competition effects. *Journal of Indian Statistical Association* 44(1): 27-41 (2006).
 10. S.M. Nutan. Families of proper generalized neighbor designs. *Journal of Statistical Planning and Inference* 137: 1681-1686 (2007).
 11. R.G. Kedia, and B.L. Misra. On construction of generalized neighbor design of use in serology. *Statistics and Probability Letters* 18: 254-256 (2008).
 12. R. Ahmed, M. Akhtar, and M.H. Tahir. Economical generalized neighbor designs of use in Serology. *Computational Statistics and Data Analysis* 53: 4584-4589 (2009).
 13. I. Iqbal, M.H. Tahir, and S.S.A. Ghazali. Circular neighbor-balanced designs using cyclic shifts. *Science in China Series A: Mathematics* 52(10): 2243-2256 (2009).
 14. M. Akhtar, R. Ahmed, and F. Yasmin. A catalogue of nearest neighbor balanced- designs in circular blocks of size five. *Pakistan Journal of Statistics* 26(2): 397- 405 (2010).
 15. K.K.S. Meitei. Circular neighbour-balanced designs and one-sided circular neighbour-balanced designs. *Sankhyā: The Indian Journal of Statistics, Series B* 72: 175-188 (2010).
 16. R. Ahmed, and M. Akhtar. Designs balanced for neighbor effects in circular blocks of size six. *Journal of Statistical Planning and Inference* 141: 687-691 (2011).
 17. F. Shehzad, M. Zafaryab, and R. Ahmed. Minimal neighbor designs in circular blocks of unequal sizes. *Journal of Statistical Planning and Inference* 141: 3681-3685 (2011).
 18. I. Iqbal, M.H. Tahir, M.L. Aggarwal, A. Ali, and I. Ahmed. Generalized neighbor designs with block size 3. *Journal of Statistical Planning and Inference* 142: 626-632 (2012).
 19. N. Hamad, and M. Hanif. Non-directional two-dimensional neighbor designs. *Pakistan Journal of Statistics* 33(4): 269-276 (2017).
 20. S. Jaggi, D.K. Pateria, C. Varghese, E. Varghese, and A. Bhowmik. A note on circular neighbour balanced designs. *Communications in Statistics - Simulation and Computation* 47: 2896-2905 (2018).
 21. K.P. Singh. A neighbor balanced design and its optimal certainty contribution. *Bulletin of Pure and Applied Sciences Section - E - Mathematics & Statistics* 38E(2): 636-640 (2019).
 22. K.K.S. Meitei. Universally Optimal One-sided Circular Neighbour-balanced Designs with $k = 5$. *Calcutta Statistical Association Bulletin* 72(2): 84-88 (2020).
 23. A. Salam, R. Ahmed, M. Daniyal, and R.A. Berihan. Minimal circular nearly strongly-balanced neighbor designs when left and right neighbor effects are equal. *Journal of Statistical Application and Probability* 11(3): 883-891 (2021).
 24. I. Iqbal. Construction of experimental design using cyclic shifts. *Ph.D. Thesis, University of Kent at Canterbury, UK* (1991).



A Stable Version of the Modified Algorithm for Error Minimization in Combined Numerical Integration

Aijaz Bhatti, Owais Ali Rajput*, and Zubair Ahmed Kalhoro

Institution of Mathematics and Computer Science, University of Sindh, Jamshoro, Pakistan

Abstract: The present study derives a stable version of “A Modified Algorithm for Reduction of Error in Combined Numerical Integration”. It is discovered that the earlier proposed scheme “A Modified Algorithm for Error Reduction in Combined Numerical Integration” exhibits accuracy fluctuations when the number of slits, n , is increased ($n \geq 9$). Starting with the number of slits $n = 9$ and increasing the count of sub-intervals, the error increases spontaneously. This spontaneous spike in error is resolved by considering a better combination of quadrature rules. To this, the notable result of this study is the identification of an optimal choice for quadrature formulae that could minimize error fluctuations in combined numerical integration regardless the number of slits (n). With this revised choice, the error remains relatively stable and predictable even as the count of sub-intervals is increased.

Keywords: Numerical Integration, Weddle’s Rule, Boole’s Rule, Six-Point Rule, Simpson’s 1/3 Rule.

1. INTRODUCTION

Quadrature is a mathematical technique that involves the computation of definite integrals. It has a plethora of applications in areas of engineering, finance, physics and beyond. In addition to its use in numerical integration, quadrature also has applications in the differential equations’ solutions, such as in the finding solution to boundary value problems numerically. It is also used in Monte Carlo simulation, which is a statistical method for approximating the value of an integral by sampling from a probability distribution. Quadrature methods aim to approximate definite integrals with a desired accuracy. Throughout the past years, various quadrature rules and formulas have been devised to enhance the accuracy of this approximation.

Among the earliest quadrature rules is the trapezoidal rule, which involves estimating the area under a curve by summing the areas of trapezoids. Though it is simple, this method isn’t always accurate, especially for highly curved functions that have jagged peaks and valleys. To remedy this limitation, new quadrature rules and formulae were

created. The Newton-Cotes (NC) formula is one of the most commonly used quadrature formulae. This formula includes splitting the area under a curve into smaller subintervals and then using a polynomial to approximate the curve inside each subinterval. The obtained approximation is then utilised to calculate the integral. The accuracy of the NC formula depends on the degree of the polynomial and the number of subintervals used.

To approximate definite integrals, quadrature formulas are used frequently. Definite integrals that cannot be integrated analytically can be approximated by quadrature formulas [1]. Quadrature methods are an effective way of approximating integrals when the integrand’s discontinuous behaviour is in a bounded range rather than the closed-form [2]. Newton–Cotes quadrature formulae are based on equally spaced points (abscissas) [3]. In mathematics, numerical integration (NI) is among the most basic and significant practices. It has a wide range of uses, including engineering, mechanics and physics. The primary purpose is to have an alternative mechanism for estimating given definite integrals within finite

integration limits. Difficulties in NI can be traced back to Greek antiquity. They increased the number of sides of an inscribed polygon to calculate the area of a circle. With the development of calculus in the 17th century, new mathematics evolved, contributing to elementary rules in NI. Later, NI got more practical with the advent of computers, and at the day, we have numerous classical and modern algorithms providing speedy and more accurate results [4]. Many researchers and experts have already conducted substantial research on NI. A NI rule was proposed by Amanat [5], which is based on commonly used Quadrature methods like the Trapezoidal, Simpson's, and Weddle's rules. Natarajan *et al.* [6] explored the superconvergence of the NC rule for Cauchy principal value integrals while Liu *et al.* [7] compared various NI rules for approximating these integrals. A mid-point integration rule for nonlinear differential equations was proposed by Soomro *et al.* [8], and Shaikh *et al.* [9] proved the quadrature methods outperform polynomial collocation in solving second-kind Fredholm integral problems.

Bhatti *et al.* [10] presented a modified approach for error reduction in combined numerical integration (CNI) by combining lower-order rules for decreased error and enhanced accuracy. This method outperforms the original quadrature rules by two orders of magnitude. In a particular quadrature rule, the number of slits is a parameter for obtaining higher accuracy. It is supposed that number of slits give a better approximation of the integral than number of slits, where . The algorithm modified by Bhatti seems to work fine. However, the error in the approximation of the integral does not always follow a downward trend. It is observed that for number of slits, the error is sometimes higher than for number of slits, where , and this happens periodically. This is what we have tried to rectify in the present study.

2. METHODOLOGY USED FOR QUADRATURE RULES

2.1 The Newton-Cotes Formulae

The NC formulae represent a set of numerical integration techniques widely employed in approximating definite integrals of functions.

These techniques are based on the concept of approximating a curve by a series of straight line segments. These formulae offer a practical approach to solving integrals when an analytical solution is not easily attainable or simply doesn't exist. They are particularly useful for functions that are difficult to integrate analytically.

The family of NC formulae is a simple yet effective set of NI algorithms. Divide a function $f(x)$ across some interval $[a, b]$ into n equal pieces so that $f_n = f(x_n)$ and $h \approx \frac{b-a}{n}$. Then, identify polynomials that resemble the listed function and integrate them to get an idea of the area under the curve. It would be ok to use Lagrange's interpolation to pick the ideal polynomials. In this manner, the NC formulae or quadrature formulae are derived by Beyer [11].

NC formulas are considered open, or closed if the interval used is $[x_2, x_{n-1}]$ or $[x_1, x_n]$ respectively. When the function is specified explicitly rather than tabulated against the values of x , the optimal NI approach is known as Gaussian quadrature. This approach yields more accurate approximations (but is substantially more difficult to execute) by selecting the intervals to sample the function by Hildebrand [12].

Following are the most commonly used formula. The trapezoidal rule refers to the 2-point closed NC formula because it approximates the integral by placing trapezoid(s) with a base parallel to the x -axis and an inclined top (linking the endpoints of the interval). Let x_1 and $x_2 = x_1 + h$ be the first the other endpoint then the Lagrange interpolating polynomial through the points (x_1, f_1) and (x_2, f_2) is:

$$\begin{aligned} P_2(x) &= \frac{x - x_2}{x_1 - x_2} f_1 + \frac{x - x_1}{x_2 - x_1} f_2 \\ &= \frac{x - x_1 - h}{-h} f_1 + \frac{x - x_1}{h} f_2 \\ &= \frac{x}{h} (f_2 - f_1) + (f_1 + \frac{x_1}{h} f_1 - \frac{x_1}{h} f_2) \end{aligned}$$

Upon integration throughout the interval, which corresponds to the area of the trapezoid, the result is:

$$\begin{aligned}
 \int_{x_1}^{x_2} f(x) dx &= \int_{x_1}^{x_1+h} P_2(x) dx \\
 &= \frac{1}{2h} (f_2 - f_1) [x^2]_{x_1}^{x_2} \\
 &\quad + \left(f_1 + \frac{x_1}{h} f_1 - \frac{x_1}{h} f_2 \right) [x]_{x_1}^{x_2} \\
 &= \frac{1}{2h} (f_2 - f_1) (x_2 + x_1) (x_2 - x_1) \\
 &\quad + (x_2 - x_1) \left(f_1 + \frac{x_1}{h} f_1 - \frac{x_1}{h} f_2 \right) \\
 &= \frac{1}{2} (f_2 - f_1) (2x_1 + h) + f_1 h \\
 &\quad + x_1 (f_1 - f_2) \\
 &= x_1 (f_2 - f_1) + \frac{1}{2} h (f_2 - f_1) + h f_1 \\
 &\quad - x_1 (f_2 - f_1) \\
 &= \frac{1}{2} h (f_1 + f_2) \\
 &\quad - \frac{1}{12} h^3 f''(\zeta) \quad (1)
 \end{aligned}$$

which is the trapezoidal rule. The final term indicates the margin of error, which is limited by the fact that $x_1 \leq \zeta \leq x_2$ cannot exceed the maximum value of $f''(\zeta)$ within this range.

The rule with 3 points is known as the Simpson's rule.

$$\begin{aligned}
 \int_{x_1}^{x_4} f(x) dx \\
 &= \frac{3}{8} h (f_1 + 3f_2 + 3f_3 + f_4) \\
 &\quad - \frac{3}{80} h^5 f^{(4)}(\zeta) \quad (3)
 \end{aligned}$$

The Boole's rule is a closed 5-point rule.

$$\begin{aligned}
 \int_{x_1}^{x_5} f(x) dx &= \frac{2}{45} h (7f_1 + 32f_2 + 12f_3 + 32f_4 \\
 &\quad + 7f_5) \\
 &\quad - \frac{8}{945} h^7 f^{(6)}(\zeta) \quad (4)
 \end{aligned}$$

Higher order rules include the 6-point.

$$\begin{aligned}
 \int_{x_1}^{x_6} f(x) dx \\
 \text{T} &= \frac{5}{288} h (19f_1 + 75f_2 + 50f_3 + 50f_4 \\
 &\quad + 75f_5 + 19f_6) \\
 &\quad - \frac{275}{12096} h^7 f^{(6)}(\zeta) \quad (5)
 \end{aligned}$$

And the Weddle's rule

$$\begin{aligned}
 \int_{x_1}^{x_7} f(x) dx \\
 \text{H} &= \frac{h}{140} (41f_1 + 216f_2 + 27f_3 + 272f_4 \\
 &\quad + 27f_5 + 216f_6 + 41f_7) \\
 &\quad - \frac{9}{1400} h^9 f^{(8)}(\zeta) \quad (6)
 \end{aligned}$$

Generally, the n -point rule can be expressed analytically as:

$$\begin{aligned}
 \int_{x_1}^{x_n} f(x) dx \\
 &= h \sum_{i=1}^n H_{n,i} f_i \quad (7)
 \end{aligned}$$

Where,

$$\begin{aligned}
 H_{n,r+1} &= \frac{(-1)^{n-r}}{r!(n-r)!} \int_0^n t(t-1) \dots (t-r+1)(t \\
 &\quad - r-1) \dots (t \\
 &\quad - n) dt \quad (8)
 \end{aligned}$$

Note that,

$$\begin{aligned}
 \sum_{r=0}^n H_{n,r+1} \\
 &= n \quad (9)
 \end{aligned}$$

2.2 Single and Multiple Integration Rules

By dividing intervals into smaller parts and applying the technique to each segment, we can enhance the accuracy of the mentioned rules. These resulting equations are referred to as multiple or composite rules, Burden *et al.* [13].

The observed order of accuracy for the quadrature formulas is: Simpson's $\frac{3}{8}$ formula $>$ Simpson's $\frac{1}{3}$ formula $>$ Boole's formula $>$ Trapezoidal formula $>$ Weddle's formula by Amjad *et al.* [14].

2.3 Modified Algorithm for Combined Quadrature

The scheme by Amanat [5] uses the following method Trapezoidal, Simpsons $\frac{3}{8}$, Boole's and Weddle's rule interchangeably. The number of sub-intervals in the methods is suggested to be greater than or equal to 9. Out of the total number of subintervals, the first 6 subintervals are to be approximated using the Weddle's rule, then the Boole's rule is to be used to approximated as much intervals as possible, then the priority is for Simpson's $\frac{3}{8}$ rule and lastly for any single leftover subinterval we can use the trapezoidal rule.

Starting with the number of sub-intervals $n = 9$ and increasing the count of sub-intervals, the method works fine for $n = 9$ and 10 , but as we reach $n = 11$, the error increases spontaneously. The method regains its momentum at $n = 12, 13$ and 14 , but again a spontaneous increase in error occurs at $n = 15$. See Table 1.

This describes that the error starts to raise only where the trapezoidal rule comes into picture. This could be resolved if consider any better option instead of trapezoidal rule and redefine the distribution of sub-intervals for the hybrid.

2.4 A Stable Version of the Modified Algorithm for Combined Numerical Integration

The "Modified Algorithm for Error Reduction in Combined Numerical Integration" (SMA) exhibits accuracy fluctuations when the domain number of sub-intervals, n , is increased ($n \geq 9$). Starting with the number of sub-intervals $n = 9$ and increasing the count of sub-intervals, the method works fine for $n = 9$ and 10 , but the error increases spontaneously at $n = 11$. The algorithm regains momentum for $n = 12, 13$ and 14 , but a spontaneous increase in error occurs at $n = 15$. This fashion describes that the error starts to raise only where the trapezoidal rule comes into combination (due to its poor order of accuracy). This could be resolved if consider a better option instead of the trapezoidal rule and redefine the distribution of sub-intervals for the algorithm. To overcome the fore-highlighted issue the choice of rules for approximating rules is revised as follows.

It is meaningful to give priority to rules that comes with the highest order of accuracy, Thus, the priority is to be given to the Weddle's rule first, then comes the Six-point rule and lastly, the Simpson's rule. Interestingly, this makes the algorithm more robust, as it can now handle $n \geq 4$ of sub-intervals.

2.4.1 The Revised Algorithm

- i. Choose the number of sub-intervals $n \geq 4$ to divide the interval of integration.

Table 1. Error fashion in the algorithm proposed by Bhatti *et al.* [10] over different number of subintervals

Number of subintervals	Description of Hybrid	Error
9	6W + 3S	Descends
10	6W + 4B	Descends
11	6W + 4B + 1T	Spontaneous rise
12	6W + 4B + 2T	Rises
13	6W + 4B + 3S	Descends
14	6W + 8B	Descends
15	6W + 8B + 1T	Spontaneous rise
16	6W + 8B + 2T	Increase
17	6W + 8B + 3S	Descends
18	6W + 12B	Descends
19	6W + 12B + 1T	Spontaneous rise
20	6W + 12B + 2T	Rises
21	6W + 12B + 3S	Descends
⋮	⋮	⋮

T refers to trapezoidal rule, S to Simpsons $\frac{1}{3}$, B to Boole's and W to Weddle's rule

ii. Let $\mathbf{rem}(n, 6)$ be the remainder when n is divided by 6. The possibilities could be: $\mathbf{rem}(n, 6) = 5, 4, 3, 2, 1, 0$.

- If $\mathbf{rem}(n, 6) = 0$, no sub-intervals are left to be integrated.
- If $\mathbf{rem}(n, 6) = 5$, we use the Six-Point rule to approximate the 5-leftover sub-intervals.
- If $\mathbf{rem}(n, 6) = 2$, we use the Simpson's $\frac{1}{3}$ rule to approximate the 2-leftover sub-intervals.
- If $\mathbf{rem}(n, 6) = 4$, we use the composite Simpson's $\frac{1}{3}$ rule to approximate the 4-leftover sub-intervals.
- If $\mathbf{rem}(n, 6) = 3$, we reserve 6 sub-interval and approximate the rest $n - 6$ sub-intervals with Weddle's rule. This too gives $\mathbf{rem}(n - 6, 6) = 3$, but now with the 6 reserved sub-intervals, we have a total of 9 sub-intervals. These 9 sub-intervals can be sorted as $5 + 4$ and used with the Six-Point and composite Simpson's $\frac{1}{3}$ respectively.
- If $\mathbf{rem}(n, 6) = 1$, we again reserve 6 sub-interval. This gives $\mathbf{rem}(n - 6, 6) = 1$, and with the 6 reserved sub-intervals, we have a total of 7 sub-intervals. These 7 sub-intervals can be sorted as $5 + 2$ and used with the Six-Point and Simpson's $\frac{1}{3}$ respectively.

iii. Finally, Sum up the segmented integral approximation to get approximate value of given definite integral.

3. RESULTS AND DISCUSSION

Approximate solutions for the three aforementioned examples have been obtained by employing the

proposed stable version of the modified algorithm for combined numerical integration (SMA). The computed outcomes are then tested against those obtained through existing methods (EM), like Simpson's 1/3rd or Simpson's 3/8th, depending on the number of segments. Furthermore, we compare the results from the SMA with the previously available algorithm (PMA) by Amanat [5] and the refined version of the modified algorithm (MA) as proposed by Bhatti *et al.* [10].

To evaluate the integrals in the examples, numerical tests have been undertaken. These computations are carried out using MATLAB® R2018b, where the codes are written and executed. The outcomes of the these tests are presented in Tables 2, 3, and 4, depicting the results achieved in figure 1, 2 and 3. Through the computation of both absolute and percentage errors, a comparison of the results is established. Across all instances, the proposed SMA approach consistently showcases its robust stability when places against with EM, PMA, and MA methods.

Example 1.

$$\int_0^1 \sqrt{1-x^2} dx, \text{ see Table 2 and Figure 1.}$$

Example 2.

$$\int_1^2 x\sqrt{1+x} dx, \text{ see Table 3 and Figure 2.}$$

Example 3.

$$\int_0^1 xe^{x^2} dx, \text{ see Table 4 and Figure 3.}$$

Figures 1, 2, and 3 illustrate graphical representations of Tables 2, 3, and 4. On the graphs, the y -axis displays the percentile error when the given integral is computed by EM, PMA, MA, and SMA; while the x -axis displays the number of subintervals. Compared to other methods, the proposed approach SMA is observed to have better performance.

4. CONCLUSION

The introduced SMA method is an improved version of the rule proposed by Bhatti *et al.* [10], incorporating a better the selection of quadrature rule combinations. The research reveals that as the number of subintervals increases, the SMA exhibits significantly greater stability in comparison to the existing composite rules by Amanat [5] and

Table 2. Numerical results from example 1 - EM, PMA and MA in comparison to SMA

	n = 9	n = 10	n = 11
EM	0.774546345	0.776129582	0.777362076
Abs. Error	1.0851e-2	9.2685e-3	8.0360e-3
Per. Error	1.3816 %	1.1801 %	1.0231 %
PMA	0.776456493	0.781754678	0.778798642
Abs. Error	8.9416e-3	3.6434e-3	6.5995e-3
Per. Error	1.1384 %	0.4639 %	0.8402 %
MA	0.780204267	0.782199413	0.778824026
Abs. Error	5.1938e-3	3.1987e-3	6.5741e-3
Per. Error	0.6613 %	0.4072 %	0.8370 %
SMA	0.781128346	0.781754818	0.782341531
Abs. Error	4.2698e-3	3.6433e-3	3.0566e-3
Per. Error	0.5436 %	0.4638 %	0.3891 %

Table 3. Numerical results from example 2 - EM, PMA and MA in comparison to SMA

	n = 9	n = 10	n = 11
EM	2.394714891	2.394609023	2.394530692
Abs. Error	5.5721e-4	4.5134e-4	3.7301e-4
Per. Error	2.3273e-2 %	1.8852e-2 %	1.5580e-2 %
PMA	2.394213311	2.39415769	2.394188088
Abs. Error	5.5635e-5	1.4999e-8	3.0412e-5
Per. Error	2.3238e-3 %	6.3e-7 %	1.2703e-3 %
MA	2.394157718	2.394157674	2.39418808
Abs. Error	4.3000e-8	1.0000e-9	3.0404e-5
Per. Error	1.7960e-6 %	4.0000e-8 %	1.2699e-3 %
SMA	2.394157703	2.394157690	2.394157675
Abs. Error	2.7960e-08	1.5331e-08	1.2720e-10
Per. Error	1.1670e-6 %	6.4000e-8 %	5.3000e-9 %

Table 4. Numerical results from example 3 - EM, PMA and MA in comparison to SMA

	n = 9	n = 10	n = 11
EM	0.862664226	0.862179431	0.861788193
Abs. Error	3.5233e-3	3.0385e-3	2.6473e-3
Per. Error	4.1009e-1 %	3.5367e-1 %	3.0813e-1 %
PMA	0.860034834	0.859147486	0.859737179
Abs. Error	8.9392e-4	6.5720e-6	5.9627e-4
Per. Error	1.0405e-1 %	7.6495e-4 %	6.9402e-2 %
MA	0.859167420	0.859141382	0.859733843
Abs. Error	2.6505e-5	4.680e-7	5.9293e-4
Per. Error	3.0851e-3 %	5.4470e-5 %	6.9014e-2 %
SMA	0.859150653	0.859147358	0.859148341
Abs. Error	9.739e-6	6.4440e-6	7.4270e-6
Per. Error	1.1335e-3 %	7.5005e-4 %	8.6446e-4 %

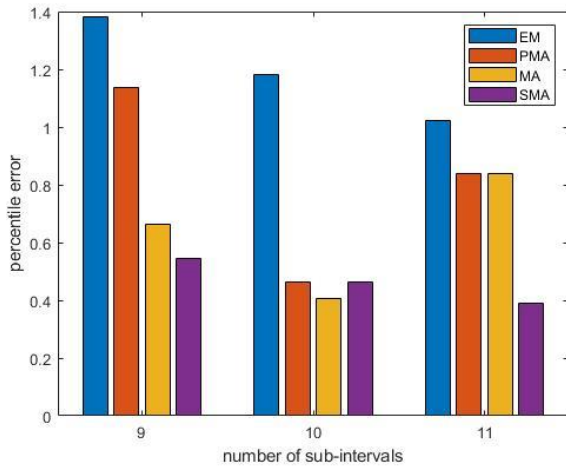


Fig. 1. Results from example 1

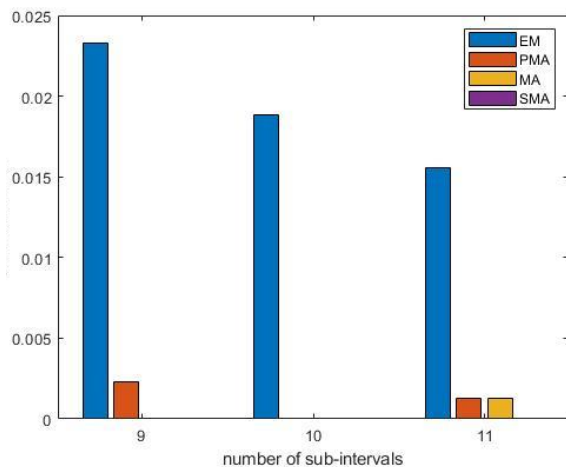


Fig. 2. Results from example 2

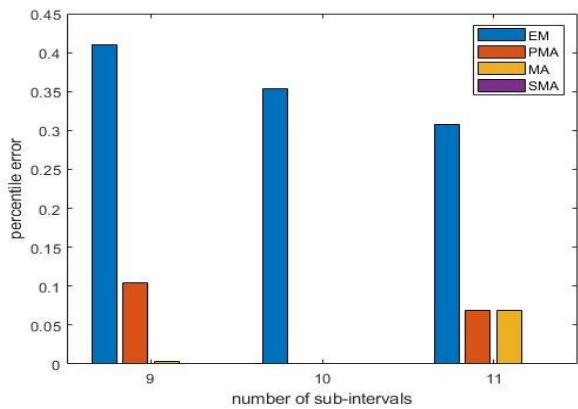


Fig. 3. Results from example 3

Bhatti et al. [10]. The findings demonstrate that the accuracy fluctuations encountered in previous methods are effectively mitigated through the redefined integration rule choices and their combined integration pattern implemented in SMA. This approach emerges as a preferable alternative to the previously employed rules, addressing accuracy concerns with enhanced stability.

5. CONFLICT OF INTEREST

The authors declare no conflict of interest.

6. REFERENCES

1. K.S. Gordon. Numerical integration. *Encyclopedia of Biostatistics* ISBN: 0471975761 (1998).
2. M.M. Shaikh, M.S. Chandio, and A.S. Soomro. A modified Four-point Closed Mid-point Derivative Based Quadrature Rule for Numerical Integration. *Sindh University Research Journal (Science Series)* 48(2): 389-392 (2016).
3. R.V. Dukkipati. Numerical methods. *New Age International Publisher* ISBN 10: 8122428134, ISBN 13: 9788122428131: 368 (2010).
4. A. Karpagam, and V. Vijayalakshmi. Comparison Results of Trapezoidal, Simpson's 1/3 rule, Simpson's 3/8 rule and Weddle's rule. *Asian Journal of Mathematical Sciences* 2(4): 50-53 (2018).
5. M. Amanat. Numerical Integration and a Proposed Rule. *American Journal of Engineering Research* 4: 120-123 (2015).
6. A. Natarajan, and N. Mohankumar. A comparison of some quadrature methods for approximating Cauchy principal value integrals. *Journal of Computational Physics* 116(2): 365-368 (1995).
7. D.J. Liu, J.M. Wu, and D.H. Yu. The Super Convergence Of The Newton-Cotes Rule For Cauchy Principal Value Integrals. *Journal of Computational and Applied Mathematics* 235(3): 696-707 (2010).
8. A.S. Soomro, G.A. Tularam, and M.M. Shaikh. A comparison of numerical methods for solving the unforced van der Pol's equation. *Mathematical Theory and Modeling* 3(2): 66-77 (2013).
9. M.M. Shaikh. Analysis of polynomial collocation and uniformly spaced quadrature methods for second kind linear Fredholm integral equations – a comparison. *Turkish Journal of Analysis and Number Theory* 7(4): 91-97 (2019).
10. A.A. Bhatti, M.S. Chandio, R.A. Memon, and M.M. Shaikh. A Modified Algorithm for Reduction of Error in Combined Numerical Integration. *Sindh University Research Journal (Science Series)* 51(4): 745-750 (2019).
11. W.H. Beyer. CRC Standard Mathematical Tables. 28th ed. *Boca Raton, FL: CRC Press*: pp 127 (1956).
12. F.B. Hildebrand. Introduction to Numerical Analysis. *McGraw-Hill Book. Company, Inc., New York* pp. 160-161 (1956).
13. R.L. Burden, and J.D. Faires. Numerical differentiation & integration numerical differentiation. *Numerical analysis* 174-184 (2011).
14. A. Amjad, F. Hamayun, and U. Muhammad. Simplified Numerical Analysis. *Pakistan: Time Render*, ISBN: 978-969-7821-01-3 (2018).



Quantum Computer Architecture: A Quantum Circuit-Based Approach Towards Quantum Neural Network

Tariq Mahmood*, Talab Hussain, and Maqsood Ahmed

Centre for High Energy Physics, University of the Punjab, Lahore, Pakistan

Abstract: According to recent research on the brain and cognition, the microtubule level activities in the brain are in accordance with the quantum mechanical concepts. Consciousness is the emergent phenomenon of the brain's subsystems and the quantum neural correlates. Based on the global work-space theory and traditional neural networks, investigations in machine consciousness and machine intelligence are reporting new techniques. In this study, a novel approach using circuit-based quantum neural network is proposed and simulated. This approach satisfies all the criteria of quantum computing and is tested for the exclusive OR (XOR) gate's nonlinear learning. As a result of the use of quantum gates, various quantum circuits, such as quantum adders and subtractors, are also created and included in the designing and simulation of circuit of the quantum neural networks. Moreover, it is also argued that the proposed circuit of quantum neural network may also be tested and implemented on real quantum computer hardware. The present study also stresses the applicability of techniques of machine learning algorithms such as quantum and classical neural networks to various challenges of High Energy Physics.

Keywords: High Energy Physics, Artificial Neural Network, Quantum Computing, Quantum Circuits, Quantum Neural Network.

1. INTRODUCTION

To recreate the characteristics of human intellect in computers, different theories of consciousness such as Global Workspace Theory [1–5] and Neural Correlate Theory have proposed different models in the recent years [6–18]. In machine intelligence, neurological correlates of consciousness are employed by artificial neural networks (ANNs) [18–21] which consist of layers (input, hidden and output) of neurons [21–23]. Real values are used as the ANNs' inputs, weights (connection strengths), and outputs [22, 23]. The artificial neural networks are being simulated to learn and recognize using the typically available computer architecture, which represents information with “0” or “1”. By claiming that information at the microtubule level in human brain follows the laws of quantum physics [9], Roger Penrose and Hameroff's Orch-OR model [13, 21] was used to describe the capabilities of the brain at the microtubule level. This model further contended that higher-level characteristics of the brain, such as consciousness and unconsciousness,

may be explained by general relativity and quantum physics principles [6-7, 13, 21]. Quantum physics may more effectively describe nature, including energy and matter at the microscopic level [24]. Quantum computing based upon its marvelous features such as superposition and entanglement is promising to provide answers to those higher dimensional issues that conventional computing has not yet been able to resolve [25]. The amazing properties of interference, entanglement, and superposition in quantum computing also offer a genuine parallel architecture [21, 24-27].

The typical concepts about Quantum Circuits, Quantum Neural Networks (QNNs) and Machine Learning in High-Energy Physics are as follows. As far as the Quantum Circuits are concerned, the quantum counterpart of classical information, known as a qubit, is denoted by the Dirac notations which are Ket (column) and Bra (row) vectors. Qubits may be a superposition of these states [24–25, 27] even if they are in the state of “ $|0\rangle$ ” or “ $|1\rangle$.” The arithmetic and logical units, registers,

and memory are only a few examples of the several classical gates utilized in classical computers. Quantum computing also consists of Hermitian matrices/operators named as single-qubit and multiqubit gates (H, X, Y, Z, CNOT, Toffoli, Fradklin etc.) to process information in quantum circuits required to build quantum computer architecture. The Toffoli gate, which can be seen in Figures 1, 2, and 3, is used to transform classical gates and circuits therefore named as the universal gate of quantum computing. As a result, Toffoli gate is used to form quantum circuits for the corresponding classical circuits (as seen in Figures 4, 5, 6, and 7).

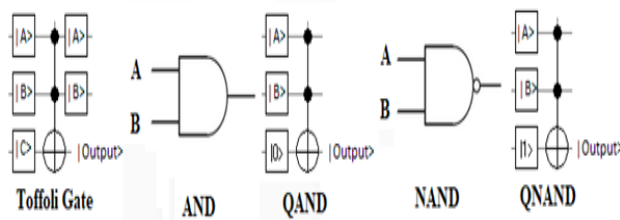


Fig. 1. By fixing the Toffoli gate’s third qubit to $|0\rangle$ or $|1\rangle$, the classical AND and NAND gates are transformed into Quantum AND and Quantum NAND gates respectively. Where inputs ($|A\rangle$, $|B\rangle$) and $|C\rangle$ are named as Qubits (quantum states) with A and B being classical bits (0 or 1) [28-30].

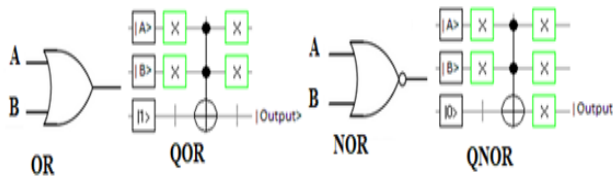


Fig. 2. By fixing third qubit of Toffoli gate to be $|1\rangle$ or $|0\rangle$, the classical OR and NOR gates are transformed into QOR and QNOR gates respectively. Where, inputs ($|A\rangle$, $|B\rangle$) and $|C\rangle$ are named as Qubits (quantum states) and A and B are classical bits (0 or 1) [28-30].

The Quantum Neural Networks (QNNs) are neural networks that use quantum mechanical concepts. Similar to artificial neuron, the quantum neurons are arranged in different layers of neuron such as input, hidden, and output. In contrast to conventional neural networks, quantum neural networks (QNNs) use complex column vectors for input and output, and complex Hermitian matrices or quantum operators for connection weights. Quantum neural networks are more effective than



Fig. 3. CNOT gate of quantum computing is equivalent of Classical XOR gate. Where, inputs ($|A\rangle$, $|B\rangle$) and $|C\rangle$ are named as Qubits (quantum states) and A and B are classical bits (0 or 1) [28-30].

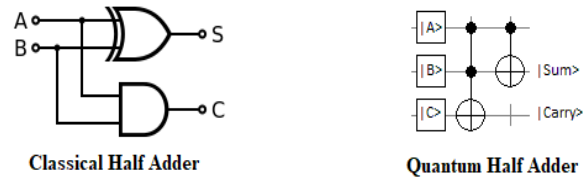


Fig. 4. Classical half adder is transformed into quantum half adder by applying Toffoli gate on the three qubits followed by CNOT gate applied to the first two qubits. Where, inputs ($|A\rangle$, $|B\rangle$) and $|C\rangle$ are named as Qubits (quantum states), and A, B, S (Sum), and C (Carry) are classical bits (0 or 1) [28-30].

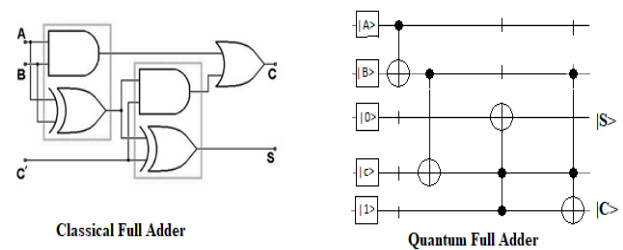


Fig. 5. Classical full adder is transformed into quantum full adder with CNOT gate and three Toffoli gates acting on different qubits. Where, inputs ($|A\rangle$, $|B\rangle$) and $|C\rangle$ are named as Qubits (quantum states) and A, B, S (Sum), and C (Carry) being classical bits (0 or 1) [28-30].

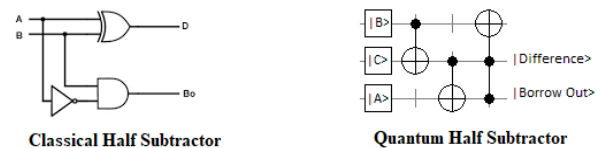


Fig. 6. Classical Half Subtractor is transformed into quantum Half Subtractor with two CNOT gates and one Toffoli gate acting on different qubits. Where, inputs ($|A\rangle$, $|B\rangle$) and $|C\rangle$ are named as Qubits (quantum states), A and B are classical bits (0 or 1), D (Difference) and B (borrowed) are classical outputs (0 or 1) [28-30].

conventional neural networks, as shown by earlier research in this field [22–23]. Li Fei [22] argued that one quantum neuron outperforms a network of six conventional neurons for the different input

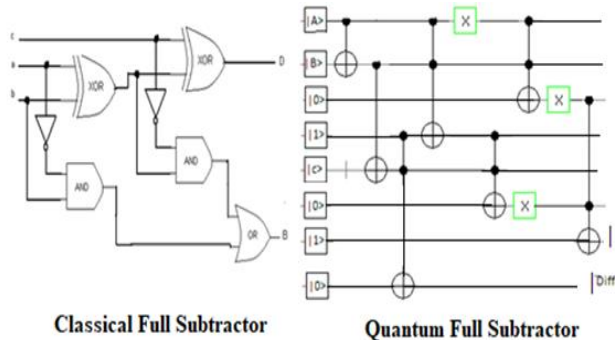


Fig. 7. Classical Half Subtractor is transformed into quantum Half Subtractor with three X gates, 6 Toffoli gates, and one CNOT gate acting on different qubits. Where, $|A\rangle$, $|B\rangle$ and $|C\rangle$, $|Difference\rangle$ and $|Borrow\rangle$ are Qubits (quantum states) and A, B, D (Difference) and B (Borrow) are classical bits (0 or 1) [28-30].

patterns of the XOR gate’s nonlinear learning. The concepts of Machine Learning in High-Energy Physics are also quite important. The high energy physicists (HEP) conduct experiments employing accelerator and detector technology as well as the Standard Model of particle physics to study the fundamental properties of the cosmos. Gravitational, strong, electromagnetic, and weak interactions are the basic forces that control how particles behave towards one another. The Standard Model, which was created in the 1970s, has proven very effective in describing physical processes involving basic interactions (apart from gravity), becoming the most thoroughly tested theory of physics, and accurately predicting the results in a broad range of events [31-33]. To optimize high-energy physics processes, several issues are being resolved using artificial neural networks [34-39]. Artificial neural networks are used in experimental high energy physics for classification of events [43-44], reconstruction of objects [45-46], triggering process [47-48], and track finding [49-50], while they are used in theoretical high energy physics to solve the Schrodinger wave equation and calculate the mass spectra of particles [40-42]. In addition, ordinary and partial differential equations of various domains [52-54] as well as quantum many-body problems are being resolved using artificial neural networks [51]. Quantum neural networks have also been emphasized recently by developments in high-energy physics and machine learning [55-58]. This research will be expanded in the future to address the issues in the aforementioned fields.

During the last ten years, a lot of research has been done on quantum neural networks [18-20, 22-23, 58-75]. Alexander’s research on “quantum neural networks” basically presents explanation of the paradigm of shifting from classical computing to quantum computing. There was also discussion of the advantages of quantum computing (using quantum neural networks) over conventional computing (using conventional neural networks) [23]. These advantages included high performance, Exponential memory, faster learning, processing speed, compact size, great stability, and reliability. By duplicating certain characteristics of the conventional neural network into a quantum counterpart, many algorithms have been developed for quantum neural networks, however, they are missing other qualities and limitations imposed by quantum computing.

QNNs are created by solely altering the input, output, and weights of artificial neural network into their quantum counterparts, by having overall architecture and methodology to be the same [19-20, 22-23, 57-58, 69-73]. However, Gradient Descent-based Algorithms are used for the majority of ANN implementation [22]. The present architecture of conventional and quantum neural networks is shown in Figure 8, and it has the following three shortcomings:

- (a) Cloning in Quantum Circuits: In conventional computers, it is simple to make a duplicate of the information, but according to the quantum theory of nature, because information is the

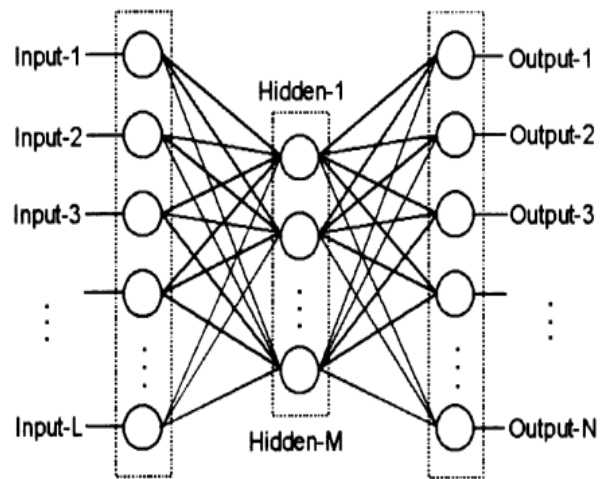


Fig. 8. Currently existing Classical or Quantum Neural Network Structure [30]

representational state of a physical system, like electrons or photons, it cannot be directly copied. In quantum computing, information may be copied from one location to another via the fan-out operator or circuit of teleportation [76]. Therefore, without teleportation or the use of the fan-out operator, it is not feasible to transmit copies of the quantum information to the other neurons.

- (b) Reversibility in Quantum Computing: In quantum computing, information is processed by using quantum gates which are Hermitian matrices which make quantum circuits and quantum processes to be reversible. Because classical weight signals are not Hermitian matrices, therefore, a straight modification from classical to quantum is irretrievable.
- (c) Loss of Information: In classical circuits, number of inputs varies from number outputs resulting into loss of information in the form of heat and direct conversion of classical neural network into quantum neural network in which inputs are qubits which represent of the physical system and this variation of input and output results into loss of information.

The main objectives of the present studies are as follows: (i) To highlight the drawbacks of the architecture of the existing conversion of classical neural networks to quantum neural networks, (ii) To address these drawbacks through a proposed quantum circuit-based approach and to simulate for the non-linear learning of XOR Gate, (iii) To process the proposed algorithm for each pattern of the truth table of the XOR Gate.

2. MATERIALS AND METHODS

The rules of quantum computing are not satisfied when a conventional neural network circuit or design is replicated into a quantum counterpart, therefore, it is essential to create a circuit or architecture for quantum neural networks that complies with all conceivable principles and computing/quantum mechanics limitations. Since traditional gates/circuits and neural networks have only one output and two input lines, respectively. Moreover, they are irreversible and lost their information as heat. However, one cannot claim that limitations exist in quantum computing, such as information loss, irreversibility, and the no-cloning theorem, since the number of input and output lines in quantum circuits is identical. The current research in quantum

neural networks continues in accordance with the classical hierarchy rather than the principles of quantum mechanics/computing. The present work argues that every transformation of the classical circuit into its quantum counterpart must satisfy all limitations or principle(s) of quantum computing. Therefore, it is argued that present practice of QNNs may not be used for the quantum mechanical way of implementation of higher-level feature of mind and brain into machines to accomplish intelligence. Because of the above-mentioned flaws, it is difficult to say that existing QNNs are capable of quantum learning. The presented quantum neuron has four inputs and four outputs, as shown in Figure 9. The connection weights are quantum operators with complex entities, whereas the inputs and outputs are complex column vectors.

The suggested quantum neurons (Figure. 9) may be used to build quantum neural networks

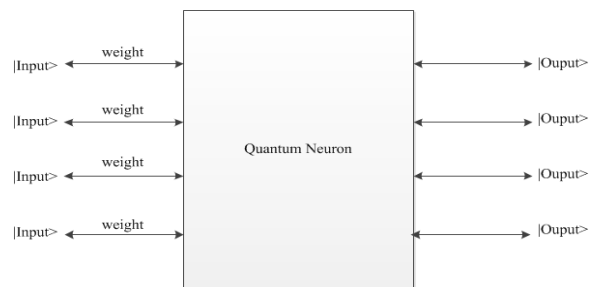


Fig. 9. Circuit Diagram of Quantum Neuron

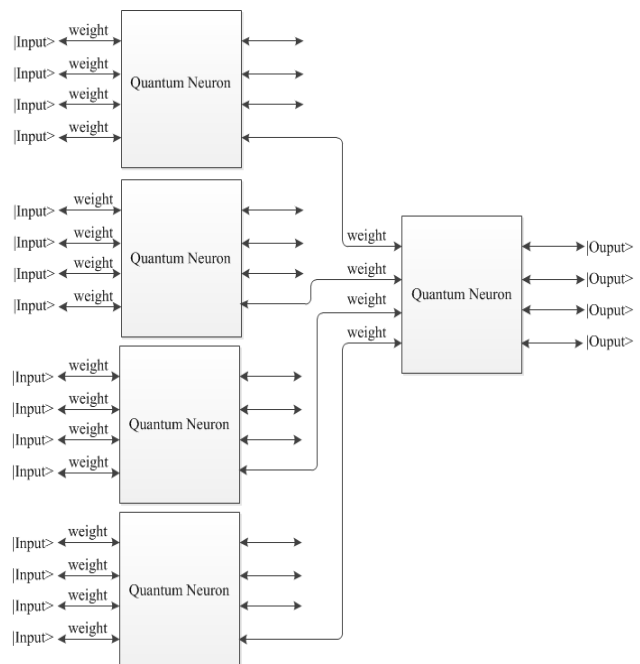


Fig. 10. Suggested model of Quantum Neural Network

(Figure. 10). The circuit lines that are not used by the next quantum neuron, may be passed on to other brain cells to accomplish additional functions. The suggested design prevents information loss by having an equal number of input and output lines, avoiding copying of quantum information, and having a reversible neural network. Quantum neuron layers may also be added to aid in the understanding of complicated events.

The suggested quantum neural network in this research complies with all restrictions and quantum computing principles. The identification and recovery of data about the suggested circuit/hierarchy of quantum neural networks is thus said to be beneficial for the employment of quantum learning, and it may also be advantageous to title it for the quantum-oriented involvement of the complicated processes in the brain and mind.

For quantum circuit-based simulation of the non-linear learning of XOR Gate, it is necessary to initially define the input and output patterns of the Quantum XOR gate. Table 1 shows the Truth table with the corresponding input and output patterns of the Quantum XOR gate.

Subsequently, the following quantum circuit-based algorithm/approach or steps are proposed for the simulation of non-linear learning of XOR Gate.

Step 1: Set up the quantum neuron's initial parameters, such as count=0, the connection weights as quantum operators, the learning rate (eta), the acceptable minimal error as E_{min} , and $\emptyset, \gamma, \delta$ and θ with random values for each various weight.

Table 1. Truth table with corresponding input and output patterns of Quantum XOR gate.

Input Pattern #	A)	B)	t)
1	0)	0)	0)
2	0)	1)	1)
3	1)	0)	1)
4	1)	1)	0)

Where $|0\rangle = \begin{bmatrix} 1 \\ 0 \end{bmatrix}$, $|1\rangle = \begin{bmatrix} 0 \\ 1 \end{bmatrix}$ and mixed or superposition state $|\Psi\rangle = \begin{bmatrix} a \\ b \end{bmatrix} = a|0\rangle + b|1\rangle$ (here a and b are probability amplitudes).

Step 2: Compute W_a and W_b by using undermentioned function for further calculation of corresponding output for different patterns of XOR gate.

$$W(\emptyset, \gamma, \delta, \theta) = e^{i\emptyset} \begin{pmatrix} \cos \delta e^{i\gamma} & \sin \delta e^{i\theta} \\ -\sin \delta e^{-i\theta} & \cos \delta e^{-i\gamma} \end{pmatrix}$$

$$|\text{Out}\rangle = W^* |\text{In}\rangle$$

$$\text{e.g. } |A_0\rangle = W_a^* |A\rangle, |B_0\rangle = W_b^* |B\rangle$$

Note: A tensor product of weights may be used to match the desired input order.

Step 3: Quantum neuron's final output is calculated by applying the quantum adder upon $|A_0\rangle$ and $|B_0\rangle$.

Step 4: Obtain a transfer function to use on the estimated $|\text{Out}\rangle$ that is comparable to the one mentioned by Li Fei [22]. The following is the transfer function:

$$FT = \frac{1}{\sqrt{2}} \begin{bmatrix} 0 & 1 \\ 1 & -1 \end{bmatrix} \begin{bmatrix} \sin(\bullet) & 0 \\ 0 & \sin(\bullet) \end{bmatrix}$$

Step 5: Use the transfer function: $|Y_0\rangle = FT^* |\text{Out}\rangle$ i.e

$$|Y_0\rangle = \frac{1}{\sqrt{2}} \begin{bmatrix} 0 & 1 \\ 1 & -1 \end{bmatrix} \begin{bmatrix} \sin(\bullet) & 0 \\ 0 & \sin(\bullet) \end{bmatrix} |\text{Out}\rangle$$

Here $|\text{Out}\rangle$ may be a mixed state:

$$|\text{Out}\rangle = \begin{bmatrix} \pm a \\ \pm b \end{bmatrix}$$

$$\begin{aligned} |Y_0\rangle &= \frac{1}{\sqrt{2}} \begin{bmatrix} 0 & 1 \\ 1 & -1 \end{bmatrix} \begin{bmatrix} \sin(\bullet) & 0 \\ 0 & \sin(\bullet) \end{bmatrix} \begin{bmatrix} \pm a \\ \pm b \end{bmatrix} \\ &= \frac{1}{\sqrt{2}} \begin{bmatrix} 0 & 1 \\ 1 & -1 \end{bmatrix} \begin{bmatrix} \sin(\pm a) \\ \sin(\pm b) \end{bmatrix} = \frac{1}{\sqrt{2}} \begin{bmatrix} 0 & 1 \\ 1 & -1 \end{bmatrix} \begin{bmatrix} +a \\ +b \end{bmatrix} \end{aligned}$$

$$|Y_0\rangle = \frac{1}{\sqrt{2}} \begin{bmatrix} b \\ a - b \end{bmatrix}$$

Step 6: Calculate error for the current patterns using $|\text{Er}\rangle = Q_{\text{Sub}}(|t\rangle, |Y_0\rangle)$

Step 7: Determine error by taking the inner product with itself error = $\langle \text{Er} | \text{Er} \rangle$

Step 8: compare this error with the E_{min} If error is less than E_{min} then increases the value of count++.

Step 9: If the patterns of XOR gate is fourth and the value of count equal to 4 then proceed to step 11 otherwise update the weight parameters in step 10 and then choose first pattern again as input/output, set the value of counter equal to 0 and goto step2.

Step 10: Update the following parameters.

$$\begin{aligned}\phi &= \phi + \eta \langle \text{In} | Q_{\text{Sub}}(|t\rangle, |Y_o\rangle) \\ \gamma &= \gamma + \eta \langle \text{In} | Q_{\text{Sub}}(|t\rangle, |Y_o\rangle) \\ \delta &= \delta + \eta \langle \text{In} | Q_{\text{Sub}}(|t\rangle, |Y_o\rangle) \\ \theta &= \theta + \eta \langle \text{In} | Q_{\text{Sub}}(|t\rangle, |Y_o\rangle)\end{aligned}$$

$\langle \text{In} | = \langle A |$ and $\langle \text{In} | = \langle B |$ for W_a and W_b respectively.

Step 11: Break

3. RESULTS AND DISCUSSIONS

The suggested approach is simulated using the Open Quantum Computing Framework (OpenQCF), which was created in Python and C#. It uses the QRegister ($|xxxx\rangle$), which is made up of various XOR Gate patterns, as the inputs and outputs (target output) to the quantum neuron. The Hermitian matrices are used as connection weights. Through the tensor product, many qubits are merged to create a QRegister, for example. $|AB\rangle = |A\rangle \otimes |B\rangle$

$$\text{Let } |A\rangle = |0\rangle = \begin{bmatrix} 1 \\ 0 \end{bmatrix} \text{ and } |B\rangle = |1\rangle = \begin{bmatrix} 0 \\ 1 \end{bmatrix}$$

$$|01\rangle = |0\rangle \otimes |1\rangle = \begin{bmatrix} 1 \\ 0 \end{bmatrix} \otimes \begin{bmatrix} 0 \\ 1 \end{bmatrix} = \begin{bmatrix} 0 \\ 1 \\ 0 \\ 0 \end{bmatrix}$$

Figures 11 and 12 show the mean squared error convergence rate with respect to number of iterations for minimum errors 0.000000005 and 0.000000005 corresponding to learning rates 0.035 and 0.0135, respectively.

From the truth table of XOR gate (Table 1) choose first pattern as input $|A\rangle = |0\rangle = \begin{bmatrix} 1 \\ 0 \end{bmatrix}$, $|B\rangle = |0\rangle = \begin{bmatrix} 1 \\ 0 \end{bmatrix}$. Initialize the W_a weight and corresponding output by using the following:

$$W(\phi, \gamma, \delta, \theta) = e^{i\phi} \begin{pmatrix} \cos \delta e^{i\gamma} & \sin \delta e^{i\theta} \\ -\sin \delta e^{-i\theta} & \cos \delta e^{-i\gamma} \end{pmatrix},$$

$$|Out\rangle = W^* |In\rangle$$

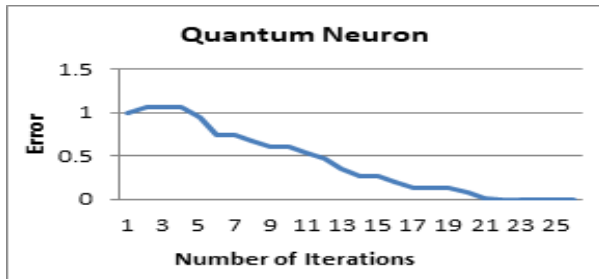


Fig. 11. Convergence of mean squared error of Quantum learning with learning rate=0.035 and MinError=0.000000005

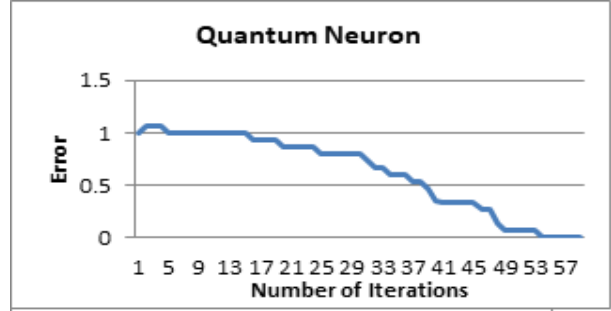


Fig. 12. Convergence of mean squared error of Quantum learning with learning rate=0.0135 and MinError=0.000000005

To explain the algorithm in simpler way, suppose following weight matrices are initiated based upon the random values of ϕ, γ, δ and θ .

$$W_a = \frac{1}{\sqrt{2}} \begin{bmatrix} 1 & 1 \\ 1 & -1 \end{bmatrix}, \quad W_b = \frac{1}{\sqrt{2}} \begin{bmatrix} 1 & 1 \\ 1 & -1 \end{bmatrix}$$

then

$$|A_o\rangle = W_a^* |A\rangle = \frac{1}{\sqrt{2}} \begin{bmatrix} 1 & 1 \\ 1 & -1 \end{bmatrix} \begin{bmatrix} 1 \\ 0 \end{bmatrix} = \frac{1}{\sqrt{2}} \begin{bmatrix} 1 \\ 1 \end{bmatrix} = \begin{bmatrix} \frac{1}{\sqrt{2}} \\ \frac{1}{\sqrt{2}} \end{bmatrix}$$

$$|B_o\rangle = W_b^* |B\rangle = \frac{1}{\sqrt{2}} \begin{bmatrix} 1 & 1 \\ 1 & -1 \end{bmatrix} \begin{bmatrix} 1 \\ 0 \end{bmatrix} = \frac{1}{\sqrt{2}} \begin{bmatrix} 1 \\ 1 \end{bmatrix} = \begin{bmatrix} \frac{1}{\sqrt{2}} \\ \frac{1}{\sqrt{2}} \end{bmatrix}$$

Quantum adder is applied on $|A_o\rangle$ and $|B_o\rangle$ to calculate the quantum neuron's final $|Out\rangle$.

$$|Out\rangle = QAdd(|A_o\rangle \text{ and } |B_o\rangle) = \begin{bmatrix} \sqrt{2} \\ \sqrt{2} \end{bmatrix} \text{ (assume QAdd provides this output)}$$

Apply the following transfer function upon the calculated $|Out\rangle$ which is considered by Li Fei [22].

$$FT = \frac{1}{\sqrt{2}} \begin{bmatrix} 0 & 1 \\ 1 & -1 \end{bmatrix} \begin{bmatrix} \sin(\bullet) & 0 \\ 0 & \sin(\bullet) \end{bmatrix}$$

Final output is calculated as $|Y_o\rangle = FT^* |Out\rangle$

$$|Y_o\rangle = \frac{1}{\sqrt{2}} \begin{bmatrix} 0 & 1 \\ 1 & -1 \end{bmatrix} \begin{bmatrix} \sin(\bullet) & 0 \\ 0 & \sin(\bullet) \end{bmatrix} |Out\rangle$$

Here we may get $|Out\rangle$ as a mixed quantum state

$$\begin{aligned} |Out\rangle &= \begin{bmatrix} \pm a \\ \pm b \end{bmatrix} \\ &= \frac{1}{\sqrt{2}} \begin{bmatrix} 0 & 1 \\ 1 & -1 \end{bmatrix} \begin{bmatrix} \sin(\bullet) & 0 \\ 0 & \sin(\bullet) \end{bmatrix} \begin{bmatrix} \sqrt{2} \\ \sqrt{2} \end{bmatrix} \\ &= \frac{1}{\sqrt{2}} \begin{bmatrix} 0 & 1 \\ 1 & -1 \end{bmatrix} \begin{bmatrix} \sin(\sqrt{2}) \\ \sin(\sqrt{2}) \end{bmatrix} = \frac{1}{\sqrt{2}} \begin{bmatrix} 0 & 1 \\ 1 & -1 \end{bmatrix} \begin{bmatrix} \sqrt{2} \\ \sqrt{2} \end{bmatrix} \end{aligned}$$

$$|Y_0\rangle = \frac{1}{\sqrt{2}} \begin{bmatrix} \sqrt{2} \\ 0 \end{bmatrix} = \begin{bmatrix} 1 \\ 0 \end{bmatrix} = |0\rangle$$

As $|t\rangle = |0\rangle$, $|Y_0\rangle = |0\rangle$ calculate

$$|Er\rangle = QSub(|t\rangle, |Y_0\rangle)$$

to Estimate error = $\|QSub(|t\rangle, |Y_0\rangle)\|^2 = 0$.

Based upon this error weights parameter will be updated by following formulas.

For W_a , $|In\rangle = |A\rangle = |0\rangle$

$$\phi = \phi + \eta \langle In | (QSub(|t\rangle, |Y_0\rangle)) \rangle$$

$$\phi = \phi + \eta \langle A | Er \rangle$$

$$\gamma = \gamma + \eta \langle In | (QSub(|t\rangle, |Y_0\rangle)) \rangle$$

$$\delta = \delta + \eta \langle In | (QSub(|t\rangle, |Y_0\rangle)) \rangle$$

$$\theta = \theta + \eta \langle In | (QSub(|t\rangle, |Y_0\rangle)) \rangle$$

$$W_a = W(\phi, \gamma, \delta, \theta) = e^{i\phi} \begin{pmatrix} \cos \delta e^{i\gamma} & \sin \delta e^{i\theta} \\ -\sin \delta e^{-i\theta} & \cos \delta e^{-i\gamma} \end{pmatrix}$$

For W_b , $|In\rangle$ is $|B\rangle = |0\rangle$ and the factors α, ψ, φ and χ will be revised to evaluate W_b consequently. For the current pattern weights will not be updated because error=0, therefore, XOR gate's second pattern will be processed which is $|A\rangle = |0\rangle = \begin{bmatrix} 1 \\ 0 \end{bmatrix}$, $|B\rangle = |1\rangle = \begin{bmatrix} 0 \\ 1 \end{bmatrix}$

$$W_a = \frac{1}{\sqrt{2}} \begin{bmatrix} 1 & 1 \\ 1 & -1 \end{bmatrix}, \quad W_b = \frac{1}{\sqrt{2}} \begin{bmatrix} 1 & 1 \\ 1 & -1 \end{bmatrix}, \text{ Then}$$

$$|A_0\rangle = W_a * |A\rangle = \frac{1}{\sqrt{2}} \begin{bmatrix} 1 & 1 \\ 1 & -1 \end{bmatrix} \begin{bmatrix} 1 \\ 0 \end{bmatrix} = \frac{1}{\sqrt{2}} \begin{bmatrix} 1 \\ 1 \end{bmatrix} = \begin{bmatrix} \frac{1}{\sqrt{2}} \\ \frac{1}{\sqrt{2}} \end{bmatrix}$$

$$|B_0\rangle = W_b * |B\rangle = \frac{1}{\sqrt{2}} \begin{bmatrix} 1 & 1 \\ 1 & -1 \end{bmatrix} \begin{bmatrix} 0 \\ 1 \end{bmatrix} = \frac{1}{\sqrt{2}} \begin{bmatrix} 1 \\ -1 \end{bmatrix} = \begin{bmatrix} \frac{1}{\sqrt{2}} \\ -\frac{1}{\sqrt{2}} \end{bmatrix}$$

Quantum adder is applied on $|A_0\rangle$ and $|B_0\rangle$ to calculate the quantum neuron's final $|Out\rangle$.

$$|Out\rangle = QAdd(|A_0\rangle \text{ and } |B_0\rangle) = \begin{bmatrix} \sqrt{2} \\ 0 \end{bmatrix}$$

(Assume QAdd provides this output)

Apply the following transfer function upon the calculated $|Out\rangle$ which is considered by Li Fei [22]

$$FT = \frac{1}{\sqrt{2}} \begin{bmatrix} 0 & 1 \\ 1 & -1 \end{bmatrix} \begin{bmatrix} \sin(\bullet) & 0 \\ 0 & \sin(\bullet) \end{bmatrix}$$

Final output is calculated as $|Y_0\rangle = FT * |Out\rangle$

$$|Y_0\rangle = \frac{1}{\sqrt{2}} \begin{bmatrix} 0 & 1 \\ 1 & -1 \end{bmatrix} \begin{bmatrix} \sin(\bullet) & 0 \\ 0 & \sin(\bullet) \end{bmatrix} |Out\rangle$$

Here we may get $|Out\rangle$ as a mixed quantum state

$$|Out\rangle = \begin{bmatrix} \pm a \\ \pm b \end{bmatrix}$$

$$\begin{aligned} |Y_0\rangle &= \frac{1}{\sqrt{2}} \begin{bmatrix} 0 & 1 \\ 1 & -1 \end{bmatrix} \begin{bmatrix} \sin(\bullet) & 0 \\ 0 & \sin(\bullet) \end{bmatrix} \begin{bmatrix} \sqrt{2} \\ 0 \end{bmatrix} \\ &= \frac{1}{\sqrt{2}} \begin{bmatrix} 0 & 1 \\ 1 & -1 \end{bmatrix} \begin{bmatrix} \sin(\sqrt{2}) \\ \sin(0) \end{bmatrix} = \frac{1}{\sqrt{2}} \begin{bmatrix} 0 & 1 \\ 1 & -1 \end{bmatrix} \begin{bmatrix} \sqrt{2} \\ 0 \end{bmatrix} \end{aligned}$$

$$|Y_0\rangle = \frac{1}{\sqrt{2}} \begin{bmatrix} 0 \\ \sqrt{2} \end{bmatrix} = \begin{bmatrix} 0 \\ 1 \end{bmatrix} = |1\rangle$$

As $|t\rangle = |1\rangle$, $|Y_0\rangle = |1\rangle$ calculate

$$|Er\rangle = QSub(|t\rangle, |Y_0\rangle)$$

to Estimate error = $\|QSub(|t\rangle, |Y_0\rangle)\|^2 = 0$.

For this pattern weights will not again be updated because error=0. In the same way, next input will be processed i.e. ($|B\rangle = |0\rangle = \begin{bmatrix} 1 \\ 0 \end{bmatrix}$, $|A\rangle = |1\rangle = \begin{bmatrix} 0 \\ 1 \end{bmatrix}$) and the fourth pattern ($|A\rangle = |1\rangle = \begin{bmatrix} 0 \\ 1 \end{bmatrix}$, $|B\rangle = |1\rangle = \begin{bmatrix} 0 \\ 1 \end{bmatrix}$) for XOR Gate. If four patterns yield no error, the processing will be stopped; if not, it will resume with first pattern of truth table by using updated weights and will continue until acceptable error is obtained.

There is no information loss or copying since the circuit for quantum neurons or neural networks has an equal number of input and output lines. Therefore, the suggested approach qualifies all limitations of quantum computing by considering the architecture's processing power, which is used to run the proposed algorithm's simulation. The findings and execution of the suggested method make it evident that the limitations discussed in this study are resolved. The suggested quantum neuron's corresponding circuit and algorithm satisfy all the fundamental laws and theorems of quantum computing. The simulation findings also demonstrate that it can learn many phenomena. Therefore, the proposed quantum circuit and algorithm is it is suggested, for the solution of Partial differential equations (PDEs) and Ordinary Differential Equations (ODEs), to implement quantum neural correlates of consciousness into machines, to calculate mass spectroscopy, and in high energy physics instead of using existing quantum or classical artificial neural networks. The related detail can be seen in author's PhD thesis [30] for further information.

A prominent work on the non-linear learning of XOR gate through quantum neural network is by Li Fei [22]. The algorithm used by Li Fei [22]

violates the quantum computing principles such as no-loss of information, reversibility, and no-cloning theorem etc. The algorithm explained in the present study is free of such drawbacks and ensures that principles of quantum computing are fully satisfied.

4. CONCLUSION

The present study proposes and implements a novel paradigm of quantum neural networks for the XOR gate's nonlinear learning. It is demonstrated that the proposed method follows all quantum computing constraints. Therefore, it is recommended to utilize the suggested QNNs circuit and corresponding algorithm for the modelling and employment of higher-level characteristics in conscious robots if the brain functions are in accordance with the principle of quantum mechanics. Additionally, the suggested quantum neural network and its associated circuits and algorithms may be employed to address certain high-energy physics issues.

5. CONFLICT OF INTEREST

Authors declare no conflict of interest.

6. DATA AND CODE AVAILABILITY

On reasonable request, the corresponding author will provide the code along with data sets created and used in the present work.

7. REFERENCES

1. B.J. Baars. A Cognitive Theory of Consciousness. *Cambridge, MA: Cambridge University Press* (1988).
2. B.J. Baars. The conscious access hypothesis: origins and recent evidence. *Trends in Cognitive Sciences* 6(1): 47-52 (2002).
3. R. Prakash, O. Prakash, S. Prakash, P. Abhishek, and S. Gandotra. Global workspace model of consciousness and its electromagnetic correlates. *Ann Indian Acad Neurol*:146-153 (2006).
4. B.J. Baars. Global workspace theory of consciousness: toward a cognitive neuroscience of human experience. *Progress in Brain Research* 150: 45-53 (2005).
5. B.J. Baars. The Global Workspace Theory of Consciousness. *The Blackwell Companion to Consciousness, Second Edition*, John Wiley & Sons Ltd: 227-242 (2017).
6. W.M. Qazi, K. Ahmed, Y. Saeed, A. Athar, and M. A. Saeed. Cybernetics Approach towards the Development of Cognitive Model for Machine. *International Conference on Intelligence and Information Technology* (2010).
7. W.M. Qazi, and K. Ahmad. Building Conscious Cybernetic Entities using QuBIC Model and Framework Based on Unified Theory of Mind. *The 11th Islamic Countries Conference on Statistical Sciences (ICCS-11), Lahore*, (2011).
8. I. Aleksander. Designing Conscious Systems, *Cogn Comput* 1: 22–28, (2009).
9. B.J. Baars, and S. Franklin. An Architectural Model of Conscious and Unconscious Brain Functions: Global Workspace Theory and IDA. *Neural Networks* 20: 955-961 (2007).
10. S. Frankin, and F. G. Patterson, The LIDA Architecture: Adding New Modes of Learning To An Intelligent, Autonomous, Software Agent. *Society for Design and Process Science, USA* (2006).
11. S. Franklin. Building life-like conscious software agents. *AI Communication* :183-193 (2000).
12. D. Gamez. The Development and Analysis of Conscious Machines. *University of ESSEX* (2008).
13. S.R. Hameroff. The Brain is Both Neurocomputer and Quantum Computer. *Cognitive Science* 31: 1035-1045 (2007).
14. Y. Kinouchi. A Logical Model of Consciousness on a Neural Network System with a Simple Abstract Brain-like Structure. *Nokia Workshop on Machine Consciousness* (2008).
15. J.A. Starzyk, and D.K. Prasad. A Computational Model of Machine Consciousness. *International Journal of Machine Consciousness* 3: 255-281 (2011).
16. R. Sun. The Importance of Cognitive Architectures: An Analysis Based on CLARION. *Journal of Experimental and Theoretical Artificial Intelligence* 19(2): 159-193 (2007).
17. R. Sun. Motivational Representations within a Computational Cognitive Architecture. *Cognitive Computation* 1: 91-103 (2009).
18. J.G. Taylor. CODAM: A Neural Network Model of Consciousness. *Neural Network* 20: 983-992 (2007).
19. K. Sgarbas. The Road to Quantum Artificial Intelligence. *11th Panhellenic Conference in Informatics* (2007).
20. B. Aoun, and M. Tarifi. Quantum Artificial Intelligence, *Quantum Information Processing, ArXiv:quant-ph/0401124* (2004).
21. W.M. Qazi. Modeling Cognitive Cybernetics From Unified Theory Of Mind Using Quantum Neuro-Computing For Machine Consciousness (2012).
22. L. Fei, D. Xiaoliang, Z. Shengmei, and Z. Baoyu. A Learning Algorithm for Quantum Neuron. *ISCP'04 Proceedings* (2004).
23. A. Ezhov, and D. Ventura. Quantum Neural Networks (2000).
24. M.A. Nielsen, and I.L. Chuang. Quantum Computation and Quantum Information. *Cambridge University Press* (2000).
25. D. Deutch. Quantum Theory, the Church–Turing

- principle and the universal quantum computer. *Proceedings of the Royal Society of London* 400: 97–117 (1985).
26. K. Raedit, K. Michielsen, H. Raedt, B. Trieu, G. Arnold, M. Richter, T. Lippert, H. Watanabe, and N. Ito. Massively Parallel Quantum Computer Simulator, *Computer Physics Communication* 176: 121-136 (2007).
 27. L.K. Grover. Quantum mechanics helps in searching for a needle in a haystack. *Physical Review Letters* 79: 325–328 (1997).
 28. R.C. Jaeger. Microelectronic Circuit Design. *McGraw-Hill*. 226–233. ISBN 0-07-032482-4 (1997).
 29. M.M. Mano, and M.D. Ciletti, Digital Design. *Pearson* (1927).
 30. T. Mahmood. Neural Network Based Study of Charmonium Spectrum. *PhD Thesis, submitted to Centre for High Energy Physics, University of the Punjab, Lahore-Pakistan* (2022).
 31. CERN, Physics at CERN, [Online]. Available: <https://home.cern/science/physics>. [Accessed 20 September 2019].
 32. A. Radovic, M. Williams, D. Rousseau, M. Kagan, D. Bonacorsi, A. Himmel, A. Aurisano, K. Terao, and T. Wongjirad. Machine learning at the energy and intensity frontiers of particle physics. *Nature* 560: 41-48 (2018).
 33. CERN, CERN accelerating science, [Online]. Available: <https://home.cern/science/physics/standard-model>. [Accessed 24 September 2019].
 34. B.H. Denby, Neural network and cellular automata in experimental high energy physics. *Computational physics communication* 49: 429-448 (1988).
 35. C. Peterson, T. Rognvaldsson, and L. Lonnblad. JETNET 3.0: a versatile artificial neural network package. *Computational Physics Communication* 81: 185-220 (1994).
 36. P. Baldi, K. Crammer, T. Faucett, P. Sadowski, and D. Whiteson. Parametrized neural networks for high energy physics. *European Physical Journal C* 76(05): (2016).
 37. G. Carleo, I. Cirac, K. Cranmer, L. Daudet, M. Schuld, N. Tishby, L. Vogt-Maranto, and L. Zdeborová. Machine learning and the physical sciences. *arXiv:1903.10563*, (2019).
 38. H. Mutuk. Energy levels of one-dimensional anharmonic oscillator via neural network. *Modern Physics Letters A* 34(12): 1950088 (2019).
 39. H. Mutuk. A Neural Network Study of Blasius Equation. *Neural Processing Letters* 51: 2179-2194 (2018).
 40. H. Mutuk. Cornell Potential: A Neural Network Approach. *Hindawi: Advances in High Energy Physics* 2019(3): 1-9 (2019).
 41. H. Mutuk. Neural Network Study of Hidden-Charm Pentaquark Resonances. *arXiv:1904.09756v3 [hep-ph]*, (2019).
 42. H. Mutuk. Mass Spectrum of Exotic X (5568) State via Artificial Neural Network. *arXiv:1901.01154* (2019).
 43. D. Collaboration. Classification of hadronic decays of Z0 into b and c quark pairs using neural network. *Physics Letters B* 295(3-4):383-395 (1992).
 44. H. Kolansoki. Application of artificial neural networks in particle physics. *Nuclear Instruments and Methods in Physics Research Section A: 14-20* (1995).
 45. A. collaboration, and I. Caprini. A neural network clustering algorithm for the ATLAS silicon pixel detector. *Journal of Instrumentation* 9(09): (2014).
 46. C. Peterson. Track finding with neural networks. *Nuclear Instruments and Methods in Physics Research Section A: 279(3): 537-545* (1989).
 47. L. Lonnblad, C. Peterson, and T. Rognvaldsson. Finding gluon jets with a neural trigger. *Physics Review Letters* 65: 1321-1324 (1990).
 48. H. Bruce, M. Denby, F. B. Campbell, N. Chriss, C. Bowers, and F. Nesti. Neural networks for triggering, *IEEE Transactions on Nuclear Science* 37(2): 248-254 (1990).
 49. R. Frhwirth, M. Regler, R. K. Bock, H. Grote, and D. Notz. Data analysis techniques for high energy physics. *Cambridge monographs* (1990).
 50. A. Strandlie, and R. Frhwirth. Track and vertex reconstruction: From classical to adaptive methods. *Review of Modern Physics* 82(2): (2010).
 51. G. Carleo, and M. Troyer. Solving the quantum many-body problem with artificial neural networks. *Science* 355(6325): 602-606 (2017).
 52. E.I. Lagaris, A. Likas, and D.I. Fotiadis. Artificial neural network for solving ordinary and partial differential equations. *IEEE transactions on neural networks* 9: 987-1000 (1998).
 53. D.W. Berry. High order quantum algorithm for solving linear differential equation. *Journal of Physics A: Mathematical and Theoretical* 47: (2014).
 54. Y. Cao, A. Papageorgiou, I. Petras, J. Traub, and S. Kais. Quantum algorithm and circuit design solving the poison equation. *New Journal of Physics* 15: 013021 (2013).
 55. K.K. Sharma. Quantum Machine Learning in High Energy Physics: the Future Prospects. *High Energy Particle Physics* 06: (2018).
 56. S. Carrazza. Machine learning challenges in theoretical HEP. *Journal of Physics Conference Series* 1085: (2017).
 57. A.J. Silva, T. B. Ludermir, and W. R. Oliveira. Quantum perceptron over a field and neural network architecture selection in a quantum computer. *Neural Networks* 76: (2016).
 58. F. Tacchino, C. Macchiavello, D. Gerace, and D. Bajon. An artificial neuron implemented on an actual quantum processor. *Nature partner journal: Quantum information* 5: 8 (2019).
 59. K.H. Wan, O. Dahlsten, H. Kristjánsson, R. Gardner, and M.S. Kim. Quantum generalization

- of feedforward neural networks. *npj Quantum Information* 3(1): (2017).
60. P. Rebentrost, T.R. Bromley, C. Weedbrook, and S. Lloyd. Quantum Hopfield neural network. *Physical Review A* 98: 042308 (2018).
 61. Y. Cao, G. G. Guerreschi, and A. Aspuru-Guzik. Quantum Neuron: an elementary building-block for machine learning on quantum computers. *arXiv:1711.11240* (2017).
 62. F. Neukart, and S.-A. Moraru. On Quantum Computers and Artificial Neural Networks. *Journal of Signal Processing Research* 2: 1-11 (2013).
 63. M. Schuld, I. Sinayskiy, and F. Petruccione. The quest for a Quantum Neural Net-work. *Quantum Information Processing* 13(11): 2567–2586 (2014).
 64. M. Schuld, I. Sinayskiy, and F. Petruccione. Simulating a perceptron on a quantum computer. *Physics Letters A* 379(7): 660–663 (2015).
 65. N. Wiebe, A. Kapoor and K. M. Svore. Quantum Perceptron Models. *Adv. Neural Inf.Process. Syst. (NIPS)* 29: 3999–4007 (2016).
 66. S. Lloyd, M. Mohseni, and P. Rebentrost. Quantum algorithms for supervised and unsupervised machine learning. *arXiv:1307.0411* (2013).
 67. L. Lamata. Basic protocols in quantum reinforcement learning with super-conducting circuits. *Scientific Reports* 7(1): 1609 (2017).
 68. J. S. Otterbach, R. Manenti, N. Alidoust, A. Bestwick, M. Block, B. Bloom, S. Caldwell, N. Didier, E. Schuyler Fried, S. Hong, P. Karalekas, C.B. Osborn, A. Papageorge, E.C. Peterson, G. Prawiroatmodjo, N. Rubin, C.A. Ryan, D. Scarabelli, M. Scheer, E.A. Sete, P. Sivarajah, Robert S. Smith, A. Staley, N. Tezak, W. J. Zeng, A. Hudson, Blake R. Johnson, M. Reagor, M. P. da Silva, and C. Rigetti. Unsupervised Machine Learning on a Hybrid Quantum Computer. *arXiv:1712.05771* (2017).
 69. M. Schuld, Xanadu, I. Sinayskiy, and F. Petruccione. Viewpoint: Neural Networks Take on Open Quantum Systems. *Physics* 12: (2019).
 70. A. Nagy, and V. Savona. Variational Quantum Monte Carlo Method with a Neural-Network Ansatz for Open Quantum Systems. *Physical Review Letters* 122(25): (2019).
 71. M.J. Hartmann, and G. Carleo. Neural-Network Approach to Dissipative Quantum Many-Body Dynamics. *Physical Review Letters* 122: 250502 (2019).
 72. F. Vicentini, A. Biella, N. Regnaul, and C. Ciuti. Variational Neural-Network Ansatz for the Steady States in Open Quantum Systems. *Physical Review Letters* 122: 250503 (2019).
 73. N. Yoshioka, and R. Hamazaki. Constructing neural stationary states for open quantum many-body systems. *Physical Review B* 99: 214306 (2019).
 74. C.P.D.S. Gonçalves. Quantum Neural Machine Learning: Theory and Experiments. *Applications in Medicine and Biology* (2019).
 75. B. Ricks, and D. Ventura. Training a Quantum Neural Network. *Advances in neural information processing systems* (2004).
 76. X.L. Wang, X.D. Cai, Z.E. Su, M.C. Chen, D. Wu, L. Li, N.L. Liu, C.Y. Lu, and J.W. Pan. Quantum teleportation of multiple degrees of freedom of a single photon. *Nature* 518(7540): 516-9 (2015).



Design and Development of Neutronics and Thermal Hydraulics Modeling Code for ACP1000 Nuclear Reactor Dynamics in Lab VIEW

Arshad Habib Malik^{1*}, Feroza Arshad², and Aftab Ahmad Memon³

¹Department of Basic Training, Chashma Centre of Nuclear Training, Pakistan Atomic Energy Commission, Chashma, Pakistan

²Department of Information System, Karachi Nuclear Power Generating Station, Pakistan Atomic Energy Commission, Karachi, Pakistan

³Department of Telecommunication Engineering, Mehran University of Engineering and Technology, Jamshoro, Pakistan

Abstract: An advanced neutronics and thermal hydraulics nuclear code, called GNTHACP code, is designed and developed in LabVIEW as Graphical Neutronics and Thermal Hydraulics toolkit for 1100 MWe Advanced Chinese PWR (ACP-1000) nuclear power plant. The reactor neutronics model is developed using a nonlinear point reactor kinetics model, while the reactor thermal hydraulics model is developed based on nonlinear fuel and coolant temperature dynamics. The heart of the GNTHACP code is the control rod reactivity model. Control rod reactivity banks are comprised of four power compensation banks G1, G2, N1, N2 and one temperature compensation bank R. The reactivity control configuration of these banks is highly nonlinear, complex and challenging in nature. The control rod reactivity model as a function of G1, G2, N1, N2 and R banks is optimized using two distinct techniques. The control rod reactivity model is optimized using Simplex Linear Programming (SLP) technique under constraints of reactor power as safety limit and control rod speed as maximum speed limit in LabVIEW. The control rod reactivity model is also optimized and investigated using nonlinear Sequential Quadratic Programming (SQP) technique under same constraints in LabVIEW. All the models are integrated and the state-of-the-art virtual instruments (VIs) are designed for cost function optimization, configuring models and calibration of model parameters in LabVIEW. The integrated model as graphical coupled neutronics and thermal hydraulics modeling code is optimized and validated against the Final Safety Analysis Report (FSAR) and different parameters of interest are investigated and proved within design limits as reported with CORCA and CORTH benchmark nuclear codes. The proposed code is stable, highly efficient and accurate as compared to other nuclear codes.

Keywords: Reactor Neutronics, Thermal Hydraulics, Linear Optimization, Nonlinear Optimization, ACP1000, Nuclear Power Plant.

1. INTRODUCTION

Nuclear reactor codes are designed, developed and used for industry-standard modeling of nuclear reactor cores for transient, safety and accident analyses. A reactor kinetics and dynamics model was developed in detail for the PWR type nuclear reactor by Johnson *et al.* [1], while the coupled transient neutronics calculations were performed for molten fast reactor by Laureau *et al.* [2]. An educational simulator for PWR neutronics was developed by Lam [3]. The educational tool was further extended for PWR neutronics with special

emphasis on transient and safety studies by Mollah *et al.* [4]. The reactor neutronics simulator is developed in LabVIEW by Hakim *et al.* [5]. The research is extended to thermal hydraulics studies of PWR by Ibrahim [6]. LabVIEW based Graphical User Interface (GUI) is developed for thermal hydraulics Reactor Excursion and Leak Analysis Program (RELAP) code for PWR by Macedo *et al.* [7]. A 3D neutron diffusion code is developed by Park *et al.* [8] for PWR neutron kinetics studies. A reactor dynamics code is developed for PWR studies for three different ratings of PWRs including ACP1000 using deep learning technique by Malik *et*

Received: July 2022; Accepted: June 2023

*Corresponding Author: Arshad Habib Malik <enr.dr.arshad.habib.malik@gmail.com>

al. [9]. Coupled neutronics and thermal hydraulics analysis is performed for nuclear reactor by Rais *et al.* [10]. Research is further extended for neutronics and thermal hydraulics sub-channel analysis of PWR by Ribeiro *et al.* [11] using Computational Fluid Dynamics (CFD) techniques. Point reactor kinetics model is optimized using Particle Swarm Optimization (PSO) technique by Mousakazemi [12]. PWR control rod drive mechanism is addressed with emphasis on 3D modeling and analysis by Tanaka [13]. Parameters of PWR steam cycle are optimized by simplex optimization technique by Wang *et al.* [14]. Sequential quadratic programming is used for large scale nonlinear problems by Boggs *et al.* [15]. Neutronics analysis is performed for research reactor with emphasis on safety parameters by Torabi *et al.* [16].

In the present research work, a third generation PWR nuclear reactor ACP1000 is addressed for design, modeling, analysis and simulation purposes. The techniques addressed above [13-16] are adopted for this research work. Accordingly, a novel state-of-the-art coupled neutronics and thermal hydraulics graphical code is developed with novel control rod reactivity optimal models using simplex linear programming and nonlinear sequential quadratic programming algorithms in LabVIEW for the first time for ACP1000 nuclear power plant. These new models based on SLP and SQP optimization techniques are more stable, efficient, faster and accurate as compared to other numerical techniques and Industry Standard Toolset (IST) nuclear codes such as CORCA and CORTH codes. SQP exhibits excellent stability and convergence for solving large-scale optimization problems. SQP can find high Net Present Value (NPV) after about few iterations. CORCA and CORTH codes are coupled through traditional master slave coupling. CORCA and CORTH codes do not incorporate the comprehensive modeling of control rods for advanced ACP1000 reactor dynamics. Average coolant temperature dynamics predicted by CORTH code is overestimated. Therefore, GNTHACP Code is a one step ahead towards nuclear code development as well as numerical optimization based toolkit development for ACP1000 reactor dynamics in LabVIEW. Various parameters used in the present research work are described as following:

n_r = Relative Reactor Power

ρ = Net Reactivity

$\rho_{INTERNAL}$ = Internal Reactivity

$\rho_{EXTERNAL}$ = External Reactivity

ρ_{FUEL} = Reactivity due to Fuel

$\rho_{MODERATOR}$ = Reactivity due to Moderator

ρ_{CR} = Reactivity due to Control Rods

β = Delayed Neutron Fraction

Λ = Average Neutron Life Time

λ = Decay Constant

C = Precursor Concentration

$G_{CR-BANK}$ = Worth of Control Rod Bank

M_F = Mass of Fuel

C_F = Specific Heat Capacity of Fuel

M_C = Mass of Coolant

C_{PC} = Specific Heat Capacity of Coolant at Constant Pressure

W = Flow Rate of Coolant

R = Thermal Resistance

T_F = Temperature of Fuel

T_C = Temperature of Coolant

T_{IN} = Temperature of Inlet

2. MATERIALS AND METHODS

2.1 ACP1000 Neutronics Modeling in CORCA Code

The CORCA Code is a two-group two-dimension fine-mesh static neutron diffusion and core burn-up calculation code. CORCA Code could be used in light water moderated PWRs. The code is capable to do calculations in both partial (1/8, 1/4, 1/2) and whole geometry. Baffle, thermal shield and reflector can be described in detail by the code. Replacement of assemblies' location is allowed in the code, which is frequently used in refueling calculations.

All the nuclear design parameters calculated, such as Neutron Effective Multiplication Factor (NEMF called K_{eff}), Moderator Temperature Coefficient (MTC), Total Peaking Factor (Fq) and Control rod worth, etc., are evaluated, and the accuracy of all the parameters is found the same as that of international comparable nuclear design codes, meeting the requirements of engineering design. The fuel temperature coefficient is calculated by performing two-group X-Y calculations using the CORCA Code. Moderator temperature is held constant and the power level is varied. Spatial variation of fuel temperature is taken into account by calculating the effective fuel temperature as a function of reactor power.

2.2 ACP1000 Thermal Hydraulics Modeling in CORTH Code

The objective of reactor core thermal design is to determine the maximum heat removal capability in all flow sub-channels and show that the core safety limits, as presented in the technical specifications are not exceeded while compounding engineering and nuclear effects. The thermal design considers local variations in dimensions, power generation, flow redistribution and mixing. The design is made using the CORTH computer code which is a three dimensional core sub-channels of variable size and form connected together. It determines in a very general way the steady state and transient flows of a fluid flowing in separate or connected channels. It is, thus, a suitable tool for the thermal-hydraulic analysis of reactor cores or experimental loops with heating rod bundles (limits of heat extraction from the core and in particular as it affects the critical heat flux). The CORTH Code gives all thermal-hydraulic variables in every node of the mesh: temperature of coolant, pressure, enthalpy, quality, void fraction, heat flux and flow-rate. It determines the margin with regard to the critical heat flux phenomenon.

2.3 Neutronics Modeling of ACP1000 Reactor Core

The neutronics modeling of ACP1000 reactor core is carried out using point reactor kinetics model with six precursor groups. The coupled relative neutron power and precursor concentrations are given as [1]:

$$\frac{dn_r(t)}{dt} = \frac{\rho(t) - \beta}{\Lambda} n_r(t) + \sum_{i=1}^6 \lambda_i C_i(t) \quad (1)$$

$$\frac{dC_i(t)}{dt} = \frac{\beta_i}{\Lambda} n_r(t) - \lambda_i C_i(t) \quad (2)$$

where the symbols having their usual meanings.

Six group precursors are chosen because these are representative groups in terms of half-lives of fission fragments and provides the sufficiently accurate neutron dynamics.

The net reactivity is given as:

$$\rho(t) = \rho_{INTERNAL}(t) + \rho_{EXTERNAL}(t) \quad (3)$$

Internal reactivity is given as:

$$\rho_{INTERNAL}(t) = \rho_{FUEL}(t) + \rho_{MODERATOR}(t) \quad (4)$$

where the symbols having their usual meanings.

Now, assuming the reactor is controlled with control rod banks. So, the external reactivity is given as:

$$\rho_{EXTERNAL}(t) = \rho_{CONTROLROD}(t) = \rho_{CR}(t) \quad (5)$$

where the symbols having their usual meanings.

2.4 Reactor Thermal Hydraulics Modeling of ACP1000 Reactor Core

The fuel temperature dynamics is given as [6]:

$$M_F C_F \frac{dT_F(t)}{dt} = n_r(t) - \frac{1}{R} [T_F(t) - T_C(t)] \quad (6)$$

The average reactor coolant temperature dynamics is given as:

$$M_C C_{PC} \frac{dT_C(t)}{dt} = \frac{1}{R} [T_F(t) - T_C(t)] - 2WC_{PC} [T_C(t) - T_{IN}(t)] \quad (7)$$

where the symbols having their usual meanings.

2.5 Control Rod Reactivity Modeling of ACP1000 Reactor Core

The control rod reactivity is given as [13]:

$$\frac{d\rho_{CR}(t)}{dt} = G_{CR-BANK} \frac{dx_{CR}(t)}{dt} = G_{CR-BANK} v_{CR}(t) \quad (8)$$

where $x_{CR}(t)$ and $v_{CR}(t)$ are the control rod bank position and control bank velocity respectively.

Amongst all models adopted in this research work, the control rod reactivity model is the most complex because it is comprised of four power compensation banks G1, G2, N1, N2 and one temperature compensation bank R which are configured in a highly nonlinear fashion.

2.6 Optimization of Control Rod Reactivity Model

The control rod reactivity model is optimized by the following two techniques:

- i) Simplex linear optimization technique
- ii) SQP nonlinear optimization technique

2.6.1 Simplex Linear Optimization Problem Formulation

Simplex linear optimization algorithm is used to optimize the control rod reactivity problem described in equation (8). This technique is the best choice with linear constraints which is the core advantage of this method [14].

$$\min f(v_{CR})$$

Subject to the linear constraints:

$$g(v_{CR}^j) \geq 0, \quad j = 1, 2, 3, 4$$

$$v_{CR}^1 \leq v_{CR}^2$$

$$v_{CR}^2 \leq v_{CR}^3$$

$$v_{CR}^3 \leq v_{CR}^4$$

$$v_{CR}^j \leq v_{CR}^{j, \max}$$

$$n_r \leq n_r^{SafetyLimit}$$

where v_{CR} is a j -dimensional variable vector, $f(v_{CR})$ is the objection function or cost function, $v_{CR}^{j, \max}$ is the upper bound of variable v_{CR}^j and $g(v_{CR}^j)$ is the j th inequality constraint of control rod reactivity optimization problem.

2.6.2. SQP Nonlinear Optimization Problem Formulation

SQP nonlinear optimization algorithm is used to optimize the control rod reactivity problem described in equation (8). SQP exhibits excellent stability and convergence for solving large-scale optimization problem of control rod reactivity comprising of several banks operating in complex configuration. This technique is the best with nonlinear constraints.

$$\min f(v_{CR}(t))$$

Subject to the nonlinear constraints:

$$g(v_{CR}^j(t)) \geq 0, \quad j = 1, 2, 3, 4$$

$$v_{CR}^1(t) \leq v_{CR}^2(t)$$

$$v_{CR}^2(t) \leq v_{CR}^3(t)$$

$$v_{CR}^3(t) \leq v_{CR}^4(t)$$

$$v_{CR}^j(t) \leq v_{CR}^{j, \max}$$

$$n_r(t) \leq n_r^{SafetyLimit}$$

where symbols having their usual meanings in nonlinear domain.

Now, the nonlinear control rod reactivity optimization problem is converted into QP sub-problem by means of gradient and nonlinear constraints. The solution space is obtained by series of QP sub-problems as [15]:

$$g(v_{CR}(t)) = \nabla f(v_{CR}(t))$$

$$\min \frac{1}{2} m^k T H^k m^k + g^T(v_{CR}(t)) m^k$$

where H^k the Hessain matrix of Lagrangian is function and m^k is the solution of SQ sub-problem.

Subject to the nonlinear constraints:

$$v_{CR}^1(t) + \nabla v_{CR}^1(t) m^k \leq v_{CR}^2(t) + \nabla v_{CR}^2(t) m^k$$

$$v_{CR}^2(t) + \nabla v_{CR}^2(t) m^k \leq v_{CR}^3(t) + \nabla v_{CR}^3(t) m^k$$

$$v_{CR}^3(t) + \nabla v_{CR}^3(t) m^k \leq v_{CR}^4(t) + \nabla v_{CR}^4(t) m^k$$

$$v_{CR}^j(t) + \nabla v_{CR}^j(t) m^k \leq v_{CR}^{j, \max} + \nabla v_{CR}^{j, \max}(t) m^k$$

$$n_r(t) + \nabla n_r(t) m^k \leq n_r^{SafetyLimit} + \nabla n_r^{SafetyLimit}(t) m^k$$

2.7 Framework of Neutronics and Thermal Hydraulics Modeling Code of ACP1000 Nuclear Reactor

The overall framework of neutronics and thermal hydraulics model consists of point reactor kinetics model, thermal hydraulics model of fuel and coolant and control reactivity model with both linear and nonlinear optimization techniques. The framework of ACP1000 neutronics and thermal hydraulics modeling is shown in Figure 1. All the models are coupled dynamic in nature solved and computed in parallel computing framework. LabVIEW is selected as programming platform because it is the best choice for nuclear code as stand-alone product development with powerful excellent user friendly GUI. However, initially, the coupled integrated model is first analyzed with simplex linear programming (SLP) and then with sequential quadratic programming (SQP).

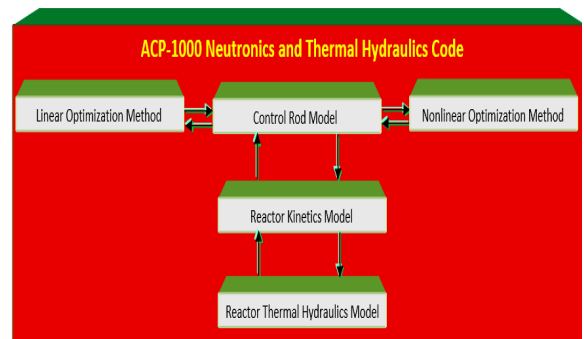


Fig. 1. Framework of ACP1000 neutronics and thermal hydraulics modeling.

3. RESULTS AND DISCUSSION

In the present investigations, the entire modeling and linear as well as non-linear optimization work is carried out in LabVIEW. Results are discussed in the following sections:

3.1 Modeling and Linear Optimization in LabVIEW

In the present research work, a virtual instrument (VI) is designed for linear simplex optimization as shown in Figure 2. The design of linear model optimization VI for control rod reactivity is shown in Figure 3. The linear constrained optimization problem is solved and various parameters of interest are analyzed. The initial value of control rod position is $x_0 = 357.1875$ cm. The control rod speeds are returned with four set of speeds as shown in Figure 4.

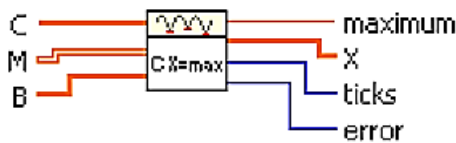


Fig. 2. Design of linear simplex optimization VI in LabVIEW

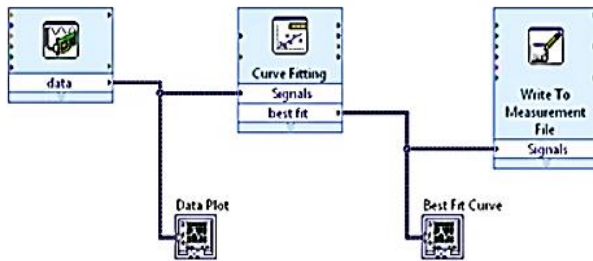


Fig. 3. Design of linear model optimization VI in LabVIEW

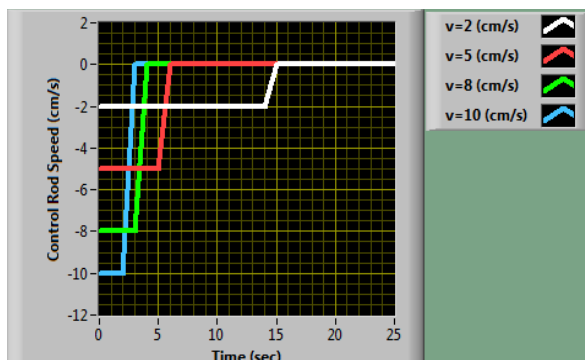


Fig. 4. Optimization of control rod speed with linear control rod reactivity model in LabVIEW

Amongst four design values of control rod speed, the desired objective is to obtain a maximum speed for safe operation of ACP1000 nuclear reactor. Therefore, the maximum safe control rod speed (MSCRS) is 2 cm/ sec which moves with optimal design time delay of 14 seconds. Now, it is desired that against maximum safe speed, the reciprocal of reactor period which is a measure of net reactivity under critical operation of the reactor must be zero as shown in Figure 5. This proves that reactor is self-regulating with internal and external reactivity feedbacks.

The behavior of maximum relative reactor power (MRRP) against four different control rod speed is shown in Figure 6. The maximum power level using ex-core instrumentation for large power excursion is 110% RP having equivalent relative reactor power of 1.1 on normalized or per unit scale. This value is basically the design safety limit before the actuation of protection system. The

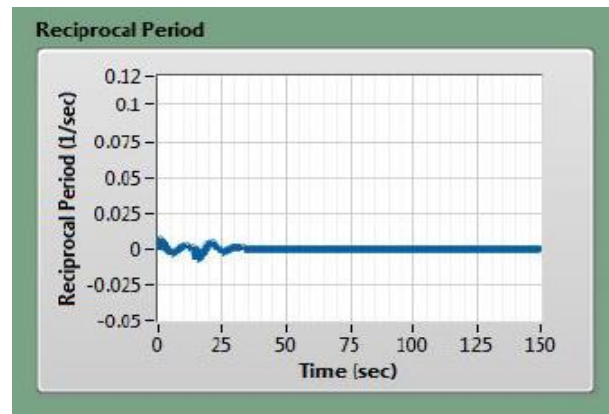


Fig. 5. Optimization of reciprocal reactor period at optimal control rod speed with linear control rod reactivity model in LabVIEW

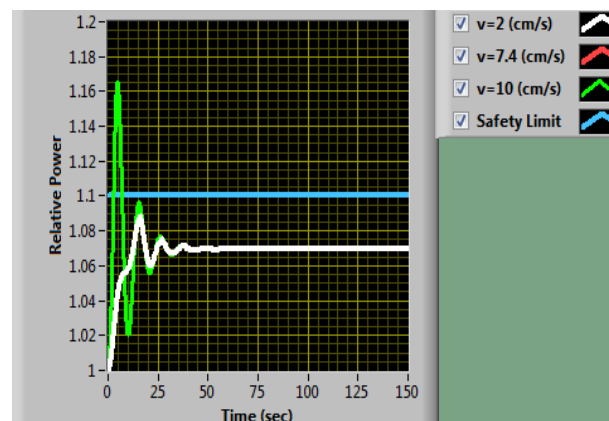


Fig. 6. Optimization of relative reactor power with linear control rod reactivity model in LabVIEW

safest power level is found as 107% RP which is well below the design safety limit (110%).

The optimal trend of average coolant temperature (ACT) is shown in Figure 7. The coolant cold leg temperature is 291.5 °C, coolant hot leg temperature is 328.5 °C, and initial reactor coolant average temperature is 307.8° C. The optimized value of average coolant temperature by using CORTH Code is 310 °C with ± 2.8 °C uncertainty. However, this average coolant temperature is overestimated by 2.2°C.

The optimized coolant average temperature using GNTHACP Code is 307.4 °C which is an excellent estimate as compared to CORTH Code.

3.2 Modeling and Nonlinear Optimization in LabVIEW

In this research work, a VI is designed for nonlinear SQP optimization as shown in Figure 8. The design of cost function for nonlinear SQP optimization VI is shown in Figure 9, while the design of front panel for nonlinear SQP optimization VI is shown in Figure 10.

The VI is designed for the computation of neutronics and thermal hydraulics system model parameters as shown in Figure 11. A VI is designed to model neutronics and thermal hydraulics model equations as shown in Figure 12. A VI is designed to calibrate the neutronics and thermal hydraulics system model as shown in Figure 13.

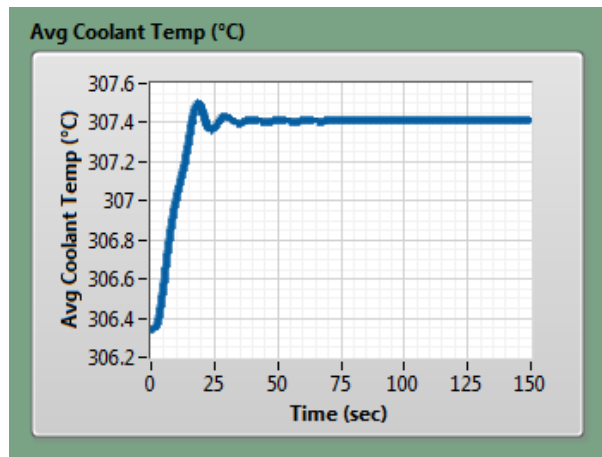


Fig. 7. Optimization of average coolant with linear control rod reactivity model in LabVIEW

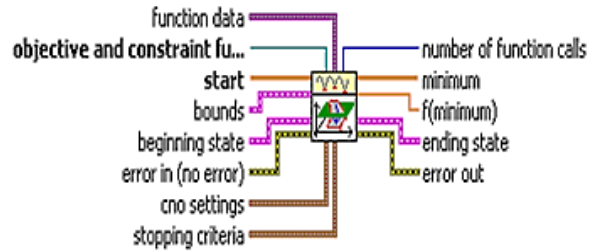


Fig. 8. Design of nonlinear SQP optimization VI in LabVIEW

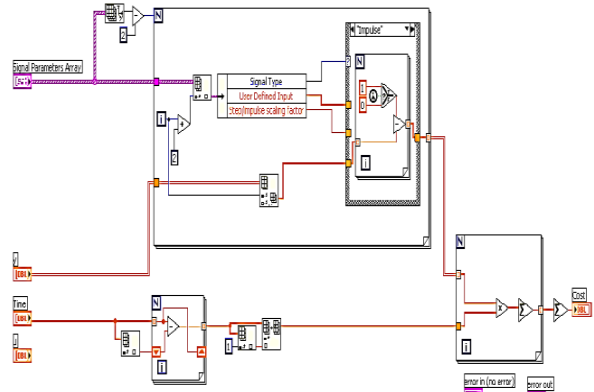


Fig. 9. Design of cost function for nonlinear SQP optimization VI in LabVIEW

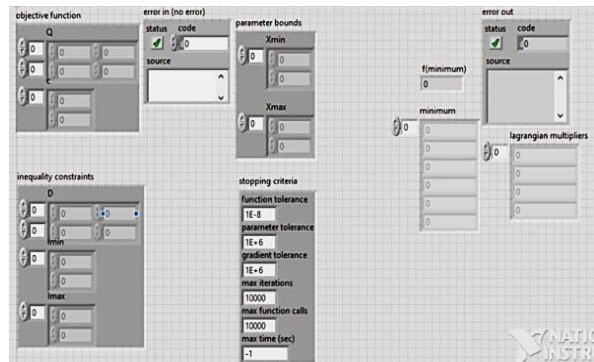


Fig. 10. Design of front panel for nonlinear SQP optimization VI in LabVIEW

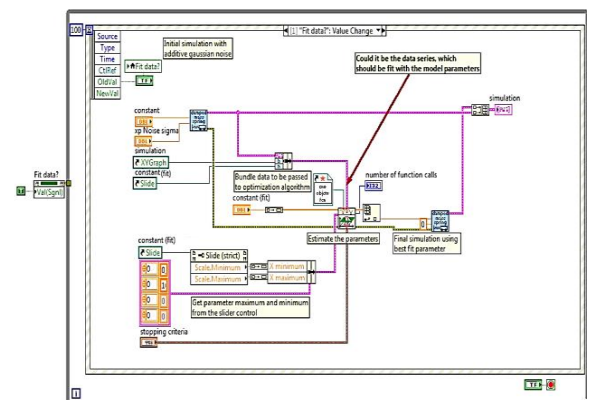


Fig. 11. Computation of neutronics and thermal hydraulics system model parameters in LabVIEW

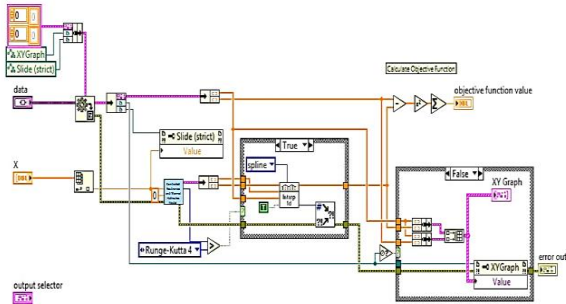


Fig. 12. Modeling of neutronics and thermal hydraulic system equations in LabVIEW

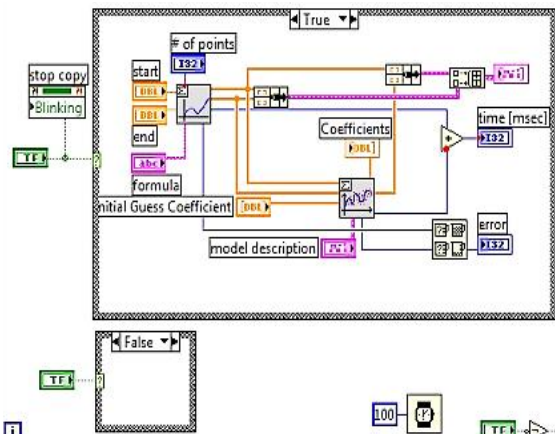


Fig. 13. Calibration of neutronics and thermal hydraulics system model in LabVIEW

The comparison of optimization parameters of both algorithms are tabulated in Table 1.

The behavior of relative reactor power against two different control rod speed is shown in Figure 14. The safest power level is found 107.33% RP which is well below the design safety limit. The optimal trend of average coolant temperature is shown in Figure 15.

The comparison of parameters of coupled neutronics and thermal hydraulics model of GNTHACP code and benchmark FSAR results computed

Table 1. Comparison of optimization parameters

GNTHACP Code	Design values
SIMPEX Algorithm Optimization Time (Sec)	70
SQP Algorithm Optimization Time (Sec)	52.5
Number of total gradient evaluations in SQP	31
SQP Lagrangian Multiplier	0.0036
SQP Penalty Factor	0.5
SQP Cost Function	0.0013

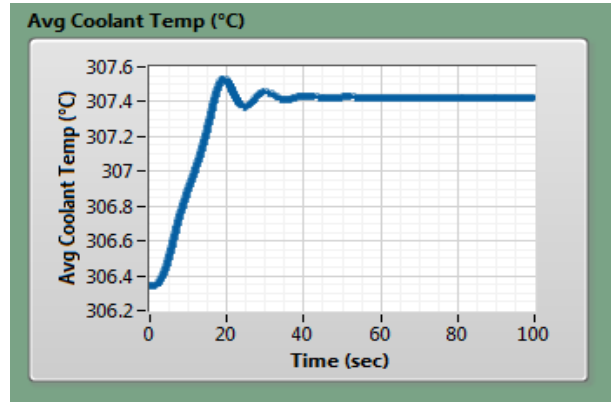


Fig. 14. Optimization of relative reactor power with nonlinear control rod reactivity model in LabVIEW

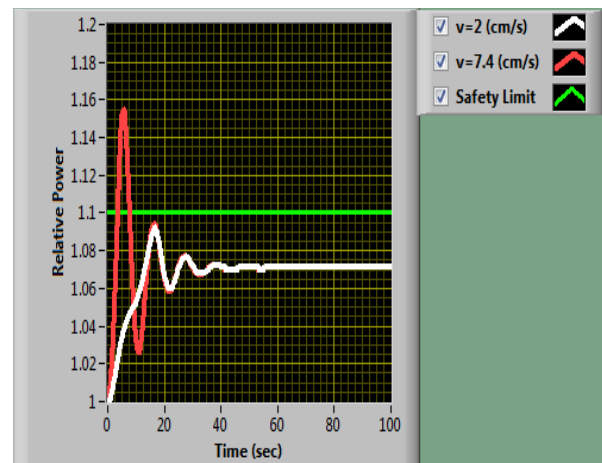


Fig. 15. Optimization of average coolant and fuel temperatures with nonlinear control rod reactivity model in LabVIEW

using CORCA and CORTH Codes is tabulated in Table 2. The results show that the proposed GNTHACP Code is quite accurate and hence a successful realization has been made.

4. CONCLUSION

The reactor neutronics and thermal hydraulics modeling has been successfully attempted and a state-of-the-art nuclear code (GNTHACP) is designed and developed in graphical programming environment LabVIEW. The GNTHACP nuclear code in LabVIEW is a step towards new toolkit development for the ACP1000 nuclear power plant neutronics and thermal hydraulics modeling in LabVIEW. The GNTHACP nuclear code is 100% equivalent to coupled CORCA and CORTH nuclear codes. The performance of GNTHACP nuclear code has been tested and validated against

Table 2. Parameters of coupled neutronics and thermal hydraulics model of GNTHACP code

Parameters	GNTHACP Code	FSAR Benchmark
MRRP (% RP)	107	110
MSCRS (cm/sec)	2	1.905
AFT (°C)	653	650
ACT (°C)	307.4	307.8

FSAR as benchmark and found robust. As such, the robustness of the GNTHACP nuclear code is established as tested and validated under extreme safety limits of ACP1000 imposed over the neutronics and thermal hydraulic parameters to ensure the design and optimization process valid under maximum allowed perturbing conditions. The results of control rod speed, reciprocal reactor period, relative reactor power, coolant temperature have been investigated and found industry standard toolset (IST) for neutronics and thermal hydraulics modeling of ACP1000 nuclear power plant. The proposed code development has established a strong basis for similar development for nuclear reactor systems other than ACP1000 in future.

5. ACKNOWLEDGEMENTS

The support of the Pakistan Atomic Energy Commission, Chashma Centre of Nuclear Training and Information System Division of KNPGS is gratefully acknowledged.

6. CONFLICT OF INTEREST

The authors declare no conflict of interest.

7. REFERENCES

1. M. Johnson, S. Lucas, and P. Tsvetkov. Modeling of reactor kinetics and dynamics. *Idaho National Laboratory, Report Idaho Falls, Idaho 83415, U.S. Department of Energy, Canada* (2010).
2. A. Laureau, D. Heuer, E.M. Lucotte, P.R. Rubiolo, M. Allibert, and M. Aufiero. Transient coupled calculations of the molten salt fast reactor using transient fission matrix approach. *Nuclear Engineering and Design* 316 (01): 112-124 (2017).
3. W.K. Lam. Pressurized water reactor simulator. IAEA Workshop Material, Second Edition, *IAEA, Vienna* (2005).
4. A.S. Mollah. Education tool for simulation of safety and transient analysis of a pressurized water reactor. *International Journal of Integrated Sciences & Technology* 03: 01-10 (2018).
5. S.U.E. Hakim, A. Abimanyu, and Sutanto. Simulator design of Kartini reactor based on LabVIEW. *Journal forum Nukir* 12 (1): 29-41 (2018).
6. S.M.A. Ibrahim. Thermal hydraulic simulations of a PWR nuclear power plant. *International Journal of Safety and Security* 013 (01): 31-520 (2019).
7. L.A. Macedo, W.M. Torres, G. Sabundjian, D.A. Andrade, A.B. Junior, P.E. Umbehaun, T.N. Conti, R.N. Mesquita, P.H.F. Masotti, and G. Angelo. Development of a LabVIEW web-based simulator for RELAP. *International Nuclear Atlantic Conference, Brazil*: 01-13 (2011).
8. J. Park, J. Jang, H. Kim, J. Choe, D. Yun, P. Zhang, A. Cherezov, and D. Lee. Three-Dimensional nodal diffusion code for pressurized water reactor core analysis. *Energies* 13(23): 6324 (2020).
9. A.H, Malik, A.A. Memon, and F. Arshad. Advanced multi-modeling of PWR dynamics and deep learning based computational tool in SIMULINK and LabVIEW. *Proceedings of Pakistan Academy of Sciences-A: Physical and Computational Sciences* 59(01): 71-81 (2022).
10. A. Rais, D. Siefman, G. Girardin, M. Hursin, and A. Pautz. Methods and models for the coupled neutronics and thermal-hydraulics analysis of the CROCUS reactor at EFPL. *Science and Technology of Nuclear Installations* 2015: 01-10 (2015).
11. F.P. Ribeiro, and J. Su. Coupled neutronics-thermal hydraulics analysis in a coolant sub-channel of a PWR using CFD techniques. *International Nuclear Atlantic Conference, 22-27 October*: 01-25 (2017).
12. S.M.H. Mousakazemi. Control of a pressurized light-water nuclear reactor two-point kinetics model with performance index-oriented PSO. *Nuclear Engineering and Technology* 53 (08): 2556-2563 (2021).
13. A. Tanaka, K. Futahashi, K. Takanabe, and C. Kurimura. Development of a 3-D simulation analysis system for a PWR control rod drive mechanism. *International Journal of Pressure Vessels and Piping* 85: 655-661 (2008).
14. C. Wang, C. Yan, J. Wang, C. Tian, and S. Yu. Parametric optimization of steam cycle in PWR nuclear power plant using improved genetic-simplex algorithm. *Applied Thermal Engineering* 125: 830-845 (2017).
15. P.T. Boggs, and J.W. Tolle. Sequential quadratic programming for large scale nonlinear optimization. *Journal of Computational and Applied Mathematics* 124: 123-137 (2000).
16. M. Torabi, A. Lashkari, S.F. Maoudi, and S. Bagheri. Neutronic analysis of control rod effect on safety parameters in Tehran Research Reactor. *Nuclear Engineering and Technology* 50(07): 1017-1023 (2018).

Instructions for Authors

Manuscript Format

The manuscript may contain Abstract, Keywords, INTRODUCTION, MATERIALS AND METHODS, RESULTS, DISCUSSION (or RESULTS AND DISCUSSION), CONCLUSIONS, ACKNOWLEDGEMENTS, CONFLICT OF INTEREST and REFERENCES, *and any other information that the author(s) may consider necessary.*

Abstract (font size 10; max 250 words): Must be self-explanatory, stating the rationale, objective(s), methodology, main results, and conclusions of the study. Abbreviations, if used, must be defined on the first mention in the Abstract as well as in the main text. Abstract of review articles may have a variable format.

Keywords (font size 10): Three to eight keywords, depicting the article.

INTRODUCTION: Provide a clear and concise statement of the problem, citing relevant recent literature, and objectives of the investigation.

MATERIALS AND METHODS: Provide an adequate account of the procedures or experimental details, including statistical tests (if any), concisely but sufficient enough to replicate the study.

RESULTS: Be clear and concise with the help of appropriate Tables, Figures, and other illustrations. Data should not be repeated in Tables and Figures, but must be supported with statistics.

DISCUSSION: Provide interpretation of the RESULTS in the light of previous relevant studies, citing published references.

ACKNOWLEDGEMENTS: (font size 10): In a brief statement, acknowledge the financial support and other assistance.

CONFLICT OF INTEREST: State if there is any conflict of interest.

REFERENCES (font size 10): Cite references in the text **by number only in square brackets**, e.g. “Brown et al [2] reported ...” or “... as previously described [3, 6–8]”, and list them in the REFERENCES section, in the order of citation in the text, Tables and Figures (not alphabetically). Only published (and accepted for publication) journal articles, books, and book chapters qualify for REFERENCES.

Declaration: Provide a declaration that: (i) the results are original; (ii) the same material is neither published nor under consideration elsewhere; (iii) approval of all authors have been obtained; and (iv) in case the article is accepted for publication, its copyright will be assigned to *Pakistan Academy of Sciences*. Authors must obtain permission to reproduce, where needed, copyrighted material from other sources and ensure that no copyrights are infringed upon.

Manuscript Formatting

Manuscripts must be submitted in Microsoft Word (2007 Version .doc or .docx format); **pdf** files not acceptable. Figures can be submitted in Word format, TIFF, GIF, JPEG, EPS, PPT. Manuscripts, in *Times New Roman*, 1.15spaced (but use single-space for Tables, long headings, and long captions of tables & figures). The text must be typed in a double-column across the paper width. The Manuscript sections must be numbered, i.e., **1. INTRODUCTION, 2. MATERIALS AND METHODS**, and so on... (a) **Title** of the article (Capitalize initial letter of each main word; font-size 16; **bold**), max 160 characters (no abbreviations or acronyms), depicting article’s contents; (b) Author’ first name, middle initial, and last name (font size 12, **bold**), and professional affiliation (i.e., each author’s Department, Institution, Mailing address and Email; but no position titles) (font size 12); (c) Indicate the corresponding author with *; (d) **Short running title**, max 50 characters (font size 10).

Headings and Subheadings (font size 11): All flush left

LEVEL-1: ALL CAPITAL LETTERS; Bold

Level-2: Capitalize Each Main Word (Except prepositions); Bold

Level-3: Capitalize each main word (Except prepositions); Bold, Italic

Level-4: Run-in head; Italics, in the normal paragraph position. Capitalize the initial word only and end in a colon (i.e., :)

List of REFERENCES must be prepared as under:

a. Journal Articles (*Name of journals must be stated in full*)

1. I. Golding, J. Paulsson, S.M. Zawilski, and E.C. Cox. Real time kinetics of gene activity in individual bacteria. *Cell* 123: 1025–1036 (2005).
2. W. Bialek, and S. Setayeshgar. Cooperative sensitivity and noise in biochemical signaling. *Physical Review Letters* 100: 258–263 (2008).
3. R.K. Robert, and C.R.L.Thompson. Forming patterns in development without morphogen gradients: differentiation and sorting. *Cold Spring Harbor Perspectives in Biology* 1(6) (2009).
4. D. Fravel. Commercialization and implementation of biocontrol. *Annual Reviews of Phytopathology* 43: 337359 (2005).

b. Books

5. W.R. Luellen. Fine-Tuning Your Writing. *Wise Owl Publishing Company, Madison, WI, USA* (2001).
6. U. Alon, and D.N. Wegner (Ed.). An Introduction to Systems Biology: Design Principles of Biological Circuits. *Chapman & Hall/CRC, Boca Raton, FL, USA* (2006).

c. Book Chapters

7. M.S. Sarnthein, and J.D. Stanford. Basal sauropodomorpha: historical and recent phylogenetic developments. In: *The Northern North Atlantic: A Changing Environment*. P.R. Schafer, & W. Schluter (Ed.), *Springer, Berlin, Germany*, pp. 365–410 (2000).
8. J.E. Smolen, and L.A. Boxer. Functions of Europhiles. In: *Hematology*, 4th ed. W.J. Williams., E. Butler and M.A. Litchman (Ed.), *McGraw Hill, New York, USA*, pp. 103–101 (1991).

d. Reports

9. M.D. Sobsey, and F.K. Pfaender. Evaluation of the H2S method for Detection of Fecal Contamination of Drinking Water, Report WHO/SDE/WSH/02.08, *Water Sanitation and Health Programme, WHO, Geneva, Switzerland* (2002).

e. Online references

These should specify the full URL for reference and give the date on which it was consulted. Please check again to confirm that the work you are citing is still accessible:

10. L. Branston. SENSPOL: Sensors for Monitoring Water Pollution from Contaminated Land, Landfills and Sediment (2000). <http://www.cranfield.ac.uk/biotech/senspol/> (accessed 22 July 2005)

Tables and Figures

Insert all tables as editable text, not as images. Number tables consecutively following their appearance in the text, Figures should appear in numerical order, be described in the body of the text, and be positioned close to where they are first cited. Each figure should have a caption that describes the illustration, and that can be understood independently of the main text (Caption Table 1. and Fig 1. font size 10; Bold; Captions should be in sentence case; left-aligned). All Figures should have sufficiently high resolution (minimum 1000 pixels width/height, or a resolution of 300 dpi or higher) to enhance the readability. Figures may be printed in two sizes: column width of 8.0 cm or page width of 16.5 cm; number them as **Fig. 1**, **Fig. 2**, ... in the order of citation in the text. Parts in a figure can be identified by A, B, C, D, ... and cited as Figure 2A, Figure 2B, Figure 2C. Captions to Figures must be concise but self-explanatory. Laser printed line drawings are acceptable. Do not use lettering smaller than 9 points or unnecessarily large. Photographs must be of high quality. A scale bar should be provided on all photomicrographs.

Tables: with concise but self-explanatory headings must be numbered according to the order of citation (like **Table 1.**, **Table 2.**). *Do not* abbreviate the word "Table" to "Tab.". Round off data to the nearest three significant digits. Provide essential explanatory footnotes, with superscript letters or symbols keyed to the data. Do not use vertical or horizontal lines, except for separating column heads from the data and at end of the Table.

Figures: Figures may be printed in two sizes: column width of 8.0 cm or page width of 16.5 cm; number them as **Fig. 1, Fig. 2, ...** in the order of citation in the text. Captions to Figures must be concise but self-explanatory. Laser printed line drawings are acceptable. Do not use lettering smaller than 9 points or unnecessarily large. Photographs must be of high quality. A scale bar should be provided on all photomicrographs.

Note: The template of the manuscript is available at <http://www.paspk.org/proceedings/>; <http://ppaspk.org/>

Reviewers: Authors may suggest four relevant reviewers, two National and two International (with their **institutional E-mail** addresses).

SUBMISSION CHECKLIST

The following list will be useful during the final checking of an article before sending it to the journal for review.

Ensure that the following items are present:

One author has been designated as the corresponding author with contact details:

- E-mail address (Correct and valid)
- Full address of Institute/organization
- Keywords
- All figure captions
- All tables (including title, description, footnotes)

Further considerations

- Manuscript has been 'spell-checked' and 'grammar checked'
- References are in the correct format for this journal
- All references mentioned in the Reference list are cited in the text, and vice versa
- Permission has been obtained for the use of copyrighted material from other sources (including the Internet)

In case of any difficulty while submitting your manuscript, please get in touch with:

Editor

Pakistan Academy of Sciences
3-Constitution Avenue, Sector G-5/2
Islamabad, Pakistan
Email: editor@paspk.org
Tel: +92-51-920 7140

Websites: <http://www.paspk.org/proceedings/>; <http://ppaspk.org/>



PROCEEDINGS OF THE PAKISTAN ACADEMY OF SCIENCES: PART A Physical and Computational Sciences

CONTENTS

Volume 60, No. 2, June 2023

Page

Research Articles

- Stability of Graphene on the Si (111) Surface: Insights from Reactive Molecular Dynamics Simulations 1
— *Didik Riyanto, Edy Kurniawan, Husein Muhammad Fras, Hanifsha Nur Azizah, and Rizal Arifin*
- Analysis of a City's Heat Island Effect on the Micro-Climature Parameters within Cities 7
— *Rishabh Sharma, Khan Amadur Rahman, Vasyl Tyshchenko, Oksana Illiash, and Iryna Mezentseva*
- Flow Control in a Rectangular Open Channel using Two Impermeable Spur Dikes: A Numerical Study 17
— *Hafiz Syed Moazzum Gillani, Zain-ul-Hassan, Hafiz Rana Azeem Sarwar, Muhammad Sohail Jameel, Waqar Hasan, Ehsaan Manzoor, and Imran Khan*
- Catalogues of Some Useful Classes of Circular Designs in Blocks of Three Different Sizes to Control Neighbor Effects 27
— *Akbar Fardos, Abdul Salam, Jamshaid Ul Hassan, Hurria Ali, Khadija Noreen, and Rashid Ahmed*
- A Stable Version of the Modified Algorithm for Error Minimization in Combined Numerical Integration 37
— *Aijaz Bhatti, Owais Ali Rajput, and Zubair Ahmed Kalhoro*
- Quantum Computer Architecture: A Quantum Circuit-Based Approach Towards Quantum Neural Network 45
— *Tariq Mahmood, Talab Hussain, and Maqsood Ahmed*
- Design and Development of Neutronics and Thermal Hydraulics Modeling Code for ACP1000 Nuclear Reactor Dynamics in LabVIEW 55
— *Arshad Habib Malik, Feroza Arshad, and Aftab Ahmad Memon*

Instructions for Authors

PAKISTAN ACADEMY OF SCIENCES, ISLAMABAD, PAKISTAN

HEC Recognized, Category Y; Scopus Indexed

Website: <http://www.paspk.org/proceedings/>; <http://ppaspk.org>